Government of **Western Australia**
Department of **Mines and Petroleum**

RECORD 2009/15

USING CALCULATED PSEUDOSECTIONS IN THE SYSTEM NCKFMASHTO AND SHRIMP U-PB ZIRCON DATING TO CONSTRAIN THE METAMORPHIC EVOLUTION OF THE LATITUDE HILLS PARAGNEISSES, WEST MUSGRAVE PROVINCE, WESTERN AUSTRALIA

by
Rodney J King

TRaX
Tectonics, Resources and Exploration

THE UNIVERSITY OF ADELAIDE
AUSTRALIA
BUD. CRUCE LUMEN




Geological Survey of
Western Australia

NGAANYATJARRA COUNCIL (Aboriginal Corporation)

Using calculated pseudosections in the system NCKFMASHTO and SHRIMP II U–Pb zircon dating to constrain the metamorphic evolution of paragneisses in the Latitude Hills, West Musgrave Province, Western Australia.

Rodney J. King.
Supervisors: Alan Collins, Martin Hand & David Kelsey.
Continental Evolution Research Group, School of Earth and Environmental Sciences,
University of Adelaide, Adelaide, South Australia, 5005, Australia.
(Corresponding Author email: rodney.king@adelaide.edu.au

Notice to the reader

This Record is one of a series of BSc. Hons theses researched, written and compiled by students from the Centre of Tectonics, Resources and Exploration (TRaX), University of Adelaide, through an ongoing collaborative project between the Geological Survey of Western Australia (GSWA) and the University of Adelaide. Although GSWA has provided field and laboratory support for this project, the scientific content of each Record, and the drafting of figures, has been the responsibility of the authors. No editing has been undertaken by GSWA.

All work carried out in the west Musgrave region is done so within the framework of an ongoing collaborative project involving GSWA, the Traditional Owners of the region and the Ngaanyatjarra Council. The considerable efforts of the Traditional Owners and of the Ngaanyatjarra Council in facilitating this work is gratefully acknowledged.

Using calculated pseudosections in the system NCKFMASHTO and SHRIMP II U-Pb zircon dating to constrain the metamorphism of the Latitude Hills paragneisses, West Musgrave Province, Western Australia.

Rodney J. King

Continental Evolution Research Group
School of Earth and Environmental Sciences
The University of Adelaide

Abstract

The Latitude Hills in the West Musgrave Province, Western Australia, preserve evidence for high to ultrahigh-temperature metamorphism in aluminous Fe-rich metapelites. Peak metamorphism during the Musgravian Orogeny (D2), is defined by the peak mineral assemblage: garnet, sillimanite, spinel, quartz, ilmenite and K-feldspar, with spinel and quartz often preserved in contact or separated by a corona of cordierite. Calculated pseudosections using THERMOCALC 3.30 (August 2007 update) of Powell and Holland (1988), in the geologically representative system: NCKFMASHTO (Na_2O-CaO-K_2O-FeO-MgO-Al_2O_3-SiO_2-H_2O-TiO_2-Fe_2O_3) indicate peak metamorphic conditions lie above previous estimates, in the range 900 – 1000 ºC and 6 – 8 kbar, representing significant temperature increase from previous peak P-T estimates of 800-850 ºC at 5 - 6 kbar for similar metapelites in the Tomkinson Range. Mineral growth from peak metamorphism suggests initial decompression at high temperatures allowing the growth of cordierite, followed by rapid cooling. Post-peak mineral assemblages characterised by magnetite, spinel, quartz, cordierite, plagioclase and biotite, occur as fine-grained domains and symplectites mantling peak mineral. Post-peak minerals formed during D3, following the Giles Event, have estimated P-T conditions typically cooler than D2. The calculated P-T conditions agree with more recent studies with

temperatures of 700 to 750 ºC at pressures between 4 to 6 kbars with late decompression textures defined by fine-grained growth of cordierite. SHRIMP U-Pb zircon dating was performed on one Birksgate-aged paragneiss with targeted zircon rim analyses yielding concordant or near-concordant ^{207}Pb corrected ^{238}U/^{206}Pb ages of 1297 ± 36, 1211 ± 13, 1151 ± 10 and 1081 ± 11 Ma, which correlate to known tectonothermal/magmatic events in the West Musgrave Province.

Key Words: metapelites, ultrahigh-temperature granulites, Latitude Hills, West Musgrave Province, THERMOCALC 3.30, NCKFMASHTO.

Mineral Abbreviations: quartz, q; garnet, g; sillimanite, sill; cordierite, cd; K-feldspar, ksp; plagioclase, pl; biotite, bi; silicate melt, liq; spinel, sp; magnetite, mt; kyanite, ky; free water, H_2O; ilmenite, ilm; orthopyroxene, opx.

Table of Contents

Special Acknowledgement
The author would like to thank the Ngaanyatjarra Council and the local traditional owners inthe Blackstone area for their help and support, and for allowing access to their lands for thepurposes of scientific research.

Introduction

A significant reappraisal of major earth processes began in the late 1980's, changing our view of how crustal rocks are affected by diverse tectonothermal processes (Bohlen, 1987, 1991; Brandt et al., 2007; Brown, 2006, 2007; Collins, 2002; Harley, 1989; Kelsey, 2007; Moraes et al., 2002; Mouri et al., 2003; Sajeev and Osanai, 2004; Satish-Kumar, 2000; Shaw and Arima, 1998; Zhang et al., 1996). Advances in analytical techniques have, and are continuing to extend understanding of deep crustal processes associated with lithospheric deformation and granulite to ultrahigh-temperature granulite-facies metamorphism. Establishment of qualitative and semi-qualitative modelling of reactions in petrogenetic grids using interpreted reaction textures in metapelitic rocks has driven the revolution in understanding of metamorphic processes. More recently, methods for quantitative evaluation of mineral equilibria using calculated pseudosections continues to offer higher accuracy and potentially tighter constraints to the metamorphic history recorded in high-grade rocks.

Ultrahigh-temperature (UHT) granulites are a relatively new addition to recognised metamorphic facies rocks, defined by mineral assemblages formed at high temperatures and low pressures. Definitive mineral assemblages of UHT granulites include; sapphirine+quartz, orthopyroxene+sillimanite+quartz, and spinel+quartz (Kelsey, 2007). UHT granulites are the result of the continuation of granulite facies metamorphism from >900 ºC and limited to the crustal rock liquidus, ~1150 ºC and generally occur within the stability field of sillimanite (Brown, 2007; Kelsey, 2007). Petrographic analysis of mineral relationships and reaction textures, integrated with phase equilibria modelling of chemical systems offer unique solutions for the determination of the tectonothermal evolution of high-grade metamorphic terranes (Bodorkos and Clark, 2004; Bohlen, 1987; Brown, 2002a, b; Hensen, 1971; Kelsey, 2007; Kelsey et al., 2003b; Kelsey et al., 2003c; Kriegsman and Hensen, 1998; Moraes et al., 2002; Morimoto et al., 2004; Mouri et al., 2003; Passchier and

Trouw, 2005; Sajeev and Osanai, 2004; White et al., 2000). By coupling petrographic analysis with calculated pseudosections and geochronological data gathered from U-Pb analysis from zircon and monazite analyses in-addition-to, other geochronological and geochemical data, the metamorphic history of a given terrain may be reliably constrained within a regional synthesis (Kelly et al., 2006; Kelsey et al., 2003a; Shabeer et al., 2005; Sun et al., 1996; White et al., 1999; Wingate et al., 2004; Wingate et al., 1998).

The following paper presents calculated P-T pseudosections, using the internally consistent THERMOCALC 3.30 software (August 2007 update) of Powell and Holland (1988), in the geologically representative system: NCKFMASHTO (Na_2O-CaO-K_2O-FeO-MgO-Al_2O_3-SiO_2-H_2O-TiO_2-Fe_2O_3). Use of calculated P-T pseudosections, evaluate the metamorphic evolution and potential for the paragneisses of Latitude Hills to have reach peak metamorphic conditions in ultrahigh-temperature granulite facies. Additionally, temporal constraints on metamorphic events are provided by geochronological analyses of zircon rims and cores, using SHRIMP II (Super-High Resolution Ion Microprobe). The titanium-in-zircon thermometer (Watson et al., 2006) and Rare Earth Element (REE) compositions of zircon are explored to determine growth of mineral phase during formation of zircon cores and rims (Buick et al., 2006; Rubatto, 2002a).

Tectonic Setting

The Meso-Neoproterozoic Musgrave Block occupies an area of ~120,000 km^2 across three state and territory boundaries – the Northern Territory, South Australia and Western Australia in central Australia (Fig. 1) (Daniels, 1974; Wade et al., 2006) and is bounded by the younger Amadeus Basin to the north, the Officer Basin to the south and the Canning Basin to the west. The Musgrave Province is a basement inlier composed of two domains. The Mulga Park Domain (Fig. 1) which is composed of amphibolite facies rocks to the north of the Woodroffe Thrust, referred to as the Olia gneiss (Fig. 1). The Fregon Domain is composed of dominantly granulite facies rocks, known as the Birksgate Complex (Edgoose et al., 2004; Major and Conor, 1993; Wade et al., 2007). The metamorphic evolution of the Birksgate Complex is the focus of this study.

The Birksgate Complex is composed of the oldest known rocks of the Musgrave Province, with geochemically derived protolith ages of 1600-1540 Ma (Camacho and Fanning, 1995; Edgoose et al., 2004; Howard et al., 2006; White et al., 1999). Sedimentation and volcanism may be related to arc magmatism during the period 1590-1550 Ma (Wade et al., 2006). There is currently no recognised structural or metamorphic record associated with the sedimentation/emplacement of the ~1600 – 1550 Ma gneiss (Wade et al., 2007).

U-Pb zircon geochronological evidence from the *eastern* Fregon Domain suggests ~1400 Ma sedimentation of quartzofeldspathic pelites and calcsilicates and synchronous formation of migmatitic and mafic/felsic gneiss (Wade et al., 2007). These metasediments are currently unnamed in the *eastern* Fregon Domain, but possible lithostratigraphic equivalents identified in the *western* Fregon Domain include metasedimentary units of the Tomkinson Range, including Mount West and the Latitude Hills. Composed of quartzofeldspathic, metapelite

and calcsilicate gneiss, possibly of volcanosedimentary origin, these metasediments have a maximum deposition age of 1390-1330 Ma and are currently grouped within the Birksgate Complex (Howard et al., 2006; White et al., 1999).

Following sedimentation of protoliths to the younger Birksgate Complex, felsic orthogneiss and granites were emplaced between 1324 – 1296 Ma as constrained by U-Pb zircon dating (White et al., 1999) within the Tomkinson Range. Although they are unnamed in Wade et al. (2007), these orthogneisses are referred to as the Wankanki Supersuite (White et al., 1999) and with recent geological mapping by Western Australian Geological Survey identified within the Latitude Hills (Howard et al., 2006), and principally reside south of the Hinckley Fault. Within this time period, the first tectonothermal event is recorded and referred to as D_1 – the Mount West Orogeny (Howard et al., 2006; Wade et al., 2007) is also interpreted from field relationships and geochronological data at Cohn Hill and Mt. Aloysius (Kelly et al., 2006). This deformation event is likely to have reached granulite facies conditions, and resulted in the formation of the migmatitic layering defining S_1 and voluminous leucocratic melt generation (White et al., 1999; White et al., 2002). The Mount West Orogeny can be correlated, at least temporally, to the first of two events recorded in the Albany-Fraser Orogen where metamorphic conditions reached ~800–850 °C and 5–7 kbar and resulted in the later emplacement of 1290–1280 Ma Recherche Granite sills (Bodorkos and Clark, 2004).

The second major tectonothermal event was the Musgravian Orogeny (D_2), is constrained by U-Pb dating of zircon, titanite and monazite to the interval 1230 – 1150 Ma (Camacho and Fanning, 1995; Edgoose et al., 2004; Kelly et al., 2006; Wade et al., 2007; White et al., 1999). This major tectonothermal event resulted in the regionally pervasive, amphibolite to granulite facies metamorphism throughout much of the exposed Musgrave Block. At Mount

West, low pressure – high temperature metamorphism associated with the Musgravian Orogeny (≥800 °C at pressures of 5 – 6 kbar) was identified by White et al., (2002). The Musgravian Orogeny resulted in the formation of the dominant gneissosity, migmatitic layering, the transposition of S_1/ F_1 and formation of tight to isoclinal folds (F_2) (Wade et al., 2007). Emplacement of the voluminous Pitjantjatjara Supersuite granite occurred during, and continued after the Musgravian Orogeny, from 1200 – 1140 Ma (Wade et al., 2007). This Musgravian (D_2) event, is also temporally related to a second tectonothermal event in the Albany-Fraser Orogen (Bodorkos and Clark, 2004; Kelly et al., 2006; White et al., 1999) and possibly relates to a protracted and complicated 1345–1140 Ma convergence and amalgamation of the West Australian and Mawson cratons. Correlations through parts of eastern Antarctica including: the Windmill Islands and the Bunger Hills, also show temporally related granulite facies conditions and may have implications for the assembly of Rodinia (Wade et al., 2007; White et al., 1999).

The 1080 – 1040 Ma Giles Event resulted in the emplacement of mafic-ultramafic layered intrusions of the Giles Complex, part of the Warakurna large igneous complex (Wingate et al., 2004) and includes bimodal volcanism of the Tjauwata and Tollu Groups, tholeiitic dyke emplacement including the Alcurra dykes and sedimentation within an interpreted rift setting (Edgoose et al., 2004; Wade et al., 2007) likely related to mantle-plume processes (Wingate et al., 2004). These mafic-ultramafic intrusions were subsequently recrystallised during a granulite facies event - D_3, which, occurred at ~1060 Ma, deforming mafic-ultramafic sills emplaced during the Giles Event (Clarke et al., 1995; Edgoose et al., 2004). Deformation is characterised by complex strain partitioning resulting in the formation of mylonites, open folds and weak lineations in low strain zones. Tight to isoclinal folds and well developed lineations formed in high strain zones, which also likely formed the Michael Hills Anticline

(Clarke et al., 1995) which, the Latitude Hills are part. Metamorphic conditions are estimated to have reached granulite facies with temperatures of ~750 °C and pressure of ~ 8 - 11 kbar and did not exceed peak metamorphic conditions of earlier event(s) (Clarke et al., 1995; Edgoose et al., 2004) however, pressure and temperature estimates from S_3 fabrics and leucosomes from Mount West range 760-780 ºC and approximately 6 kbar White et al. (2002). Paucity of documented field observations and recognition of D_3 structures, currently limits the effects of the D_3 to the south of the Mann Fault (Edgoose et al., 2004).

The Amata Dolerite was emplaced at ~820 Ma as constrained by U-Pb baddelyite ages (Glikson and Ballhaus, 1996). The Amata Dolerite is temporally linked to the formation of the Adelaide Rift by baddelyite U-Pb ages of the Gairdner Dyke Swarm (Wingate et al., 1998). The emplacement if the Amata-Gairdner Dyke swarm at ~820 Ma is thought to be associated with the formation of the Centralian Superbasin, which covered the bulk of Proterozoic Australia (Sandiford and Hand, 1998). The basin formed during the protracted breakup of Rodinia, with rifting and break-up of Laurentia and Gondwanaland along the eastern margin of Proterozoic Australia at ~750 Ma resulting in the formation of the proto-Pacific Ocean (Edgoose et al., 2004; Myers et al., 1996; Wade et al., 2007; Wingate et al., 1998).

The Neoproterozoic Petermann Orogeny ~630-530 Ma was a long-lived, high strain – low temperature, amagmatic, dextral transpressional, intra-plate orogenic event that exhumed deep crustal rocks (Edgoose et al., 2004; Wade et al., 2007) and may be related to forces developed along plate margins (Sandiford and Hand, 1998). The Petermann Orogeny exhumed the Musgrave Block from beneath the Centralian Superbasin and is responsible for the Musgrave Block's current east-west architecture.

Peak metamorphism inferred across the Musgrave Block during the Petermann Orogeny, reached in excess of 700 °C and between 11-13 kbar (Scrimgeour and Close, 1999). Much of the exhumation occurred in the southwest of the Musgrave Block, within a crustal wedge. The northern boundary is defined by the Woodroffe Thrust and the Mann Fault to the south (Fig. 1). Structure and architecture of the Petermann Orogeny is characterised by crustal scale shear zones, such as, the north vergent Woodroffe Thrust. Formation of the Woodroffe Thrust displaced part of the Mulga Park Domain over the Amadeus Basin in addition to the south vergent thrusting of the Fregon Domain over the Officer Basin. Formation of mylonite and anhydrous pseudotachylite may be linked to the protracted formation of D_4 to D_7 (Clarke et al., 1995; Daniels, 1974; Edgoose et al., 2004; Glikson et al., 1996; Wade et al., 2007), with cross-cutting relationships between pseudotachylites and mylonites in the west Musgrave Block, suggesting formation at the brittle/ductile transition zone (Howard et al., 2005). Hand and Sandiford (1999) proposed a mechanism for exhumation where reactivation of structures in thermally weakened crust is made possible where thick sedimentary sequences blanket radiogenic crust.

Geology of the Latitude Hills

The Latitude Hills project area has an areal extent of some 70 km^2 in Western Australia and is bound to the east by the South Australian state border. The Latitude Hills are located along the southern margin of the Tomkinson Ranges, within the south–western Fregon Domain, approximately 20 km south-east of Mount West (Fig. 1). Within this area, the Latitude Hills are comprised of inselbergs of moderately weathered and poorly exposed granulites (Figure 2). Lithological units include migmatised (meta-diatexites) Birksgate-aged paragneisses; Wankanki-aged foliated and schlieric granites; foliated Pitjantjatjarra Suite granite and Giles Complex mafic-ultramafic intrusions; mylonites (Howard et al., 2006), and pseudotachylite (Figure 2). The comprehensive geological map of the area is presented in Appendix 1.

The Birksgate-age paragneisses (Howard et al., 2006) of the Latitude Hills are divided into two domains – (1) Southern paragneisses and (2) the Northern paragneisses (Fig. 2). The division of the geological units is based on lithological differences, structural relationships (Figs. 4a,b,c) and geophysical data – presented in Appendix 1. The first package of paragneisses is defined as a largely migmatitic domain defined by quartzofeldspathic-leucosomes and occasionally fine-grained, garnet-rich melanosomes (Fig. 3a); layer parallel quartzites (Fig. 3b), scapolite-bearing calcsilicates (Fig. 3c) and rafts of Al-Fe-rich metapelitic assemblages (Fig. 3d). Metapelites are typically high-grade, spinel-quartz bearing assemblages, including: garnet + sillimanite + cordierite + plagioclase + K-feldspar and minor biotite + magnetite + ilmenite – Figure 3d. Sub-vertical to vertical layer parallelism defines a dominant structural trend with layers forming a broad, kilometre scale antiformal fold, plunging steeply 73→338 with a calculated girdle = 13/158 - Figure 4b. Mineral lineation data plot along a great circle which intersects the calculated beta axis for foliation data, 79/279 – figure 4b. In addition, Pitjantjatjara Suite granite in the western edge

of the mapping area has steep, north-west dipping foliation – parallel to the regional fabric, constraining earliest deformation to mid-to-late D_2. This structure is correlated to similar scale structures in the area surrounding the Latitude Hills and interpreted to have formed during D_3 (Clarke et al., 1995; Edgoose et al., 2004; Glikson and Ballhaus, 1996).

Sharp contact relationships occur between leucosomes and garnetiferous metapelites, reflecting a migmatitic or intrusive relationship - figure 3e. Metapelites appear to have been highly deformed, characterised by rounded, porphyroclastic garnet which often resemble σ-type porphyroclasts, but often do not preserve early deformation structures and/or are overprinted by later growth of aggregates of sillimanite which defines the dominant foliation (Fig. 3d). At the meter scale, intrafolial isoclinal and rootless folds in leucosomes (Fig. 3f); and rare preserved leucosomal asymmetric and parasitic folds (F_1/F_2) in melanosomes (Fig. 3g), are characteristics of intense ductile deformation. Two generations of lineations are recorded, these, together with two early fold generations remain structurally unresolved but are likely to reflect early deformational events described above (Daniels, 1974; Kelly et al., 2006; Wade et al., 2007; White et al., 1999; White et al., 2002).

Dismembered, mafic dykes cross-cut lithologies within the migmatitic terrane and trend 150˚. These dykes have a recrystallised mineral texture and are composed of two pyroxenes, plagioclase and biotite, with biotite defining a weak to moderate foliation dipping 80/039 that is axial planar to the F_3 plunging antiform. Field evidence coupled with published literature indicate these dykes intruded prior to the D_3 tectonothermal event and subsequently reached granulite facies conditions (Clarke et al., 1995; Edgoose et al., 2004; Wade et al., 2007) and possibly relate to the emplacement of the Giles Complex ultramafic intrusion.

An additional, *unfoliated*, dyke suite cross-cuts the surrounding units, trending 140º SE. Field work did not define cross-cutting relationships between mafic dykes and mylonites in the south, due in part to limited exposure, however, the mafic dykes are cross cut by a conspicuous ~20-30 meter-wide fault zone. The fault zone trends ~320º and defined by conspicuous pseudotachylite. Sinistral, displacement of up to 5 meters of the dyke by a fault zone is indicated by slight curvature of the mafic dyke, caused by drag and repeated offset of splay faults. On the northern side of the fault, the truncated dyke was not observed in the local vicinity. Meter-scale sinistral displacement is common throughout the southern mapping area and is associated with the presence of epidote. Pseudotachylite occurring in the Michael Hills have similar structural trends and are interpreted to post-date Giles intrusion (Daniels, 1974) and probably relate to $D_{4\text{-}7}$ during the Petermann Orogeny (Clarke et al., 1995; Edgoose et al., 2004; Glikson and Ballhaus, 1996; Wade et al., 2007)

Interpretation of Total Magnetic Intensity images for the Latitude Hills indicates that the Southern Latitude Hills are characterised by lower total magnetic intensity than paragneisses in the northern Latitude Hills. Several magnetic ridges can be seen trending north-west to south-east and are interpreted to represent shear zones. The northern domain of the Latitude Hills is also a broadly migmatitic terrane composed of clinopyroxene-garnet-quartz-plagioclase-bearing paragneisses, garnet-sillimanite-bearing quartzites, interlayered melanosomes and quartzofeldspathic leucosomes, orthopyroxene-bearing granitoids, mylonites and pseudotachylites. Garnet-sillimanite-bearing quartzites often form ridge-tops, controlling topographic expression of the landscape and structurally overlie clinopyroxene-garnet-quartz-plagioclase bearing paragneisses. Structurally, the domain is characterised by upright, open to tight folds, plunging 07→282 – (Fig. 4c). Contacting the paragneisses in the north-west is the layered, mafic-ultramafic Giles intrusion which forms Latitude Hill (Fig. 2

and Appendix 1). Latitude Hill is deformed and constitutes part of the southern limb of the Michael Hills Anticline.

Localised orthopyroxene-bearing granitoids crop out, often with ≤100 m^2 areal exposure and have an intrusive contact relationship with quartzites and cpx + g + q + pl-bearing lithologies. Larger intrusions occasionally contain rafts of quartzite and are later cross-cut by mafic dykes. Mafic dykes in the northern domain trend in two orientations. One recorded dyke trends 030º and truncated by ~10m mylonite, while the majority of dykes trend 150º and occasionally cross-cut by faults indicating sinistral sense displacement. Faults are typically defined by pseudotachylite, and strike ~110º. Mylonites occur in the northern domain with strongly lineated surfaces often with total thickness up to 10 meters. Dip of one mylonitic surface was 40/213 with mineral stretching lineations plunging 34→253.

Metamorphic Analysis

Petrography

Tables 1 – 4 present representative mineral chemistry and summaries mineral assemblages for examined samples. Examination of peak and post-peak mineral assemblages and relationships forms the basis for the metamorphic reconstruction of the Latitude Hills. Four samples, MHLH-6, 7, 13 and 16 are representative of metapelitic lithologies in the Latitude Hills. Peak mineral assemblages are interpreted from coarse grain size, euhedral mineral relationships and where incomplete resorption textures form moats or reaction coronae that separate minerals. Post-peak assemblages are inferred from minerals that comprise reaction coronae and symplectic relationships (Kelsey et al., 2003c; Passchier and Trouw, 2005). It is recognised that there are inherent dangers in this method of interpretation and these have been considered when interpreting textural relationships (Kriegsman and Hensen, 1998; Passchier and Trouw, 2005; Vernon, 1996; White et al., 2002).

MHLH-6

Peak Assemblage: Coarse-grained antiperthite, quartz, prismatic sillimanite needles and aggregates and spinel, together with garnet represents interpreted peak assemblage (Fig. 5a), however, few peak minerals are in contact with the exception of a few occurrences of coexisting q-sp, shielded within local domains (Fig. 5b). Relict garnet porphyroclasts <0.5 mm to 8mm contain subrounded clasts of biotite, magnetite and quartz. Where peak quartz and garnet are in contact, planar surfaces define grain boundaries.

Post-peak Assemblage: The post-peak assemblage is principally comprised of cordierite which, often with K-feldspar, typically rimming garnet separates grains of the peak mineral assemblage (Fig. 5c). Cordierite commonly separates coarse grained quartz from spinel and is

associated with a second generation of spinel intergrowth with cordierite forming a globular sp-cd symplectite. Garnet is separated from sillimanite by cordierite, with garnet commonly exhibiting a 'dissolution' or resorption texture at the garnet grain boundary with small, 20-50 μm blebs of plagioclase, K-feldspar and to a lesser extent – biotite (Fig. 5d). Spinel and ilmenite are commonly rimmed by post-peak sillimanite, which is then separated from antiperthite (K-spar with exsolved plagioclase lamellae) by a moat of cordierite (Fig 5e).

MHLH-13

Peak Assemblage: The peak assemblage includes, garnet-spinel-quartz-sillimanite and antiperthite and may also include cordierite as there is a coarse grained generation of cordierite in the matrix (Fig. 6a). Relict garnet measuring approximately <1 mm to 10 mm, contains inclusions of ilmenite and magnetite, biotite and sillimanite. Rare, prismatic sillimanite forms aligned aggregates, defining the dominant foliation (Figs. 6b and 6c).

Post-peak Assemblage: Garnet is separated from spinel by a moat of cordierite and occasionally quartz and often contains globular cordierite-spinel symplectite (Figs. 6b and 6c). Spinel-quartz is occasionally present and forms part of the retrograde assemblage, most commonly coarse-grained spinel and quartz are separated by a moat of cordierite with globular symplectite of cordierite-spinel forming in contact with spinel (Fig. 6c). Spinel and sillimanite are similarly separated by a moat of cordierite with occasional globular cordierite-spinel symplectite. Abundant spherical zircon >5 to <20 μm occurs in cordierite moats surrounded by radiogenic halos (Fig. 6c).

MHLH-16

Peak Assemblage: This sample contains rounded garnet porphyroblasts 0.5 mm to 16 mm in size with quartz, sillimanite, magnetite and biotite inclusions (Fig. 7a). Coarse-grained ilmenite, spinel, quartz are present with minor sillimanite. Garnet and quartz are often in direct contact while quartz-spinel-ilmenite are often preserved as co-existing peak assemblages (Fig. 7b).

Post-peak Assemblage: Cordierite moats separate spinel and garnet and quartz remaining modally dominant, with cordierite in the matrix (Fig. 7a). Interpreted peak metamorphic spinel/ilmenite-quartz is occasionally preserved, commonly separated by cordierite moats (Fig. 7c). Figure 7c also shows a double reaction corona where garnet forms an outer rim that separates quartz in the matrix from the spinel-cordierite symplectite forming reaction within the garnet rim. Locally, extremely fine grained biotite-cordierite-magnetite vermicular intergrowth and symplectites occur as coronas around garnets that extend 20 μm outward from the garnet, of which, biotite and magnetite crystals are 3-5 μm in diameter (Fig. 7d).

MHLH-7 – Modelled sample and focus of study

Peak Assemblage: The peak assemblage consists of garnet-sillimanite-quartz-spinel and antiperthite. Generally, none of the interpreted peak assemblage minerals are preserved in textural equilibrium with each other and are separated by moats, myrmekitic intergrowths and symplectites. Garnet porphyroclasts measuring 1 – 15 mm contain abundant inclusions of ilmenite, minor magnetite, large inclusions of sillimanite (Fig. 8a). Garnet is rarely in contact with quartz and quartz is generally not in contact with sillimanite, typically separated by a moat of retrogressive plagioclase or cordierite. Much of the preserved peak spinel occurs within the ‘cracks’ of garnet porphyroblasts.

Post-Peak Assemblage: The post peak assemblage consists of cordierite, often intergrown, forming morphologically variable (myrmekitic, lamellar and globular) symplectite with plagioclase, K-feldspar and minor biotite – (Figs. 8a, 8b and Fig. 9). The occurrence of biotite diminishes with increased distance from garnet (Fig. 8c). Where peak spinel is involved in the post peak reaction between garnet-sillimanite-quartz, globular, post peak spinel-cordierite symplectite is formed (Fig. 10). Garnet is rimmed by plagioclase, biotite and K-feldspar, which has a distinctive reaction front, often forming vermicular intergrowth of plagioclase and cordierite (Fig. 8c). Quartz and sillimanite are separated by a moat of cordierite (Fig. 8d).

MHLH-7, Square 5

Peak Assemblage: This mineral assemblage occurs within a garnet embayment and may be considered a discrete system on the basis that it is removed and somewhat shielded from reaction series found in the matrix. The peak mineral assemblage is comprised of garnet-sillimanite-spinel and minor quartz.

Post Peak Assemblage: The post peak assemblage is composed predominantly of cordierite which forms moats that separates garnet from sillimanite, spinel from sillimanite, spinel from garnet and an important peak assemblage – quartz is separated from spinel by a moat of cordierite. Plagioclase forms intergrowths with biotite along the edge of garnet and is generally in contact with cordierite.

Mineral Chemistry

Microprobe spot analyses were undertaken on the Cameca SX51 electron microprobe using SAMX software located at Adelaide Microscopy. Operating conditions involved an accelerating voltage 15kV and a beam current of 20nA to analyse 13 elements: F-Na-Mg-Al-Si-Cl-K-Ca-Ti-Cr-Mn-Fe-Zn utilizing wavelength dispersive spectrometers. Microprobe data is presented in Tables 1, 2 and 3 and mineral composition ranges and in Table 4.

Orthopyroxene and *Clinopyroxene* from sample MHLH-11 have simple mineral chemistry with no apparent zonation or compositional trends across individual grains. Orthopyroxene X_{Fe} ranges 0.47-0.50 with little variation while clinopyroxene calcium content ranges X_{Ca} 0.16-0.39 (Table 2) with some variation but with no apparent zonation trends from core to rim of crystals.

Biotite occurs in two lithological units including recrystallised dykes and metapelites. Biotite within recrystallised dykes is in contact with plagioclase and two pyroxenes. Titanium is abundant in biotite ranging 4.73-5.33 oxide wt%, similarly flourine ranges 1.11-1.24 oxide wt%. Biotite in metapelites is flourine and titanium-rich with TiO_2 ranges 2.80 – 4.92 wt% and flourine ranges 1.69 – 3.87 wt% - Table 2.

Cordierite exists as two mineral phases: – (1) large, twinned crystals that occupy much of the matrix and is often associated with plagioclase and K-feldspar; (2) as coronas and moats that separate garnet-spinel, sillimanite-spinel, quartz-spinel assemblages. Cordierite mineral chemistry is typically homogenous, regardless of the textural setting or mineral associations. Probe analyses return low variability and consistent X_{Fe} results ranging 0.47-0.48 (MHLH-6)

from both symplectic cordierite and coarse-grained cordierite. Sample MHLH-14 X_{Fe} = 0.39-0.41 and MHLH-16 X_{Fe} = 0.33-0.40 (Table 2).

Garnet occurs as rounded porphyroblasts within metapelites, often with inclusions of sillimanite, magnetite, ilmenite, biotite plagioclase and quartz. Garnet is typically ~75-85 $\%_{almandine}$ and 11.6 – 19.93 $\%_{pyrope}$ and 0.6 – 1.75 $\%_{spessartine}$ in metapelites, reflecting the typically iron-rich composition of the rocks. Garnet composition in sample MHLH-9, are compositionally different to metapelitic garnets with spessartine comprising 7.73-9.40 %, 83.75 – 87.46 $\%_{almandine}$ and 4.46 – 6.21 $\%_{pyrope}$. This differs from the metapelites where spessartine typically comprises only 0.60 – 1.75 % of garnet composition (Table 2). While spot analyses are not available, mapping of sample MHLH-7 reveals zoning of Ca and Mg, with decreasing concentrations towards the rim of the crystal (Fig. 9). Zoning of calcium appears to be most strongly expressed when garnet is in contact with plagioclase and zoning of magnesium appears to be strongest when garnet is in contact with cordierite. No zoning of iron and manganese in garnet was present.

Spinel is typically iron rich, forming hercynite (X_{Fe}= 0.82-0.90). Occasional probe analyses revealed elevated ZnO, with a maximum value of 2.90 oxide wt%, though typical ZnO values ranges 0.35 0.41 oxide wt%. Systematic partitioning of ZnO between peak and retrograde spinel could not be determined. Similarly, CrO average values ranges 0.32 – 0.63 wt% with occasional elevated values of ~1.00 wt% and no systematic partitioning identified (Table 2).

K-feldspar Mineral chemistry for K-feldspar is consistent, with X_{Na} of samples typically ranging 0.05 – 0.1 and the highest X_{Na} occurring in sample MHLH-16 with an X_{Na} of 0.07 0.21 (Table 2).

Plagioclase Chemically, plagioclase is interesting, with little compositional range across analysed areas within individual samples, however between samples, X_{Na} can be relatively high, for example in MHLH-6 ranging X_{Na} = 0.52-0.54. Compared to MHLH-14 where X_{Na} = 0.37-0.39. Plagioclase in sample MHLH-9, shows different mineral chemistry, X_{Na} = 0.22-0.23, with no exsolution lamellae and no complex post-peak symplectite mineral reactions (Table 2).

P-T-X Evolution of the Southern Latitude Hills paragneisses

At the micro-to-mesoscopic scale, granulites are typically heterogeneous in composition, often characterised by composition and microstructural domains, commonly - peak mineral assemblages, mantled by finer-grained, retrograde mineral assemblages, including the distribution of crystallised leucosome. The formation of compositional domains and microstructures result from decreasing equilibration volumes – primarily controlled by decreasing temperatures and fluid-dependant element mobility and diffusion (Brown, 2002a; Stüwe, 1997). Open-system processes, such as melt loss, are important in the preservation of granulite facies rocks (Vanderhaeghe, 2001; White and Powell, 2002; White et al., 2007). Anhydrous peak mineral assemblages often show incomplete resorption of peak mineral assemblages by retrograde mineral assemblages forming incomplete reaction coronae and symplectites (Kelsey et al., 2003b). During prograde metamorphism, biotite breakdown constitutes a major melting step where H_2O is released from the biotite crystal lattice and stimulates melting of the rock mass. Biotite breakdown is a major melt step during prograde metamorphism that yields H_2O which is preferentially partitioned into quartzofeldspathic liquid phase (White and Powell, 2002). Subsequent, progressive removal of the hydrous component occurs with progressive melt loss, and is coupled with, or is dependant on -

ductile deformation (Vanderhaeghe, 2001; White and Powell, 2002). Continued loss of quartzofeldspathic melt depletes the system of H_2O, K, Na and Ca – producing a refractory bulk composition and the formation of anhydrous mineral phases such as garnet, spinel, sillimanite and feldspar (Kelsey et al., 2003b; White and Powell, 2002).

Consideration of H_2O and Fe^{3+} content in the mapped sample is required when setting bulk compositions that adequately represents whole-rock chemistry in the NCKFMASHTO system. H_2O cannot be directly measured using the electron microprobe and is estimated by petrographic interpretation of hydrous mineral phases such as biotite and cordierite and quartzofeldspathic-leucosomes. The method for developing a bulk composition that adequately represents the mineral assemblage is adopted from (Kelsey et al., 2003c; White et al., 2000; White et al., 2007).

Biotite is a minor accessory mineral with ~0.03 modal proportion and typically contains abundant Ti and F with OH constituting 1.5 - 2 % of the mineral chemistry. Cordierite is an abundant mineral phase and forms much of the retrograde mineral assemblage. Estimates of the modal proportion of cordierite and biotite in thin section totals ~35% and given mineral chemistry data from microprobe spot analyses, which indicates H_2O constitutes ~2-3% of the minerals H_2O is estimated to contribute 1-2 Mol %. Calculating the concentration of oxide minerals in modelled samples from the Latitude Hills is important when considering stability of various mineral phases, in particular spinel, garnet and sillimanite (Mouri et al., 2003; Mouri et al., 2004; White et al., 2000). Calculation of Fe_2O_3 from probe analyses was based on the stoichiometric conversion method of Droop (1987).

Calculated pseudosections are based on the sample metapelite sample, MHLH-7, because of the diverse mineral assemblage. Peak mineral assemblage includes: garnet + sillimanite + spinel + quartz + antiperthite; and the post-peak mineral assemblage cordierite + biotite + plagioclase + K-feldspar + magnetite, and are representative of the typical metapelitic assemblages throughout the Latitude Hills. Pseudosections were calculated in the large, geologically representative system; NCKFMASHTO (Na_2O-CaO-K_2O-FeO-MgO-Al_2O_3-SiO_2-H_2O-TiO_2-Fe_2O_3) using THERMOCALC 3.30, based on the internally consistent dataset: tcds55 (22 Nov 2003) and using the a-x relationships of White et al. (2007). Calculations considered the minerals, garnet (g), cordierite (cd), quartz (q), aluminosilicate (ky/sill), orthopyroxene (opx), spinel (sp), plagioclase (pl), K-feldspar (ksp), magnetite (mt), biotite (bi), silicate liquid (liq), and fluid (H_2O). Chemical data was collected using quantitative x-ray mapping utilising the Cameca SX51 electron microprobe with SAMX software located at Adelaide Microscopy. Operating conditions included an accelerating current of 100 nA, pixel size of 1024, step size of 4 μm and a dwell time of ~20 milliseconds. The elements, Na-Mg-Al-Si-K-Ca-Ti-Fe were analysed utilising wavelength dispersive spectrometers, resulting in 8 element maps (Marmo et al., 2002). The maps were processed in Matlab using the Bence-Albee Algorithm from Clarke et al., (2001), with a single image, (Fig. 11), resulting from the integration of each element map. Individual maps with accompanying photomicrographs are presented as addition material in Appendix 2. From this single compound map (Fig. 11), bulk compositions were calculated for the whole map and for 7 domains. Chemical data was converted to mole % for modelling in THERMOCALC 3.30 (Powell and Holland, 1988) – Table 5. Square 5, figs. 11 and 12, was selected as a unique domain and was also modelled using calculated pseudosections. A previous study by White et al. (2007) utilised chemically similar Al-Fe-rich metapelites to metapelites in the Latitude Hills, where the stability of sp-q assemblages were examined in

the system NCKFMASHTO. Pseudosections from Figure 9a, in White et al. (2007) is the starting reference for this study. Bulk compositions for all calculated pseudosections are presented in Table 6.

Calculated Pseudosections

The first calculated pseudosection is a Temperature-Composition (T-X) diagram – Figure 13, investigating the stability of mineral phases in varying MgO-FeO compositional space with the MgO-rich end-member located on the left-hand axis and the FeO-rich end-member located on the right-hand axis. The temperature range is 700 – 1100 ºC – Figure 13. Pressure is a fixed variable allowing for temperature ranges on the y-axis and sliding MgO-FeO compositions on the x-axis. Pressure is set at 4.4 kbar with stable mineral assemblages determined from reaction lines in the Pressure – Temperature (P-T) pseudosection Fig. 9, from White et al. (2007). For example, the divariant field (v=2) and the reaction line cd-sill-bi-sp-ksp-pl-liq-ilm-q-[mt] – (where [mt] defines magnetite-out line) intersects a line extending from 4.4 kbar at 700 ºC to 850 ºC is determined as a stable mineral assemblage and therefore is a recognised starting point for the T-X pseudosection.

This temperature-composition diagram presents some key phase relationships in varying FeO - MgO space. Interpreted Latitude Hills metapelitic *post-peak* mineral assemblages (g-cd-sill-bi-sp-ksp-pl-liq-ilm-q) are recognised within the calculated T-X pseudosection ranging from 75-90 % FeO : 10-25 % MgO within a temperature range 760-780 ºC. Increasing temperature within this compositional band results in movement into higher variance fields, with the early loss of biotite and garnet at 770 ºC and 790 ºC, respectively. Garnet at 4.4 kbar requires FeO-rich composition and is metastable at compositions less than ~75% FeO. Cordierite is stable in MgO-rich compositions and is metastable at compositions where MgO

is ≤10 %. Biotite is present at low temperatures between both compositional end-members, however biotite becomes stable with magnesian compositions >90 % to high temperatures and co-exists with orthopyroxene at ≥1040 ºC. Quartz becomes more stable in higher temperatures in iron-rich compositions. Sillimanite is generally more stable at higher temperatures in iron-rich bulk comp at 4.4 kbar.

Calculation of the T-X diagram calculated from the chemical composition from Figure 9, White et al. (2007), identified mineral assemblages that are present in metapelites from the Latitude Hills. These mineral assemblages are stable under Fe-Mg compositions of approximately 80% FeO and 20 % MgO. Considering this ratio, the total MgO + FeO was recalculated to suit the observed mineral assemblage at that iron-magnesium composition where: 2.68 % MgO and 10.56 % FeO was converted to 2.46 % MgO and 11.21 % FeO. In addition to this, the bulk composition to Figure 9 from White et al. (2007) was dehydrated to reflect the anhydrous mineral assemblage following the method described above and resulted in the reduction of H_2O from 5.14 to 2.06 Mol %. The resulting bulk composition is presented in Table 6.

The adjusted bulk composition from Fig. 9a, White et al. (2002) was used to calculate a P-T pseudosection for the Latitude Hills (Fig. 14). Peak mineral assemblages are interpreted from the photomicrographs and the element map constructed from sample MHLH-7 (Figs. 8-11) to be garnet + sillimanite + quartz + spinel + alkali-feldspar + liquid. This quinivariant field (indicated with red star) is narrow and oblique and constrained to 825-1050 ºC and pressures of 5.5 – 10 kbar (Fig. 14). It is unclear due to incomplete resorption of garnet by plagioclase, biotite and K-feldspar whether garnet constitutes the peak mineral assemblage or is a relict prograde/near peak metamorphism mineral. The presence of alkali-feldspar as peak

assemblage places a maximum temperature constraint on peak metamorphic assemblages to 950-1000 ºC and between 5 and 7 kbar. The post-peak mineral assemblage cordierite + plagioclase + biotite + K-feldspar + liquid + spinel is constrained to the field marked with a green star. The field is limited to ≥700 – 760 ºC and 3 – 4.3 kbar (Fig. 14). The field is constrained by the up-pressure, garnet-in line and the up-temperature, biotite-out line.

Establishing stable mineral assemblages in new chemical systems, requires the use of a T-X pseudosection. and to demonstrate reliable conversion, the T-X diagram is presented in Figure 15. The left-hand axis is the starting composition (Fig.14) and the right hand axis is the chemical system calculated from square 5. Pressure is set at 5 kbar and reaction lines that intersect that pressure from Figure 14 are reaction lines that project from the left-hand axis. As reaction lines are calculated from one composition to another, mineral stability fields change, until stable mineral assemblages intersect the right-hand axis and represent stable mineral assemblages in the new composition from 600-1100 ºC at 5 kbar.

The calculated pseudosection for MHLH-7 square 5 is presented in Figure 16. The peak assemblage interpreted from thin section and element map analysis is garnet + sillimanite + spinel + quartz. The presence of quartz, places an important constraint on peak metamorphic conditions. The quartz-in field calculated in the pseudosection occupies a small field in P-T space. The field is triangular, ranging 950 – 1025 ºC at 6.25 – 7.8 kbar and is marked with a red star (Fig. 16). Post-peak mineral assemblages are cordierite + biotite and minor magnetite. Growth of cordierite is restricted to lower pressures than peak metamorphic conditions and magnetite places an important constraint on post-peak conditions. Two fields are present in the pseudosection that can constrain post-peak conditions, these are: spinel + garnet + cordierite + biotite + magnetite + plagioclase + ilmenite + sillimanite and spinel +

garnet + cordierite + biotite + magnetite + plagioclase + ilmenite, where sillimanite is absent in the down-pressure field – Figure 16. It is not determined whether the sillimanite-out line is crossed in post-peak conditions and is discussed later. P-T constraints for post peak assemblages range, ≤700 – 850 ºC and 4.25 – 6.4 kbar. Additionally orthopyroxene does not occur in sample MHLH-7, therefore peak and retrograde mineral assemblages are confined to P-T above the orthopyroxene-in reaction line at: 700 ºC at 4.25 kbar extending to 1100 ºC at 7.4 kbar – Figure 16.

Geochronology

Three samples from the Latitude Hills were selected, representing lithological units from the southern, central and northern regions of the Latitude Hills. Two metapelitic samples (187247 and MHLH-7) on the basis that geochronological data from the metapelites would compliment results from thermodynamic modelling from the same lithological unit. An additional sample was taken (1872321) approximately 10 kilometres from the thermodynamically modelled metapelite with intent to extend geochronology across the Latitude Hills area.

Samples were crushed at the University of Adelaide, South Australia. Sample sizes were typically ~500 cm^3 and were crushed in a jaw crusher and later passed three times through a smaller jaw crusher to reduce overall chip size. The resultant milled rock was sieved simultaneously through 79 and 400 μm mesh. The 79-400 μm fraction was reduced in size through hand panning, and zircon concentrate was produced using magnetic separation and heavy liquid (methyl iodide) separation. Approximately 70-120 zircons from each sample were mounted that adequately represented typical morphology and quality of zircon in the zircon concentrate. In addition to zircons, monazites were also hand-picked, mounted and grouped adjacent to zircons from respective samples with the CZ3 zircon standard at the centre of the mount. The mount was then sent to Geological Survey of Western Australia where the mount was polished and zircons sectioned to approximately half diameter. The mount was then photographed using transmitted and reflected light and cathodo-luminescence (CL) detectors at Curtin University.

The following analytical details were obtained from Wingate and King, (2007, unpublished). Sample 187231 was analysed using SHRIMP IIb (Super-High Resolution Ion Microprobe),

housed at Curtin University on the 31st August 2007, resulting in 3 analyses (1.1-3.1) with four analyses of the CZ3 standard that indicated an external spot-to-spot uncertainty of 0.0% (1σ) and a $^{238}U/^{206}Pb^*$ uncertainty of 0.26% (1σ). Analyses 4.1 to 50.1 were obtained on 4th September 2007 using SHRIMP IIa. One standard analysis was excluded as an outlier and the remaining analyses indicated an external spot-to-spot uncertainty of 0.0% (1σ) and a $^{238}U/^{206}U^*$ calibration uncertainty of 0.20% (1σ). ^{204}Pb isotopic compositions between standards and unknowns did not vary greatly with common lead corrections established by the method of Stacey and Kramers (1975).

Sample Description

Sample 187231 is a clinopyroxene + quartz + garnet + plagioclase + magnetite-bearing, paragneiss. Characteristically, clinopyroxene is shielded from the matrix by a double corona – the first coronal shell is a moat of quartz which is then surrounded by a laminar-to-globular quartz-garnet symplectite - Figure 17a & b. The matrix is comprised of large grains of plagioclase and lesser K-feldspar with plagioclase occurring with blebby antiperthitic texture. Abundant opaque phases are present, with magnetite the dominant phase (Fig. 17b).

CL imaging of zircons revealed complex internal structures including concentric zoning patterns, truncation of zoned areas and metamorphic overgrowths. Overgrowths are variably sized, typically low in uranium (~10-60 ppm U), producing high-CL responses. Cores are often high in uranium (120-215 ppm U) producing a dark response in CL imaging, while many zircons contain complex oscillatory zones. Dark, circular inclusions near the centre of grains are common (Corfu et al., 2003), (Fig. 18).

Results

Two sessions of analysis yielded 53 analyses from 50 zircons. 47 analyses targeted rims with the remaining 6 analyses targeting zircon cores (Table 7). Graphic presentation of uncorrected $^{207}Pb/^{206}Pb$ using the Terra-Wasserberg plot (Fig. 19), shows that most data are concordant or near concordant and plot above the Concordia. A calculated model 1 solution, with a ± 95 % confidence interval, was applied to the data. Results reveal an upper intercept at 1372 ± 86 Ma and a lower intercept at 937 ± 140 Ma, with a Mean Squares of Weighted Deviation (MSWD) of 2.8, where a MSWD value >1 indicates geological variability is influencing age data over instrument variability. Two discrete age populations are present, with the first population centred at ~1180 Ma, with an age spread ranging from 1220 to 1130 Ma. The second population, measured from 6 zircon rim analyses, is centred above ~1100 - 1060 Ma (Fig. 19).

Considering that the ages plot below the concordia due to the possible addition of ^{204}Pb, a common lead correction was applied to the dataset (Fig. 20). Results from the ^{204}Pb correction give $^{207}Pb/^{206}Pb$ ages with an applied lower intercept of 1231 ±140 Ma and an upper intercept at 1364 ±300 Ma and a MSWD of 2.6. The effect of applying a ^{204}Pb correction resulted in increased dispersion of data resulting in data becoming more discordant or data becoming significantly reversely discordant. Additionally, the two age populations visible in Figure 20, merge and become indistinguishable (Fig. 21).

Considering the effect of the ^{204}Pb correction, a scatterplot was constructed, examining the relationship between ^{204}Pb corrected $^{207}Pb/^{206}Pb$ ages and the percent of common lead (Fig. 21). The scatterplot shows a strong, negative correlation ($r = 0.84$) between ^{204}Pb corrected $^{207}Pb/^{206}Pb$ ages. The negative correlation indicates that the ^{204}Pb correction is inaccurate.

Given this scenario, a substitute for the inaccurate ^{204}Pb correction is the ^{207}Pb corrected ^{238}U/^{206}Pb* age data which assumes total measured lead is a mixture of radiogenic (^{206}Pb and ^{207}Pb) and non-radiogenic lead (^{204}Pb and ^{206}Pb). The ^{207}Pb-corrected age is determined by shifting the total measured lead along the mixing line to concordia (Wingate and King, 2007). Uncorrected ^{207}Pb/^{206}Pb age data are generally concordant or near concordant (Fig. 19) and are strongly affected by the ^{204}Pb correction (Fig. 20), resulting in increased dispersion, discordance and reverse discordance. However, due to the generally concordant dates of uncorrected data, uncorrected ^{207} Pb /^{206}Pb dates, ^{204}Pb corrected and ^{207}Pb corrected, there is no significant difference in most ages (Table 6).

Age data for ^{207}Pb corrected ^{238}U/^{206}Pb dates were processed using: 'Unmix Ages' from Isoplot ver.3.24. The resulting Probability Density diagram (Fig. 22), show four age peaks within the U-Pb age spectrum. Using a maximum-likelihood mixture modelling approach (Sambridge and Compston, 1994) rim analyses define four age peaks with a 2σ fit (± 95 % conf. int.) at 1081.8 ± 11, 1151.6 ± 10, 1211.4, ± 12 and 1297 ± 36 Ma. Zircon core ^{207}Pb corrected ^{238}U/^{206}Pb ages range, 1203 – 1370 Ma, however, due to the lack of a statistically viable sample population, reliable interpretation of these dates is limited, however, core dates presented in Table 7, coincide with published age data from the West Musgrave Province, (Clarke et al., 1995; Kelly et al., 2006; Sun et al., 1996; White et al., 1999).

Laser trace element analysis

Laser trace element analyses were conducted on zircons analysed by SHRIMP II for the purposes of Rare Earth Element analysis and thermometry using the titanium-in-zircon thermometer. Trace Element and Rare Earth Element (REE) analyses from zircon cores and rims were performed by LA-ICPMS, on an Agilent 7500cs ICPMS equipped with a New Wave 213 nm Nd-YAG laser at Adelaide Microscopy, The University of Adelaide. Beam diameter was set at 35µm using a repetition rate of 5 Hz which produced a laser power density of ~14-16 J cm^{-2}. Data were collected using time-resolved data acquisition in fast peak-jumping mode and processed using the GLITTER software (Van Achterbergh et al., 2001). Total acquisition time per analysis was 100 seconds; 40 seconds background measurement followed by 60 seconds of sample ablation. Calibration was performed against the NIST610 and NIST612 standard glasses using the coefficients of Pearce et al. (1997). NIST 610 was run twice followed by one analysis of NIST 612 at the beginning and end of a run and ten analyses of unknowns. U^2O^3 was used as the internal standard, applying previously determined absolute values from SHRIMP IIa and SHRIMP IIb analyses. Precision based on repeated analyses of standards is approximately ±10% for concentrations <10ppm and typical detection limits for REE in this study ranged from 0.04-0.6 ppm.

Of the 53 analyses from 50 zircons analysed on the SHRIMP IIa and IIb machines for geochronology, 43 analyses were completed from 42 zircons, with 38 rim analyses and 5 core analyses (Table 8). Laser ablation samples were taken over SHRIMP II pits, with pits typically 10 µm larger in diameter compared to SHRIMP pits.

Rare Earth Element (REE) analysis

Rare Earth Element data collected from zircon trace element data are normalised to chondrite after Boynton (1984) and presented in Table 9 and Figure 23. REE analysis of zircon cores and rims from the Latitude Hills showed several distinctive and consistent trends in REE composition in zircon. Analysis revealed a strong, positive cerium anomaly in zircon cores (Ce/Ce* = 5.95) and zircon rims (Ce/Ce* = 8.56) (Fig. 23 and Table 9). Light Rare Earth Elements (LREE) have a steep positive slope towards the Middle Rare Earth Elements (MREE) (Fig. 23). From the MREE to the Heavy Rare Earth Elements (HREE) a strong positive slope both zircon cores and rims are characterised by a strong, negative europium anomaly. Zircon cores have Eu/Eu* = 0.30 and zircon rims have Eu/Eu* = 0.33 (Fig. 23) and Table 9. Although chondrite normalised (Boynton, 1984) values have a broad vertical spread in REE element concentrations, the pattern of distribution, that is, a concentration increase towards HREE, positive anomaly for Ce and negative anomaly for Eu is the same for all samples (Fig. 23).

Ti in Zircon Thermometry

Titanium was included in trace element analyses in zircon as a viable method for determining crystallising temperatures of zircon cores and rims. Titanium in zircon is a useful thermometer because both Ti and Si are tetravalent cations and therefore do not require addition charge balance within the zircon crystal lattice and activity of TiO^2 in zircon is currently understood to be well constrained (Watson et al., 2006). Titanium content in zircon has a linear, temperature dependant relationship with increasing Ti^{4+} exchange for Si^{4+} at higher temperatures (Watson et al., 2006).

Results from titanium-in-zircon analysis zircon rims show a wide range of titanium concentrations from 88.69 - 11709.05 ppm; and in zircon cores 1185.84 – 2098.46 ppm – Table 9. Crystallising temperatures were calculated using the method of Watson et al. (2006):

$$\log(Ti) = (6.01 \pm 0.03) - \frac{5080 \pm 30}{T(\mathrm{K})}$$, (Watson et al., 2006).

Calculated temperature estimates from the Ti in zircon dataset range from 977.58 ±18.75 to 2343.56 ±44.92 ºC - Table 10. A temperature vs time plot is presented in Figure 24. Examination of the temperature vs time relationship shows that zircon ages of ≥1250 Ma have estimated temperatures that are approximately 1500 ºC. Zircon ages between 1100 and 1225 Ma have temperatures of approximately 1300 ºC and zircons younger than 1100 Ma have temperature estimates of 1400 – 1500 ºC.

Discussion

The open-system processes - melt loss is important in the preservation of granulite facies rocks (Vanderhaeghe, 2001; White and Powell, 2002; White et al., 2007). X-ray mapping of metapelite sample MHLH-7, shows that biotite growth is limited and present only in close contact with garnet and feldspar. Interpreted from the interconnected network of plagioclase and K-feldspar indicated by Na, Ca and K element maps (Appendix 2), formation of the microstructural leucosome is consistent with melt generation during prograde-to-peak metamorphism and later crystallisation of melt during retrogression and cooling. It is also inferred from field reconnaissance that significant melt-loss occurred – indicated by significant volumes of leucosome present throughout the project area and contributed to the formation of refractory mineral assemblages and significantly increased preservation potential during retrogression (White and Powell, 2002). Reconciliation of this postulate with published material indicates that significant melt generation and loss occurred, primarily during D_1 1324-1296 Ma (Mt. West Orogeny) due to muscovite and biotite dehydration reactions, with minor dehydration and melt loss during D_2 (Clarke et al., 1995; Kelly et al., 2006; White et al., 2002).

Allocation of H_2O values of 2.06 and 1.10 for Figures 14 and 16 respectively, was in hindsight, generous. Re-evaluation of the model proportions of hydrous mineral phases and estimates of their fluid content would be more realistic if they were calculated at ≤ 1 and ≤ 0.50 mole % respectively. The effect of dehydrating the effective bulk composition of the modelled system is to elevate the solidus to higher temperatures. Dehydration of Figure 9a from White et al. (2007) from 5.14 to 2.06 elevated the solidus from below 700 ºC to 760ºC. The effect of further dehydration will likely elevate the solidus in excess of 800 ºC – 850 ºC.

Dehydration of granulite facies rocks will have significant consequences for the replacement of peak mineral assemblages by growth of retrograde mineral assemblages. Interpretation of the retrograde path from calculated pseudosections may be limited in granulites where open-system processes are identified (Kelsey et al., 2003b) and must consider the effects of dehydration and melt loss (Stüwe, 1997; Vernon, 1996; White and Powell, 2002; White et al., 2002). Dehydration and melt loss will results in the expansion of stability fields of peak mineral assemblages into lower pressure-temperature space (Kelsey et al., 2003b). Additionally, the solidus will increase to higher temperatures and have significant influence in driving the biotite solidus to elevated temperatures – where granulites that have not experienced significant melt loss histories would not remain below the solidus line (Kelsey et al., 2003b). Ultimately, the two variables - reaction kinetics and H_2O content in rocks - remain subject to changes in pressure and temperature through *time* – where time has significant control on the extent of re-equilibration achieved. Dehydrated and diffusively sluggish rocks may retrogress, provided that time is sufficiently large.

Significance of the spinel + quartz assemblage

The high temperatures identified in this paper, places the metapelitic granulites of the Latitude Hills within ultrahigh-temperature granulite facies metamorphic conditions. Supporting evidence for UHT granulite facies classification is provided by the co-existing spinel-quartz mineral assemblage throughout the southern Latitude Hills and is possibly diagnostic of UHT granulites, but spinel + quartz assemblages require careful consideration when used to infer UHT granulite facies conditions (Das et al., 2001; Dasgupta et al., 1995; Kelsey, 2007; White et al., 2002). The occurrence of spinel + quartz in terranes where other UHT mineral assemblages may be reliably determined to have grown in UHT conditions, usually in high Al-Mg metapelitic rocks (Harley, 1998; Kelsey, 2007; Moraes et al., 2002;

Sajeev and Osanai, 2004). However, spinel + quartz in the Latitude Hills is the *only* mineral assemblage documented in this paper that indicate possible UHT conditions and they are present in typically Al-Fe-rich rocks.

The reported occurrence of spinel+quartz as symplectic growth around garnet at near-by Mount West was modelled in the comparatively very Fe-rich bulk composition (43.83 mole %) with high TiO_2 and O = 2.52 and 1.85 respectively in the system KFMASHTO (White et al., 2002). The calculated pseudosection demonstrated that the peak mineral stability field and inferred thermal peak, reached ~860 ºC at approximately 6 kbar. Calculations by White et al. (2002) indicate that high Fe^{3+} (recast as 'O' in the system) has a significant influence on the stability of spinel + quartz and demonstrates that the stability field of spinel + quartz expands into higher pressures and/or lower temperatures, while also remaining stable in UHT conditions. Additionally, calculated pseudosections in higher component systems - NCKFMASHTO, results in higher pressure stability of spinel + quartz compared to lower component systems eg KFMASH and NCKFMASH (White et al., 2007). Bulk compositions used in this analysis were Fe-rich, but did not use high TiO_2 and Fe^{3+} content reported by White et al. (2002), and may restrict spinel stability fields to higher temperatures than would be reasonably expected for typically Fe-rich rocks.

The influence of the other oxides, ZnO and Cr_2O_3, also expand the stability of spinel into lower temperature fields, however the spinel in the southern Latitude Hills has relatively minor amounts of both oxides, generally ≤0.5 wt% (Table 3). Infrequent analyses returned concentrations of ZnO up to ~3 wt% and may reflect exsolution of gahnite or ülvospinel, or preferential partitioning into symplectic spinel-cordierite assemblages (Das et al., 2001; Dasgupta et al., 1995), which is minor compared to other localities for example, the Kerala

Khondalites, where ZnO ranges 4.92 – 9.60 wt% and higher concentrations ZnO and Cr_2O_3 would allow spinel + quartz to be stable at lower temperatures (Dasgupta et al., 1995; Morimoto et al., 2004).

Peak and post-peak metamorphic conditions

Previously published work on granulites in the West Musgrave Province, estimated that metamorphism during the Musgravian Orogeny reached peak metamorphic conditions of 800 - 850 ºC at 6 - 7 kbar (Clarke et al., 1995; Kelly et al., 2006; White et al., 2002). Results presented in this paper are significantly higher, with estimates for peak metamorphism in the Latitude Hills range 900 – 1000 ºC at pressures between 6 - 8 kbar. The absence of mineral assemblages (eg. orthopyroxene and garnet) that are amenable to thermobarometric and y(opx) methods (Harley, 1984a, b, 1998; Kelsey, 2007; Kelsey et al., 2003c; Pattison et al., 2003) makes estimating peak conditions difficult. Two alternative methods were considered for use; 1) contouring modal proportions of minerals in fields where peak assemblages are expected to lie, 2) multiple pseudosections can be used to estimate peak conditions by overlapping observed peak mineral assemblage fields, to give a range of temperatures and pressures (Kelsey, 2007). Of the two methods outlined above, the latter was used and a range of temperatures and pressures derived.

The peak mineral stability field recognised in Figure 14 gives a peak metamorphic temperature range of 900 -1000 ºC at pressures between 6 – 8 kbar, but may extend down to 825 ºC at 5.5 kbar and gives a minimum temperature constraint and indicates that peak metamorphic occurred in conditions above this minima. Peak metamorphism in Figure 16, is controlled largely by the presence of quartz in a restricted area in P-T space and places tight P-T constraints on the peak metamorphic mineral stability field between 950 – 1025 ºC and

6.25 – 7.8 kbar. Consideration of both pseudosections resulted in a down temperature shift of the peak temperature estimate for the quartz-bearing assemblage which occupies an area within the 900-1000 ºC peak mineral temperature range, albeit slightly reduced, (Fig. 16). The revised P-T range is a good match for estimated peak metamorphic conditions estimated in Figure 14. However, to ensure estimates of peak conditions are more robust, the addition of modal proportion isopleths on the pseudosections for minerals such as garnet, spinel and sillimanite and K-feldspar is required. Additionally, six other chemical domains have been identified within the x-ray map of sample MHLH-7, calculation of each of the remaining bulk compositions will also form a thorough and extensive body of work to better constrain peak P-T conditions.

Using the method described above, post-peak metamorphism P-T conditions are inferred using post-peak mineral assemblages interpreted from the incomplete consumption of garnet, growth of cordierite and symplectite relationships of spinel+quartz+cordierite, sillimanite+spinel+cordierite and intergrowth of feldspar and cordierite. During or immediately following peak metamorphic conditions, decompression occurred to moderate depths. The range of decompression occurred from approximately from 6.5 kbar where the garnet-out line was crossed, where garnet becomes metastable and continued to 5 kbar where growth of cordierite after spinel, quartz, sillimanite and garnet. The limited retrogression seen throughout the Latitude Hills, implies rapid cooling to a point where element diffusion was sufficiently retarded and limited retrogression, or the refractory composition of the rocks limited growth of hydrous phases during retrogression (Dasgupta et al., 1995; Kelsey et al., 2003b; Stüwe, 1997; Vernon, 1996; White and Powell, 2002; White et al., 2000; White et al., 2002). D_3 textures from White et al (2002) are recognised in the modelled sample MHLH-7 as fine-grained globular symplectites growing from peak quartz, spinel and sillimanite. The

D_3 possibly overprints earlier retrograde mineral assemblages from the Musgravian Orogeny – making a P-T path difficult to infer. The overprinting texture is caused by late growth of post-peak minerals within reduced equilibrium volumes and is characterised by early growth of magnetite during prograde metamorphism to higher pressures of approximately 5-6 kbar at low temperatures (possibly out of the modelled P-T range) - and then followed by decompression, resulting in the overgrowth of spinel over magnetite at temperatures of 700 to 750 ºC, before being preserved at low pressures and low temperatures. This analysis is consistent with modelling from Mount West (White et al. 2002) but is inconsistent with P-T estimates from other areas throughout the West Musgrave Province for example, Mt. Aloysius, Mt. Gosse and Champs de Mars where estimates range 8 – 11 kbar and above 700 ºC (Clarke et al., 1995; Kelly et al., 2006; White et al., 2002).

Temporal Constraints on the metamorphism of the Latitude Hills

U-Pb SHRIMP analysis of sample 187231- clinopyroxene + quartz + garnet + plagioclase-bearing paragneiss produced four age maxima within 2σ error. These ages are 1081.8 ± 11 Ma 1211.4 ± 13 Ma, 1151.6 ± 10 Ma and 1297 ± 36 Ma and discussed below.

Analyses of 6 sub-hedral to euhedral zircon cores, produced a wide spread of ages. The oldest recorded core ages are 1375 ± 18 Ma and 1362 ± 13 Ma. Morphology and oscillatory zonation implies that the oldest U-Pb ages represent the magmatic growth age of the zircons and possibly represents maximum deposition ages of volcanosedimentary protolith. Based on two samples, which is a statistically unviable sample population, caution is advised with the interpretation. Ages are consistent with recognised dates for protolith deposition for the younger Birksgate Complex (Edgoose et al., 2004; Howard et al., 2006; Wade et al., 2007).

Zircon cores are commonly overgrown by non-zoned, high-CL rims that occasionally truncate concentric zoning patterns are consistent with metamorphic growth. Three samples (231-11.1, 14.1,17.1), identified as zircon rims record distinctly older ages of 1278 ± 20 Ma, 1288 ± 35 Ma and 1289 ± 20 Ma. These zircon rim ages are correlated to metamorphic zircon growth during the Mount West Orogeny – Wankanki granite suite intrusion and combined with other analyses give an age maxima at 1297 ± 36 Ma of zircon rims and one core sample are consistent with the Mount West Orogeny/Wankanki-suite granite emplacement (Howard et al., 2006; White et al., 1999).

Age maxima occurring at 1211.4 ± 13 and 1151.6 ± 10 Ma were derived principally from zircon rims. Sample 187231-48.1 was initially classified as zircon core based on concentric zoning, however re-examination determined zircon core was not examined. The area examined was secondary zoning which is surrounded by an additional high-CL rim. Therefore sample 48.1 probably represents metamorphic overgrowth and is included in zircon rim analysis. The first age maxima at 1211.4 ±13 coincides with recognised ages for the Musgravian Orogeny at 1230 – 1150 Ma. The second age maxima at 1151.6 ±10 Ma coincides with the later emplacement of the Pitjantjatjara Suite granite between 1200 – 1140 Ma and may record the thermal effects from voluminous magmatism throughout the Musgrave Province at that time (Edgoose et al., 2004; Wade et al., 2007).

Nine zircon rims constitute the youngest dated group of zircon rims with an age maxima at 1081.8 ±11. These zircon rims are consistent with metamorphic overgrowths characteristics described above and either record the intrusion of the Giles Complex at 1080 or the D_3 granulite facies metamorphic event, with a recognised date of 1060 Ma (Clarke et al., 1995; Glikson and Ballhaus, 1996; Kelly et al., 2006; White et al., 2002).

Rare earth element patterns within zircon have a distinctive pattern that does not vary between ages. Concentrations do change between zircon cores and rims, with cores showing slight enrichment in all rare earth elements with a strong, positive cerium anomaly and strong, negative europium anomaly that are consistent with crystallisation with plagioclase (Rubatto, 2002b). The positive slope towards the HREEs indicates that zircon cores and metamorphic rims crystallised without the coeval growth of garnet. Therefore, growth of the garnet + quartz symplectite, implies that zircons crystallisation ages pre-date growth of symplectic garnet (Rubatto, 2002b).

Titanium in zircon thermometry

Analysis of the titanium-in-zircon thermometer was problematic. Temperature estimates for zircon crystallisation are geologically unreasonable and remain unexplained. Use of the LA-ICP-MS, followed set guidelines for operation, appropriately tuned and analysis conducted under stable operating conditions, outlined in the methods above. Analysis of trace elements in zircon were calibrated using two methods. First, absolute ppm values of uranium from SHRIMP analyses are used to calibrate unknowns by converting from ppm U_2O_3 wt%. Second, HfO was used by assigning a value of HfO 1 wt% (consistent with average HfO in zircon). Calibrated unknowns were determined to be approximately equal and U_2O_3 was determined to be the most reliable oxide to use for calibration. Both calibration techniques produced normal values for trace elements in zircon, with the exception for titanium which is considerably enriched. Examination of experimental concentrations of Watson et al. (2006) suggests that values of titanium in the range 10 – 50 ppm would yield temperatures of ~650 to ~950 ºC. LA-ICP-MS analyses of zircon yield titanium values approximately two orders of magnitude higher than titanium concentrations that would give geologically reasonable

temperatures (Watson et al., 2006) and using the linear relationship defined in the methods above, produce temperature estimates of 950 – 2300 ºC.

Assuming no mechanical, tuning, calibration error, sample contamination may account for elevated titanium. Potential source of titanium comes from the gold-coat used in SHRIMP analysis (Watson et al., 2006). If residual coating remained during LA-ICP-MS analysis. Investigating this possibility, the sample was CL imaged using the XL-20 scanning electron microscope. Some gold visible as bright blebs in cracks of zircons, however, no analyses were detected over cracks where gold could not be removed and therefore limits gold-coat contamination as a viable source for titanium contamination. The unlikely alternative is that zircons from 187231 are titanium-rich, which may warrant investigation.

Conclusion

The Latitude Hills in the West Musgrave Province, Western Australia, preserve evidence for high to ultrahigh-temperature metamorphism in Birksgate-age (~1400 Ma) (Howard et al., 2006), aluminous, Fe-rich metapelites. Formation and preservation of high-temperature granulites was the result of prograde biotite breakdown and significant dehydration, linked to the D_1 Mount West Orogeny and followed by emplacement of felsic orthogneisses - Wankanki granite. The Mount West orogeny is temporally linked to the Albany-Fraser orogen and regions of Antarctica and may represent amalgamation of the Yilgarn and South Australian craton within the context of the formation of Rodinia (Bodorkos and Clark, 2004; White et al., 1999). Crustal reworking during D_2 – the Musgravian Orogeny, supported by U-Pb zircon rim ages of 1211.4 ±13 Ma, resulted in heating of metapelitic rocks to high to ultrahigh-temperature at low pressures in the range: 900 – 1000 ºC between 6 – 8 kbar. This represents a significant reappraisal of previous peak P-T estimates of 800-850 ºC at 5 - 6

kbar for similar metapelites in the Tomkinson Range. The Musgravian Orogeny is temporally linked with intrusion of the Pitjantjatjarra suite granite which had a thermal influence on paragneisses in the Latitude Hills, given by U-Pb zircon rim age of 1151.6 ±10 Ma. Following this event, intrusion of the Giles Complex and formation of the Warakurna large igneous complex occurred with later tectonothermal activity deforming the Giles Complex during D3, is also recorded with U-Pb zircon rim ages of and 1081.8 ±11 Ma. Metamorphic textures in the Latitude Hills preserve evidence of a tectonothermal event that had only a limited impact on mineral assemblages with minor retrogression driven by maximum temperatures of 700-750 ºC. No evidence exists in the analysed samples for a high pressure event (8-11 kbar) recorded by Clarke et al. (1995). Findings from this study indicate maximum pressures up to 5 – 6 kbars and defined by early growth of magnetite with later overgrowth of spinel. Additional growth of cordierite indicates peak metamorphic conditions of D3 experienced initial, limited decompression followed by rapid cooling.

Additional quantitative work is required to tightly constrain the peak or near-peak metamorphic conditions of the Latitude Hills and this study should be treated as a stepping stone for a greater understanding of the metamorphic history of the ~1400 Ma Birksgate Complex paragneisses and their significance to the Musgrave Block as a whole

Acknowledgments

I would like to thank the traditional owners – the Ngaanyatjarra Council, and Lance Eddy for the privilege to access and work in their country. Special thanks to GSWA for financial and logistical support during field work, in particular, Hugh Smithies and Paul Evins for their guidance and practical assistance. Also to Michael Wingate for his valued efforts in the collection of geochron data from the misbehaving SHRIMP IIb. From Adelaide Microscopy - Angus Netting and Peter Self. My primary supervisors - Alan Collins and Martin Hand for organising my project and for their continued enthusiasm, insight and intensity. Thanks also to Dave Kelsey without whom I would have remained in ignorant bliss and safely distanced from the dark world of THERMOCALC and calculated pseudosections! However, without these diagrams my project would pale to insignificance. Thanks to Justin Payne and Ben Wade for their assistance using the laser and data interpretation. The CERG Postgraduates have also provided me with their assistance and advice throughout the year. I'd like to thank the people in my office – Lachlan Hallett, Catherine Loye, Luke Boehm, Shaun Light, Carly Thorpe and Kylie Matonia. Finally to Thomas Raimondo, a fellow who I have worked with throughout the year and greatly admire.

References

Bodorkos, S., and Clark, D.J., 2004, Evolution of a crustal-scale transpressive shear zone in the Albany-Fraser Orogen, SW Australia: 1. P-T conditions of Mesoproterozoic metamorphism in the Coramup Gneiss: Journal of Metamorphic Geology, v. 22, p. 691-711.

Bohlen, S.R., 1987, Pressure-Temperature-Time paths and a tectonic model for the evolution of granulites: Journal of Geology, v. 95, p. 617-632.

—, 1991, On the formation of granulites: Journal of Metamorphic Geology, v. 9, p. 223-229.

Boynton, W.V., 1984, Cosmochemistry of the rare earth elements: meteorite studies., *in* Henderson, P., ed., Rare Earth Element Geochemistry: Amsterdam, Elsevier, p. 63-114.

Brandt, S., Will, T.M., and Klemd, R., 2007, Magmatic loading in the Proterozoic Epupa Complex, NW Namibia, as evidenced by ultrahigh-temperature sapphirine-bearing orthopyroxene-sillimanite-quartz granulites: Precambrian Research, v. 153, p. 143-178.

Brown, M., 2002a, Retrograde processes in migmatites and granulites revisited: Journal of Metamorphic Geology, v. 20, p. 25-40.

—, 2002b, Ridge-trench interactions and high-T-Low-P metamorphism, with particular reference to the Cretaceous evolution of the Japanese Islands, *in* Treloar, P.J., and O'Brien, P.J., eds., What drives metamorphism and metamorphic reactions?, Volume Special Edition 138: London, Geological Society, p. 131-163.

—, 2006, Duality of thermal regimes is the distinctive characteristic of plate tectonics since the Neoarchean: Geological Society of America, v. 34, p. 961-964.

—, 2007, Metamorphic conditions in Orogenic belts: A record of secular change: International Geology Review, v. 48.

Buick, I.S., Hermann, J., Williams, I.S., Gibson, R.L., and Rubatto, D., 2006, A SHRIMP U-Pb and LA-ICP-MS trace element study of the petrogenesis of garnet-cordierite-orthoamphibole gneisses from the Central Zone of the Limpopo Belt, South Africa: Lithos, v. 88, p. 150-172.

Camacho, A., and Fanning, C.M., 1995, Some isotopic constraints on the evolution of the granulite and upper amphibolite terranes in the eastern Musgrave Block, central Australia.: Precambrian Research, v. 71, p. 155-181.

Clarke, G.L., Buick, I.S., Glikson, A.Y., and Stewart, A.J., 1995, Structural and pressure-temperature evolution of host rocks of the Giles Complex, western Musgrave Block, central Australia: evidence for multiple high-pressure events.: AGSO Journal of Australian Geology and Geophysics, v. 16, p. 127-146.

Clarke, G.L., Daczko, N.R., and Nockolds, C., 2001, A method for applying matrix corrections to X-ray intensity maps using the Bence-Albee algorithm and Matlab: Journal of Metamorphic Geology, v. 19, p. 635-644.

Collins, W.J., 2002, Hot orogens, tectonic switching, and creation of continental crust: Geology, v. 30, p. 535-538.

Corfu, R., Hanchar, J.M., Hofkin, P.W.O., and Kinny, P.D., 2003, Atlas of zircon textures, *in* Hanchar, J.M., and Hofkin, P.W.O., eds., Zircon, Volume 53, Reviews in Mineralogy and Geochemistry, p. 469-500.

Daniels, J.L., 1974, The geology of the Blackstone region Western Australia: Geological Survey of Western Australia, v. Bulletin 123.

Das, K., Dasgupta, S., and Miura, H., 2001, Stability of osumilite coexisting with spinel solid solution in metapelitic granulites at high oxygen fugacity: American Mineralogist, v. 86, p. 1423-1434.

Dasgupta, S., Sengupta, P., Ehl, J., Raith, J., and Bardhan, S., 1995, Reaction textures in a suite of spinel granulites from the Eastern Ghats Belt, India: Evidence for

polymetamorphism, a partial petrogenetic grid in the system KFMASH and the roles of ZnO and Fe^2O^3.: Journal of Petrology, v. 36, p. 777-788.

Droop, G.T.R., 1987, A general equation for estimating Fe3+ concentrations in ferromagnesian silicates and oxides from microprobe analyses, using stoichiometric criteria: Mineralogical Magazine, v. 51, p. 431-435.

Edgoose, C.J., Scrimgeour, I.R., and Close, D.F., 2004, Geology of the Musgrave Block, Northern Territory., Northern Territory Geological Survey, Report 15.

Glikson, A.Y., and Ballhaus, C.G., 1996, The Giles Complex 1: Tomkinson Ranges, *in* Glikson, A.Y., Stewart, A.J., Ballhaus, C.G., Clarke, G.L., Feeken, E.H.J., Leven, J.H., Sheraton, J.W., and Sun, S.-S., eds., Geology of the western Musgrave Block, with particular reference to the mafic-ultramafic Giles Complex, Volume AGSO, Bulletin 239, Australian Government Publishing Service, p. 44 - 70.

Glikson, A.Y., Stewart, A.J., Ballhaus, C.G., Clarke, G.L., Feeken, E.H.J., Leven, J.H., Sheraton, J.W., and Sun, S.-S., 1996, Geology of the western Musgrave Block, with particular reference to the mafic-ultramafic Giles Complex: AGSO Bulletin, 239, p. 41-68.

Hand, M., and Sandiford, M., 1999, Intraplate deformation in central Australia, the link between subsidence and fault reactivation: Tectonophysics, v. 305, p. 121-140.

Harley, S.L., 1984a, An experimental study of the partitioning of the Fe and Mg between garnet and orthopyroxene: Contributions to Mineralogy and Petrology, v. 86, p. 359-373.

—, 1984b, The solubility of alumina in orthopyroxene coexisting with garnet in FeO-MgO-Al2O3-SiO2 and Cao-FeO-MgO-Al2O3-SiO2: Journal of Petrology, v. 25, p. 665-696.

—, 1989, The origins of granulites; a metamorphic perspective: Geological Magazine, v. 126, p. 215-247.

—, 1998, On the occurrence and characterisation of ultrahigh-temperature crustal metamorphism, *in* Treloar, P.J., and O'Brien, P.J., eds., What drives metamorphism and metamorphic reactions?, Volume 138, Geological Society, London, Special Publications, p. 81-107.

Hensen, B.J., 1971, Theoretical phase relations involving cordierite and garnet in the system MgO-FeO-Al2O3-SiO2.: Contributions to Mineralogy and Petrology, p. 191-214.

Howard, H.M., Smithies, R.H., Pirajno, F., Bodorkos, S., and Tyler, I.M., 2005, A relative lithological and tectonic chronology of the Wingellina region, Musgrave Complex, GSWA 2005 Extended Abstracts: Promoting the prospectivity of Western Australia, Volume 2005/5: Perth, Geological Survey of Western Australia, p. 24-26.

Howard, H.M., Smithies, R.H., Pirajno, F., and Skwarnecki, M.S., 2006, Bell Rock, W.A. Sheet 4645:Western Australia Geological Survey, 1:100 000 Geological Series.

Kelly, N.M., Clarke, G.L., and Harley, S.L., 2006, Monazite behaviour and age significance in poly-metamorphic high-grade terrains: A case study from the western Musgrave Block, central Australia: Lithos, v. 88, p. 100-134.

Kelsey, D.E., 2007, On Ultrahigh Temperature Crustal Metamorphism: Gondwana Research, v. Unpublished Manuscript Draft.

Kelsey, D.E., R., P., Wilson, C.J.L., and Steele, D.A., 2003a, (Th+U)-Pb monazite ages from Al-Mg-rich metapelites, Rauer Group, east Antarctica: Contributions to Mineral Petrology, v. 146, p. 326-340.

Kelsey, D.E., White, R.W., and Powell R., 2003b, Orthopyroxene-sillimanite-quartz assemblages: distribution, petrology, quantitative P-T-X constraints and P-T paths: Journal of Metamorphic Geology, v. 21, p. 439-453.

Kelsey, D.E., White, R.W., R., P., Wilson, C.J.L., and Quinn, C.D., 2003c, New constraints in the Rauer Group, Prydz Bay, east Antarctica: Journal of Metamorphic Geology, v. 21, p. 739-759.

Kriegsman, L.M., and Hensen, B.J., 1998, Back reaction between restite and melt; implications for geothermobarometry and pressure-temperature paths: Geology, v. 26, p. 1111-1114.

Major, R.B., and Conor, C.H.H., 1993, Musgrave Block, *in* Parker A.J., ed., The Geology of South Australia., Volume 1, The Precambrian, Bulletin 54., Geological Survey of Australia, p. 156-167.

Marmo, B.A., Clarke, G.L., and Powell, R., 2002, Fractionation of bulk rock composition due to porphyroblast growth: effects on eclogite facies mineral equilibria, Pam Peninsula, New Caledonia: Journal of Metamorphic Geology v. 20, p. 151-165.

Moraes, R., Brown, M., Fuck, R.A., Camargo, M.A., and Lima, T.M., 2002, Characterization and P-T evolution of melt-bearing Ultrahigh-temperature granulites: an example from the Anapolis-Ituacu Complex of the Brasilia Fold Belt, Brazil: Journal of Petrology, v. 43, p. 1673-1705.

Morimoto, T., Santosh, M., Tsunogae, T., and Yoshimura, Y., 2004, Spinel+quartz association from the Kerala khondalites, southern India: evidence for ultrahigh-temperature metamorphism: Journal of Mineralogical and Petrological Sciences, v. 99, p. 257-278.

Mouri, H., Andreoli, M.A.G., Kienst, J.R., Guiraud, M., and de Waal, S.A., 2003, First Occurrence of the rare 'corundum + quartz' assemblage in the high grade zone from the Namaqualand Metamorphic Complex, South Africa: evidence for higher -P, T metamorphism?: Mineralogical Magazine, v. 67, p. 1015-1021.

Mouri, H., Guiraud, M., and Osanai, Y., 2004, Review on "corundum+quartz" assemblage in nature: Possible indicator of ultra-high temperature conditions?: Journal of Mineralogical and Petrological Sciences, v. 99.

Myers, J.S., Shaw, R.D., and Tyler, I.M., 1996, Tectonic evolution of Proterozoic Australia: Tectonics, v. 15, p. 1431-1446.

Passchier, C.W., and Trouw, R.A.J., 2005, Microtectonics, Springer.

Pattison, D.R.M., Chacko, T., Farquhar, J., and McFarlane, C.R.M., 2003, Temperatures of granulite-facies metamorphism: constraints from experimental phase equilibria and thermobarometry corrected for retrograde exchange.: Journal of Petrology, v. 44, p. 867-900.

Pearce, N.J.G., Perkins, W.T., Westgate, J.A., Gorton, M.P., Jackson, S.E., N., C.R., , and Chenery, S.P., 1997, A compilation of new and published major and trace element data for NIST SRM 610 and NIST SRM 612 glass reference materials.: Geostandards Newsletter-the Journal of Geostandards and Geoanalysis, v. 21, p. 115-144.

Powell, R., and Holland, T.J.B., 1988, An internally consistent thermodynamic dataset with uncertainties and correlations: 3. Application methods, worked examples and a computer program.: Journal of Metamorphic Geology, v. 6, p. 173-204.

Rubatto, D., 2002a, Zircon trace element geochemistry: partitioning with garnet and the link between U-Pb ages and metamorphism: Chemical Geology, v. 184, p. 123-138.

—, 2002b, Zircon trace element geochemistry: partitioning with garnet and the link between U-Pb ages and metamorphism: Chemical Geology, v. 184, p. 123-138.

Sajeev, K., and Osanai, Y., 2004, Ultrahigh-temperature metamorphism (1150ºC, 12 kbar) and multistage evolution of Mg-Al-rich granulites from the Central Highland Complex, Sri Lanka: Journal of Petrology, v. 45, p. 1821-1844.

Sambridge, M.S., and Compston, W., 1994, Mixture modelling of multi-component data sets with application to ion-probe zircon ages: Earth and Planetary Science Letters, v. 128, p. 373-390.

Sandiford, M., and Hand, M., 1998, Controls on the locus of intraplate deformation in central Australia: Earth and Planetary Science Letters, v. 162, p. 97-110.

Satish-Kumar, M., 2000, Ultrahigh-temperature metamorphism in Maduri Granulites, Southern India: Evidence from Carbon Isotope Thermometry: Journal of Geology, v. 108, p. 479-486.

Scrimgeour, I.R., and Close, D.F., 1999, Regional high-pressure metamorphism during intracratonic deformation: the Petermann Orogeny, central Australia: Journal of Metamorphic Geology, v. 17, p. 557-572.

Shabeer, K.P., Satish-Kumar, M., Armstrong, R., and Buick, I.S., 2005, Constraints on the timing of the Pan-African Granulite-Facies Metamorphism in the Kerala Khondalite Belt of Southern India: SHRIMP Mineral Ages and Nd Isotopic Systematics: Journal of Geology, v. 113, p. 95-106.

Shaw, R.K., and Arima, M., 1998, A corundum-quartz assemblage from the Eastern Ghats Granulite Belt, India: evidence for high P-T metamorphism?: Journal of Metamorphic Geology, v. 16, p. 189-196.

Stacey, J.S., and Kramers, J.D., 1975, Approximation of terrestrial lead isotope evolution by a two-stage model: Earth and Planetary Science Letters, v. 26, p. 207-221.

Stüwe, K., 1997, Effective bulk composition changes due to cooling: a model predicting complexities in retrograde reaction textures.: Contributions to Mineralogy and Petrology, v. 129, p. 43-52.

Sun, S.-S., Gray, C.M., Sheraton, J.W., and Glikson, A.Y., 1996, Zircon U-Pb chronology and neodymium isotopic study of tectono-thermal and crust forming events in the Tomkinson Ranges, western Musgrave Block, Western Australia.: AGSO Journal of Australian Geology and Geophysics, v. 24.

Van Achterbergh, E., Ryan, C.G., Jackson, S.E., and Griffin, W.L., 2001, Data reduction software for LA-ICP-MS, *in* Sylvester Paul, J., ed., Laser-ablation-ICPMS in the earth

sciences; principles and applications., Mineralogical Association of Canada. Ottawa, ON, Canada. 2001.

Vanderhaeghe, O., 2001, Melt segregation, pervasive melt migration and magma mobility in the continental crust: the structural record from pores to orogens: Physics and Chemistry of the Earth, Part A: Solid Earth and Geodesy, v. 26, p. 213-223.

Vernon, R.H., 1996, Problems with inferring PTt paths in low-P granulite facies rocks: Journal of Metamorphic Geology, v. 14, p. 143-153.

Wade, B.P., Barovich, K.M., Hand, M., Scrimgeour, I.R., and Close, D.F., 2006, Evidence for Early Mesoproterozoic Arc Magmatism in the Musgrave Block, Central Australia: Implications for Proterozoic Crustal Growth and Tectonic Reconstructions of Australia: The Journal of Geology, v. 114, p. 43-63.

Wade, B.P., Kelsey, D.E., Hand, M., and Barovich, K.M., 2007, (In Press) The Musgrave Province; Stitching North, West and South Australia.: Precambrian Research.

Watson, E.B., Wark, D.A., and Thomas, J.B., 2006, Crystallization thermometers for zircon and rutile: Contributions to Mineralogy and Petrology, v. 151, p. 413-433.

White, R.W., Clarke, G.L., and Nelson, D.R., 1999, SHRIMP U-Pb zircon dating of Grenville-age events in the western part of the Musgrave Block, central Australia: Journal of Metamorphic Geology, v. 17, p. 465-481.

White, R.W., and Powell, R., 2002, Melt loss and the preservation of granulite facies mineral assemblages: Journal of Metamorphic Geology, v. 20, p. 621-632.

White, R.W., Powell, R., Holland, T.J.B., and Worley, B.A., 2000, The effect of TiO2 and Fe2O3 on metapelitic assemblages at greenschist and amphibolite facies conditions: mineral equilibria calculations in the system K2OFeOMgOAl2O3SiO2H2OTiO2Fe2O3: Journal of Metamorphic Geology, v. 18, p. 497-511.

White, R.W., R., P., and Clarke, G.L., 2002, The interpretation of reaction textures in Fe-rich metapelitic granulites of the Musgrave Block, central Australia: constraints from mineral equilibria calculations in the system K_2O-FeO-MgO-Al_2O_3-SiO_2-H_2O-TiO_2-Fe_2O_3: Journal of Metamorphic Geology, v. 20, p. 41-55.

White, R.W., R., P., and Holland, T.J.B., 2007, Progress relating to calculation of partial melting equilibria for metapelites: Journal of Metamorphic Geology, v. 25, p. 511-527.

Wingate, M., and King, R., 2007, (unpublished) 187231, cpx-q-g bearing paragneiss, Latitude Hills, West Musgrave Province, Western Australia. Geochronology dataset (unknown), Compilation of geochronology data: Geological Survey of Western Australia.

Wingate, M., Pirajno, F., and Morris, P.A., 2004, Warakurna large igneous province: A new Mesoproterozoic large igneous province in west-central Australia.: Geology, v. 32, p. 105-108.

Wingate, M.T.D., Campbell, I.H., Compston, W., and Gibson, G.M., 1998, Ion microprobe U-Pb ages for Neoproterozoic basaltic magmatism in south-central Australia and implications for the breakup of Rodinia: Precambrian Research, v. 87, p. 135-159.

Zhang, R.Y., Liou, J.G., and Tsai, C.H., 1996, Petrogenesis of a high-temperature metamorphic terrane: a new tectonic interpretation for the north Dabieshan, central China: Journal of Metamorphic Geology, v. 14, p. 319-333.

Figure Captions

Figure 1: Geological map of the Musgrave Province, showing major domains and structures. The red inset defines the location of field area.

Figure 2: Simplified geological map of the Latitude Hills identifying major lithological units identified during field work.

Figure 3: Photographs of lithological units discussed in text: (a) interlayered melanosome-leucosome-gneiss (metatexite), forming the dominant lithological unit in the southern Latitude Hills. (b) Quartzite, interlayered with metapelite, metatexite or calcsilicate. (c) Plagioclase + diopside + scapolite-bearing calcsilicates. (d) Garnet + sillimanite + spinel + quartz + cordierite + antiperthite-bearing metapelite. These are interlayered with quartzite, leucosomes or melanosomes - forming rafts within anatectic terrane. Same shows contact relationship with melanosome. (e) Garnet + sillimanite + spinel + quartz + cordierite + antiperthite-bearing metapelite showing sharp contact relationship within leucosome. (f) Leucosome with intrafolial, isoclinal, rootless folds. The regional fabric is axial planar to the folds (g) Isoclinally folded leucosome in melanosome Folds are axial planar to vertically dipping gneissic layering and occasionally asymmetric. (h) Mafic truncated by splay fault, indicating 3 meters of sinistral displacement. Dyke was not foliated.

Figure 4: Stereonet data for the Latitude Hills. (a) All foliation data for the Latitude Hills, plotted as poles to foliation. All lineation data for the Latitude Hills. (b) Stereonet for the Southern Latitude Hills. Foliation data plotted as poles to foliation (red dots), have a calculated girdle of 13/158 and foliation is plunging 77→158 – indicated by the Beta symbol. Lineations (blue dots) plot along a great circle with similar orientation to the Beta value with

a calculated girdle of 79/279. (c) Stereonet data for the Northern Latitude Hills. Data plotted as poles to foliation (red dots) and have a calculated girdle of 83/102, indicated by the Beta value and plunge 7→282. Lineation data (blue dots) have a calculated girdle of 44/333 and a mean principal direction of 19-263.

Figure 5: Photomicrographs of selected sub-domains in sample MHLH-6, Southern Latitude Hills – micrographs presented in polarized and cross-polarised transmitted light pairs. (a) incompletely resorbed garnet contacting plagioclase with minor intergrowth with biotite (bottom right). Sillimanite is in contact with K-feldspar with quartz intergrowth. (b) globular symplectite of spinel and quartz. Intergrowth includes cordierite + plagioclase + sillimanite. Garnet is commonly separated from spinel by cordierite and occasionally sillimanite and biotite + quartz intergrowth. (c) Garnet embayment with cordierite + K-feldspar + plagioclase intergrowth with minor biotite – separating quartz from garnet. Quartz + garnet + cordierite interpreted to be part of the peak mineral assemblage – based on grain size and reaction coronas forming the post-peak assemblage plagioclase + K-feldspar + cordierite. (d) Garnet separated from quartz by cordierite + K-feldspar + plagioclase intergrowth. Conspicuous spherical zircon in garnet and cd + pl + ksp intergrowth. (e) Contacting spinel and magnetite is separated from quartz by a double corona. The first shell surrounding spinel is sillimanite which is then completely surrounded by laminar intergrowth of plagioclase and cordierite. Matrix comprised of coarse-grained quartz and antiperthite.

Figure 6: Photomicrographs of selected sub-domains in sample MHLH-13, Southern Latitude Hills – micrographs presented in polarized and cross-polarised transmitted light pairs. (a) Coarse-grained, twinned cordierite (centre of micrograph) is flanked on either side of by a globular spinel-cordierite symplectite (left) and fine to medium grained, occasionally

euhedral quartz. Spinel and quartz are no longer in direct contact and are separated by symplectic cordierite with peak spinel remaining in the centre of the reaction. Minor remnant garnet is surrounded by the twinned cordierite and is incompletely consumed. (b) Coarse-grained spinel +magnetite is separated from garnet by euhedral quartz with quartz often in contact with spinel. A fine-grained globular spinel-cordierite symplectite is located in the top left of the image. Plagioclase, K-feldspar, cordierite and quartz exist within the garnet embayment and separate garnet from spinel. Garnet has abundant biotite inclusions. (c) Garnet is located at the centre of this reaction that is rimmed by a moat of plagioclase and cordierite that have euhedral edges. Extending outward from this moat is a globular spinel cordierite symplectite with coarse grained spinel located at the centre of the reaction. Spinel and quartz are not in contact in this example.

Figure 7: Photomicrographs of selected sub-domains in sample MHLH-16, Southern Latitude Hills – micrographs presented in polarized and cross-polarised transmitted light pairs. (a) Garnet and spinel display two relationships – occasionally spinel is enclosed within garnet in direct contact, however, the more common relationship is where spinel is located at the centre of a reaction and is separated from garnet by a narrow moat of cordierite and plagioclase. Garnet also forms narrow ribbons that separate cordierite from plagioclase. Quartz, cordierite and sillimanite are common minerals constituting the matrix. (b) Two morphologies of spinel are observed – coarse grains (interpreted peak spinel) and fine-grained spinel (interpreted post-peak), often intergrown with magnetite and is typically in contact with quartz and occasionally cordierite. Fine-grained magnetite is also observed within quartz with each narrow ribbon (indicated in micrograph) made up buy hundreds of tiny globules of magnetite. (c) Coarse-grained spinel is mantled by fine-grained spinel + cordierite symplectite that becomes cordierite dominant away from coarse spinel. The

reaction is then surrounded by a narrow ribbon of quartz, that encloses the entire domain from the quartz-rich matrix. (d) Garnet porphyroblast has a biotite mantle that separates garnet from quartz. A spinel-cordierite symplectite occurs in contact with garnet with only cordierite in contact with garnet. Cordierite and occasionally biotite separates spinel from garnet.

Figure 8: Photomicrographs of selected sub-domains in sample MHLH-7, Southern Latitude Hills – micrographs presented in polarized and cross-polarised transmitted light pairs – except (a) and (b). (a) view under cross polarised transmitted light of the intergrowth texture that mantles garnet and separates garnet from quartz. Biotite is typically in contact or in proximity to garnet. Away from garnet, biotite is rarely observed. Biotite is often intergrown with plagioclase, K-feldspar and cordierite. Intergrowth between cordierite and feldspar is myrmekitic or vermicular in texture often radiating away from garnet. (b) View is of the relationship between feldspar and cordierite – both coarse-grained morphologies are separated by the intergrowth of the two phases. Quartz has a sharp grain boundary and is in contact with both the intergrowth and coarse grained cordierite and the feldspars. (c) Garnet and spinel are separated by a moat of intergrown sillimanite, biotite and feldspar. Coarse-grained spinel is mantled by fine grained spinel-cordierite symplectite. Although spinel and garnet are separated they are both separated from the quartz-cordierite matrix by K-feldspar and plagioclase with myrmekitic intergrowth occurring between feldspar and cordierite at the reaction front. (d) Sillimanite, cordierite, spinel and magnetite intergrowth is at the centre of the micrograph. A narrow moat of twinned feldspar separates this domain from coarse grained quartz. Note, the similar moat separating garnet from coarse grained quartz – top left corner.

Figure 9: Sample MHLH-7, photomicrograph viewed under cross-polarised transmitted light, with accompanying Mg and Ca intensity X-ray maps highlighting mineral distribution within the intergrowth. Myrmekitic intergrowth of plagioclase, K-feldspar and cordierite occurs within the garnet embayment. Biotite is the dominant mineral phase at the base of the embayment and is also intergrown with cordierite and plagioclase. Bright colours on the Mg-intensity map highlight presence of cordierite, while bright colours in the Ca-intensity map highlight occurrence of plagioclase.

Figure 10: Sample MHLH-7, photomicrograph viewed under polarised transmitted light, with accompanying Fe and Si intensity X-ray maps highlighting mineral distribution within the intergrowth. Spinel is separated from quartz by cordierite. Relict quartz (yellow) in cordierite is seen toward the bottom right corner above the garnet grain. The Silicon intensity map also shows that spinel (blue-purple) forms a corona around magnetite (black) which separates the magnetite from cordierite.

Figure 11: Sample MHLH-7, compound element map from Quantitative X-ray element mapping on metapelitic sample: MHLH-7 from the Southern Latitude Hills. Individual element maps are presented in Appendices 2a and 2b. Mapping was conducted on a thin-section that was not perfectly flat resulting in a gradient of colour intensity from left to right. Quartz grades orange to red and garnet grades from medium intensity blue to light blue. Spinel ±magnetite is dark blue, plagioclase is light green, K-feldspar is green-to-yellow, biotite is yellow and cordierite is light blue. The feldspar present, forms a microstructural leucosome. Numbered squares represent domains where bulk compositions were measured. Square 5 was selected for modelling with calculated pseudosections.

Figure 12: Sample MHLH-7, close-up of square 5 with minerals labelled. Sillimanite is located in the centre of the domain mantled by a moat of cordierite that separates sillimanite from spinel and garnet. Spinel is mantled by a moat of cordierite that separates it from quartz and quartz is also separated from garnet by the same cordierite moat. Biotite is located along the rim of garnet and forms an intergrowth with cordierite and occasionally plagioclase and quartz. A change in the colour intensity of spinel from dark blue to – near black represents late growth of magnetite.

Figure 13: Temperature-Composition diagram calculated in the system NCKFMASHTO. Compositions for the left and right axes are given at the top of the diagram with the MgO-rich end member located on the left-hand axis and the FeO-rich end member located on the right-hand axis. System composition is adopted from fig. 9a in White et al. (2007) and explores the stability of mineral assemblages in varying FeO-MgO compositional space at 4.4 kbar.

Figure 14: Calculated P-T pseudosection in the system NCKFMASHTO for garnet, sillimanite, antiperthite, cordierite and spinel-quartz bearing metapelites from the Southern Latitude Hills. Composition based on the T-X diagram in fig. 13. Proportion of total FeO-MgO was adjusted to suit stable mineral assemblages observed in the Latitude Hills. The Bulk composition was additionally dehydrated from 5.14 to 2.06 Mol% and normalised to the new bulk composition. Bulk composition is given at the top of the diagram.

Figure 15: T-X diagram calculated for conversion from bulk composition in figure 14 to bulk composition in figure 16. Compositions for the left and right axes are given at the top of the diagram with fig. 14 on the left-hand axis and figure 16 on the right-hand axis. The T-X

diagram represents the change in bulk composition from garnet, sillimanite, antiperthite, cordierite and spinel-quartz bearing metapelites to a garnet-rich with sillimanite and spinel-quartz-bearing sub-domain – identified in figs. 11 & 12.

Figure 16: Calculated P-T pseudosection in the system NCKFMASHTO for garnet-rich with sillimanite and spinel-quartz-bearing sub-domain from X-ray-mapped metapelites from the Southern Latitude Hills. Composition is based quantified X-ray map image processed in MATLAB using the Bence-Albee Algorithm (Clarke et al., 2001). Bulk composition is given at the top of the diagram. Stable mineral assemblages were defined using the T-X diagram as a starting point for the calculation of the pseudosection.

Figure 17: Sample 187231: Photomicrograph of a Clinopyroxene-plagioclase-garnet-quartz-magnetite-bearing paragneiss from the Northern Latitude Hills. Left: polarised transmitted light, right: cross-polarised transmitted light. Clinopyroxene and magnetite is mantled by a garnet-quartz symplectite and often in contact with poikiloblast quartz. Plagioclase is typically separated form cpx and mt by the garnet-quartz corona.

Figure 18: Sample 187231: Catholodoluminecent image of zircons extracted and block mounted from sample 187231 - Clinopyroxene-plagioclase-garnet-quartz-magnetite-bearing paragneiss from the Northern Latitude Hills. Zircons commonly show oscillatory zoning patterns in low-CL cores and occasionally these zoning patterns are truncated by a high-CL rim layer. Some zircons show complex zonation patterns and resorption textures along core and rim boundaries. Red dots on zircons identify SHRIMP II and later La ICP-MS analysis locations. The dates attached to each analysis is uncorrected $^{207}Pb/^{206}Pb$.

Figure 19: Sample 187231: Terra-Wasserberg Concordia plot for all 53 zircon analyses showing U-Pb determined ages without ^{204}Pb correction. Error crosses are to 1σ. Data are concordant or near concordant with the majority of dates plotting slightly below the concordia. Several data are strongly discordant or show a trend towards common lead. For statistical analysis, these data are ignored.

Figure 20: Sample 187231: Terra-Wasserberg Concordia plot for all 53 zircon analyses showing U-Pb determined ages with ^{204}Pb correction. Error crosses are to 1σ. Data are strongly affected by the ^{204}Pb correction. Data that were concordant prior to ^{204}Pb correction remain concordant, however, data that were discordant become reversely discordant - some significantly.

Figure 21: Sample 187231: X-Y Scatterplot showing strong positive (R=0.84) between $^{207}Pb^*/^{206}Pb^*$ Ages and f204%. Correlation shows younger $^{207}Pb^*/^{206}Pb^*$ Ages are associated with increasing f204%.

Figure 22: Sample 187231: Probability density curve for U-Pb SHRIMP II determined ages from the Northern Latitude Hills. Age maxima (Ma) calculated to 2σ. Four age components form this plot with age maxima occurring at 1081.8 ±11, 1151.6 ±10, 1211.4 ±13 and 1297 ±36 (Ma).

Figure 23: a steep positive slope from (LREE) towards (HREE). Both zircon cores and rims are characterised by a strong, negative europium anomaly, where zircon cores have Eu/Eu* = 0.30 and zircon rims have Eu/Eu* = 0.33. Analysis shows a strong positive cerium anomaly where zircon cores have Ce/Ce* = 5.95 and zircon rims have Ce/Ce* = 8.56.

Figure 24: Titanium-in-zircon thermometry. Data are plotted as Temperature vs. Age (Ma) to show temporal changes in crystallisation temperatures to indicate possible metamorphic events. Calculated temperature estimates from the Ti in zircon dataset range from 977.58 ±18.75 to 2343.56 ±44.92 ºC.

Table Captions

Table 1: Representative garnet and cordierite microprobe analyses. Recalculated cation data account for Fe^{3+} (Droop, 1987).

Table 2: Representative plagioclase and K-feldspar microprobe analyses. Recalculated cation data account for Fe^{3+} (Droop, 1987).

Table 3: Representative spinel and biotite microprobe analyses. Recalculated cation data account for Fe^{3+} (Droop, 1987).

Table 4: Mineral chemistry summary showing chemical composition ranges in metapelites. P.A.= peak assemblage, R.M. = retrograde mineral assemblage. Y =presence of mineral.

Table 5: X-ray element map, bulk compositions for selected squares.

Table 6: Bulk compositions for calculated T-X diagrams and pseudosections.

Table 7: Zircon analyses from sample 187231. All uncertainties to 1σ.

Table 8: Trace element analysis for sample 187231.

Table 9: Rare Earth Element in zircon for sample 187231

Table 10: Titanium in zircon – concentrations and temperature estimates. All uncertainties to 1σ.

Figure 1: Location of the 2007 honours project area: Latitude Hills, West Musgrave Ranges, W.A.

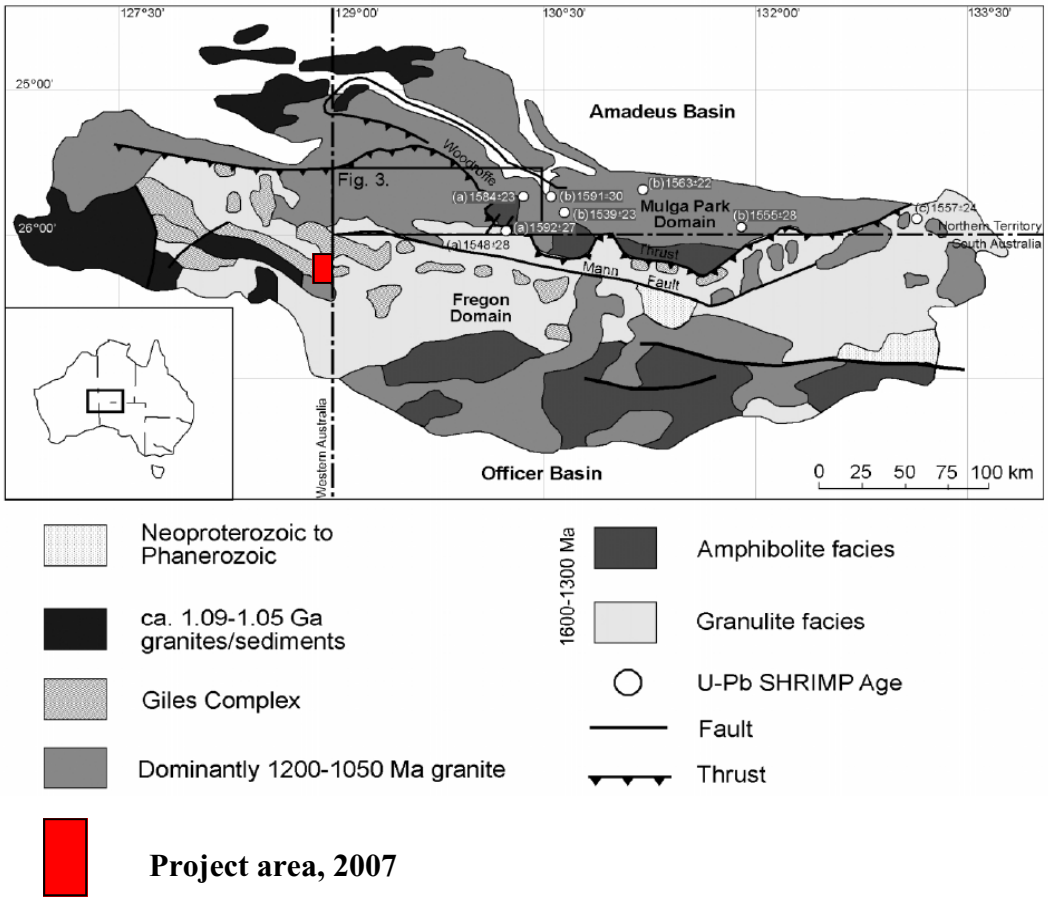

Source: Adapted from figure 2, Wade et al (2006).

Figure 2

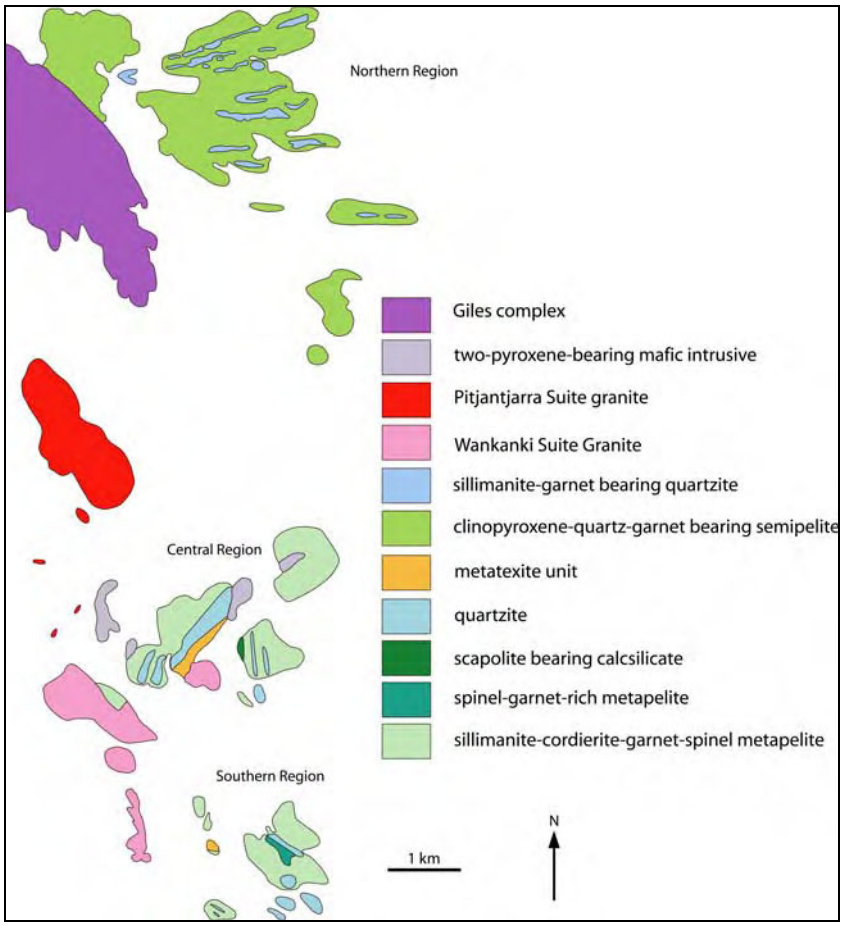

Figure 2: Simplified geological map of the Latitude Hills as identified during field work conducted during May, 2007. Map identified regions referred to in report, locations of rock samples used in petrographic, geochronological and P-T pseudosection analysis. For the complete map, with structural measurements and interpretation and stratigraphy see appendix 1.

Figure 3

3a

3b

3c

3d

3e

3f

3g

3h

Figure 4a

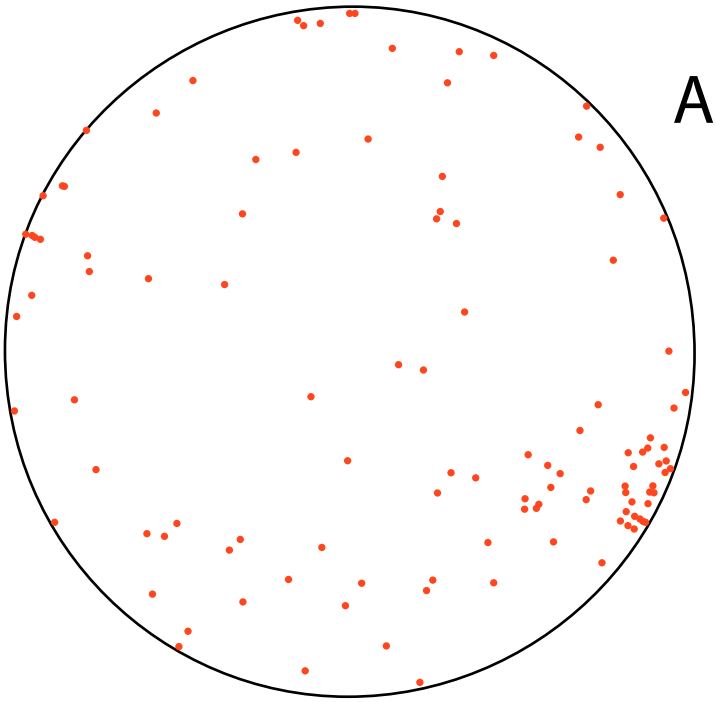

All foliation data

No. of Data = 118
Mean Principal Orientation = 79/299
Mean Resultant dir'n = 38-302
Mean Resultant length = 0.39
(Variance = 0.61)
Calculated. girdle: 14/157
Calculated beta axis: 76-337

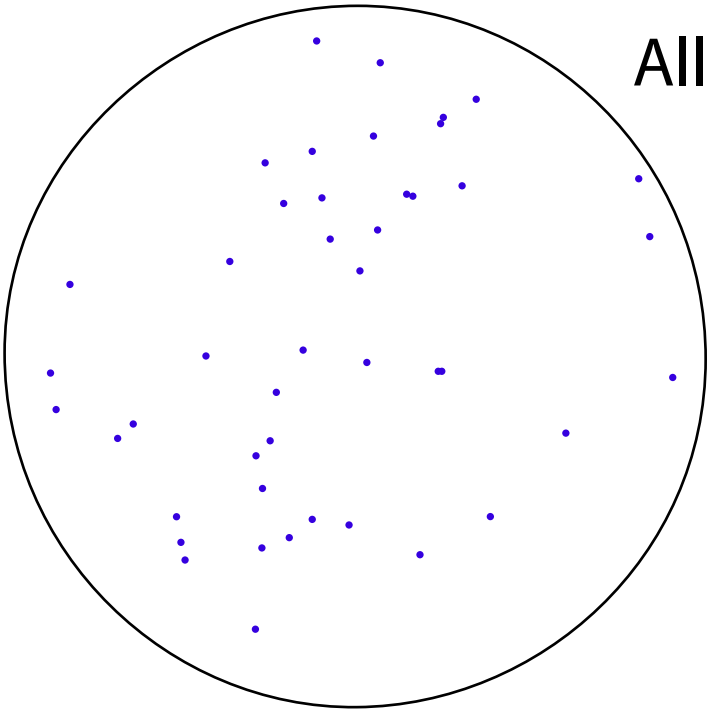

All mineral lineation data

No. of Data = 47
Mean Principal Direction = 73-317
Mean Resultant dir'n = 79/327
Mean Resultant length = 0.61
(Variance = 0.39)
Calculated. girdle: 73/304

Figure 4b

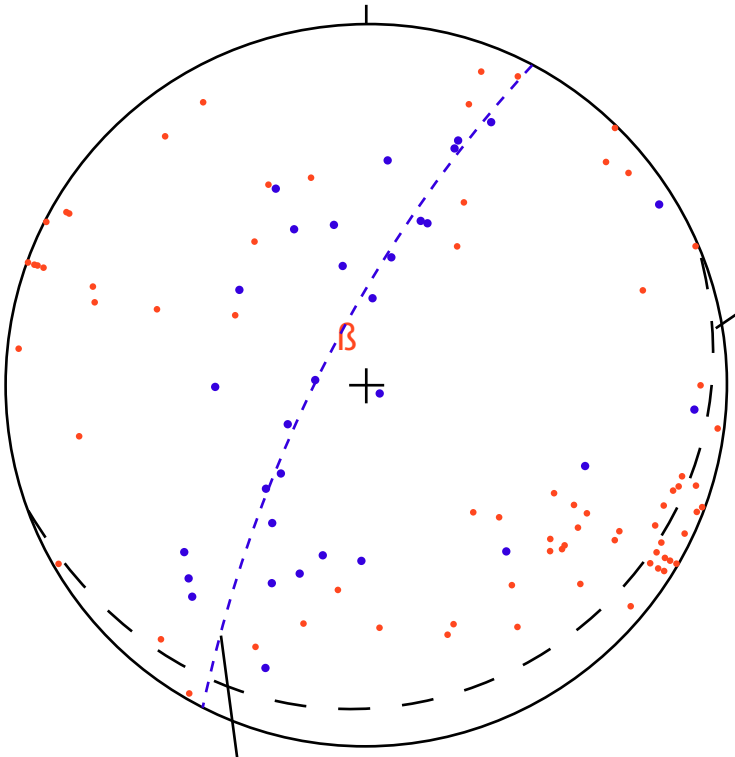

pole to foliation
No. of Data = 76
(Variance = 0.59)
ß Calculated beta axis = 77→338
Calculated girdle = 13/158

Lineations
No. of Data = 35
(Variance = 0.34)

Calculated girdle for mineral lineation data = 79/279

Figure 4c

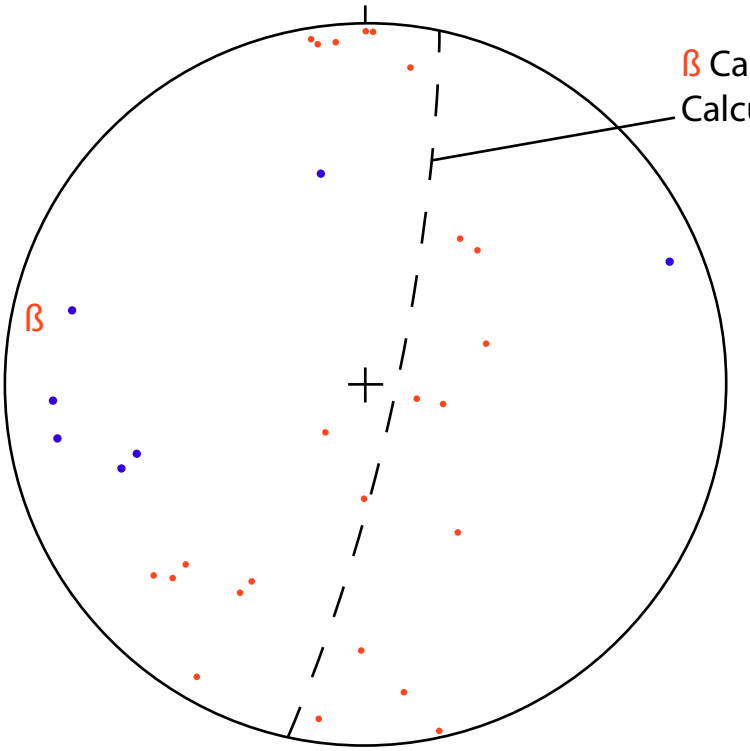

pole to foliation
No. of Data = 24
(Variance = 0.53)
ß Calculated Beta axis: 7→282
Calculated girdle: 83/102

Lineations
No. of Data = 7
(Variance = 0.34)
Calculated. girdle: 44/333
Mean Principal Direction = 19-263

Figure 5 - MHLH-6 Petrography

5a

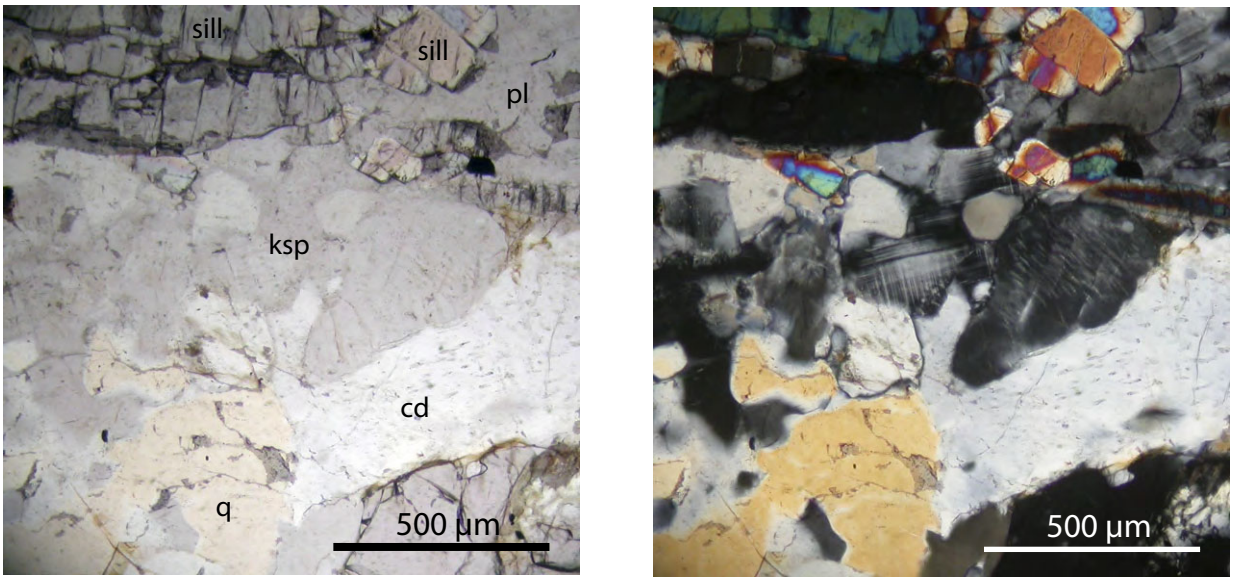

5b

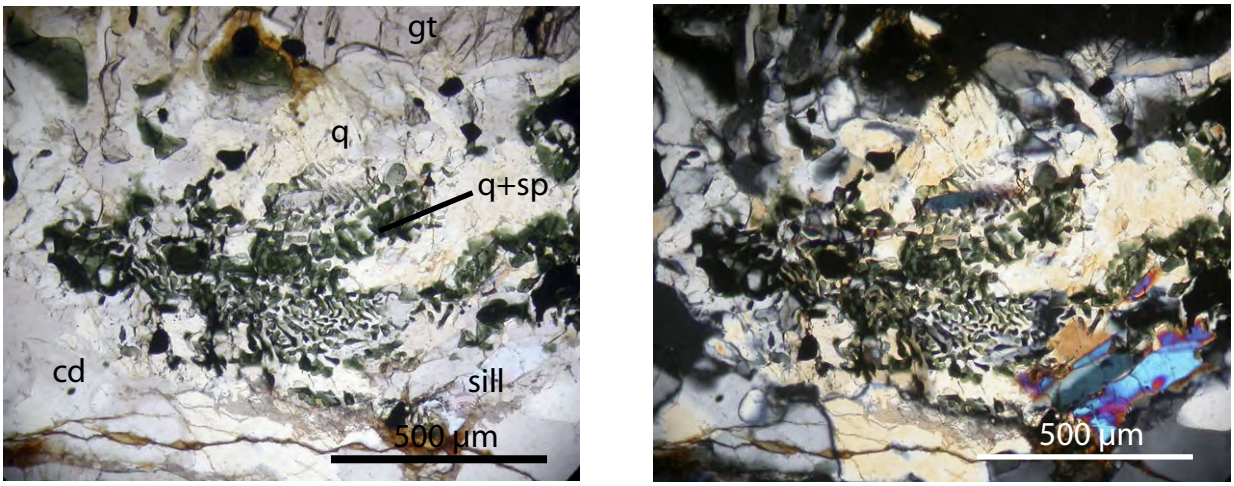

5c

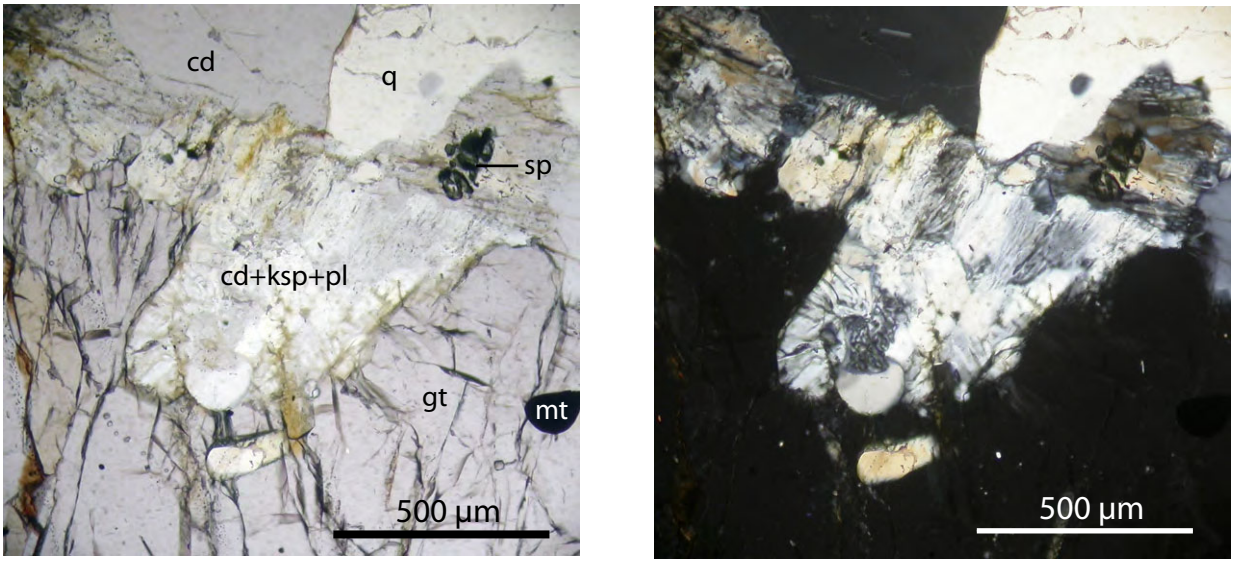

Figure 5 - MHLH-6 Petrogrpahy

5d

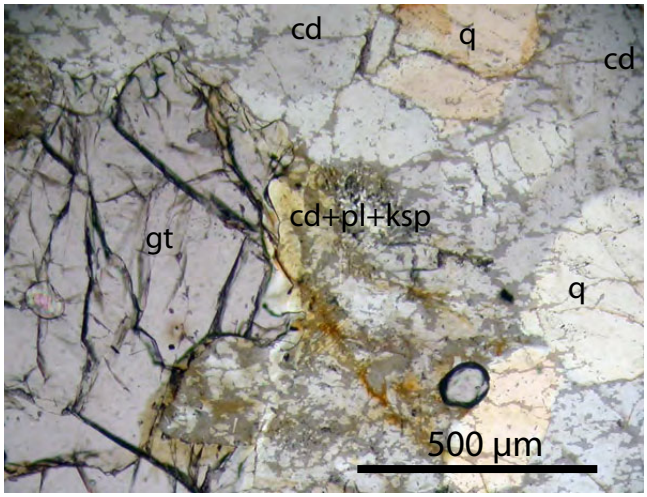

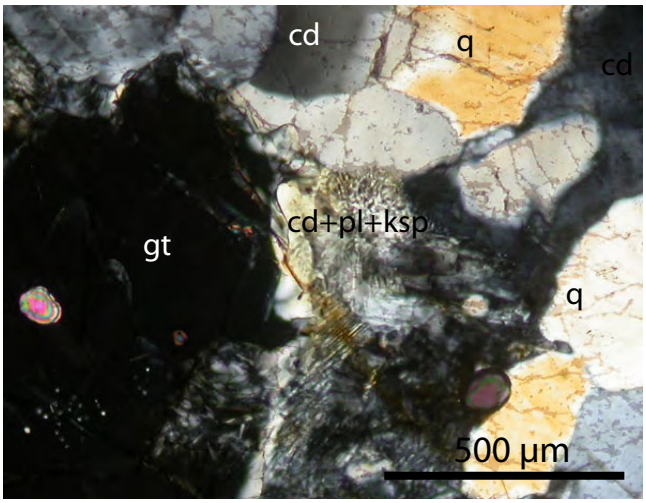

5e

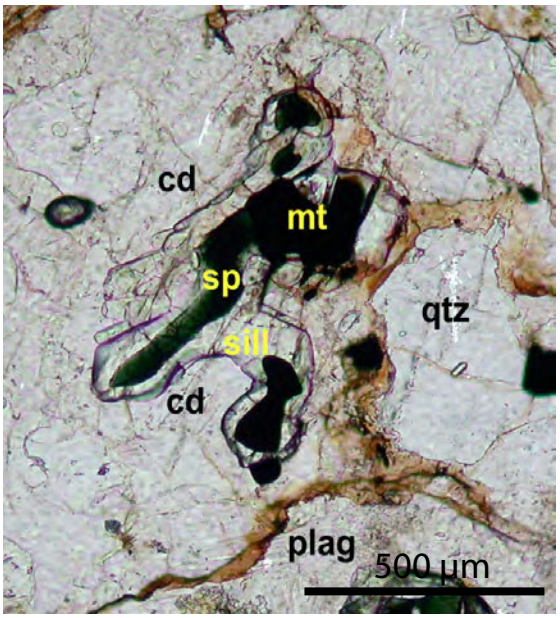

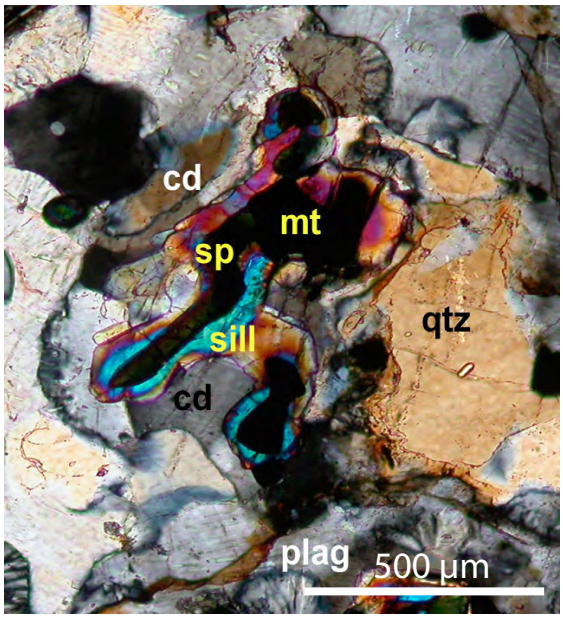

Figure 6 - MHLH-13 Petrography

6a

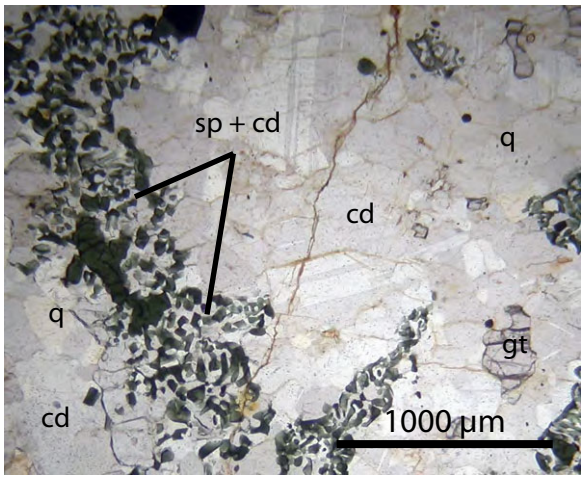

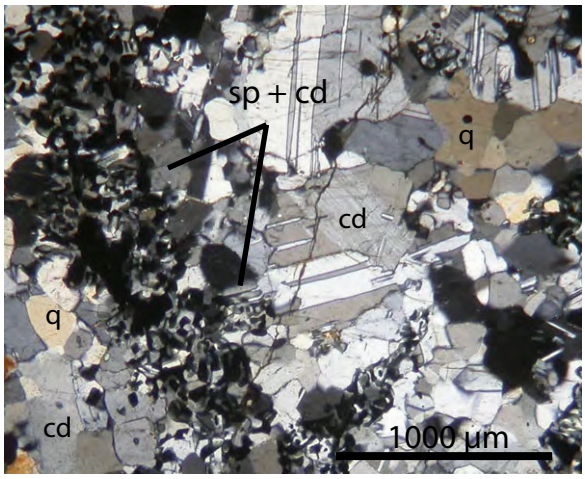

6b

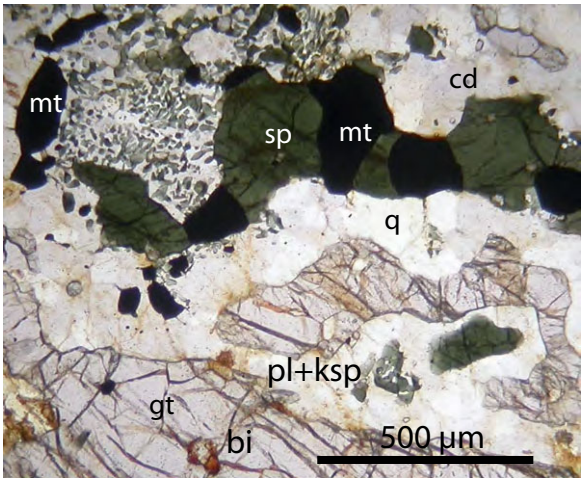

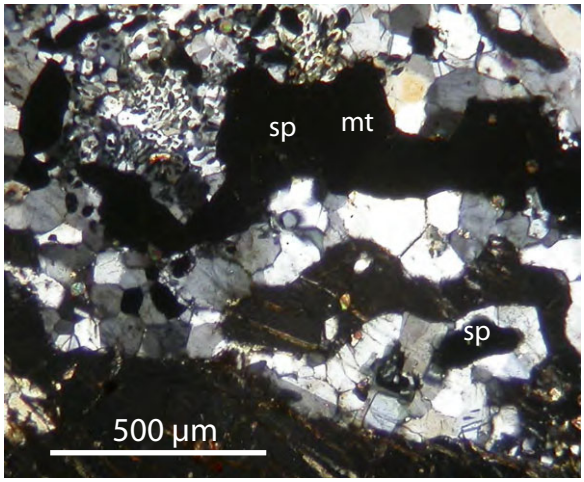

6c

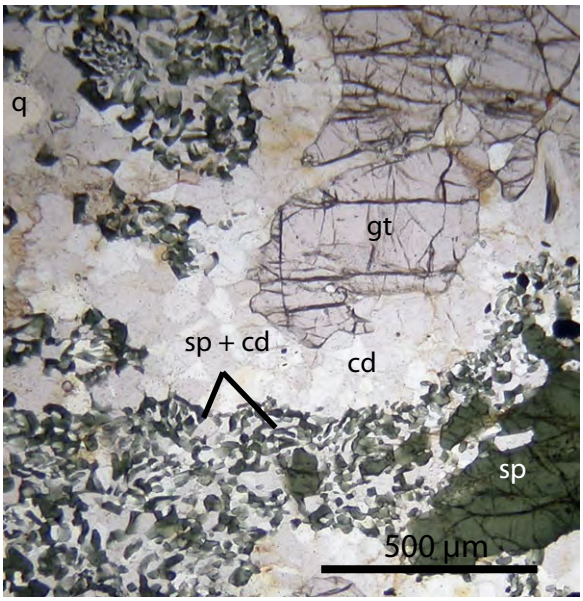

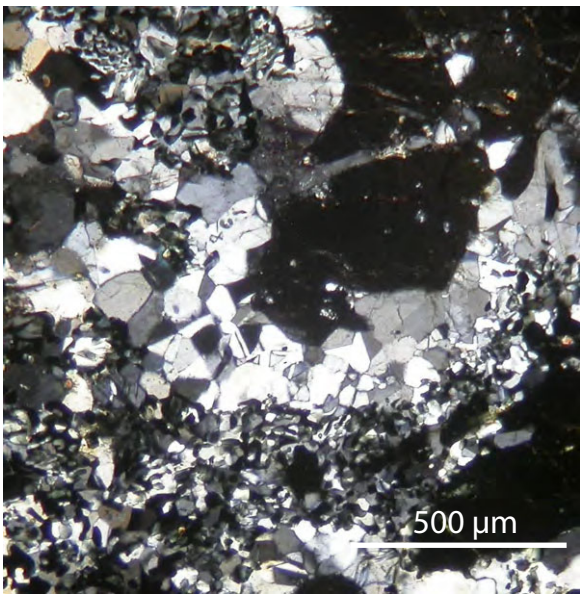

Figure 7 - MHLH-16 Petrography

7a

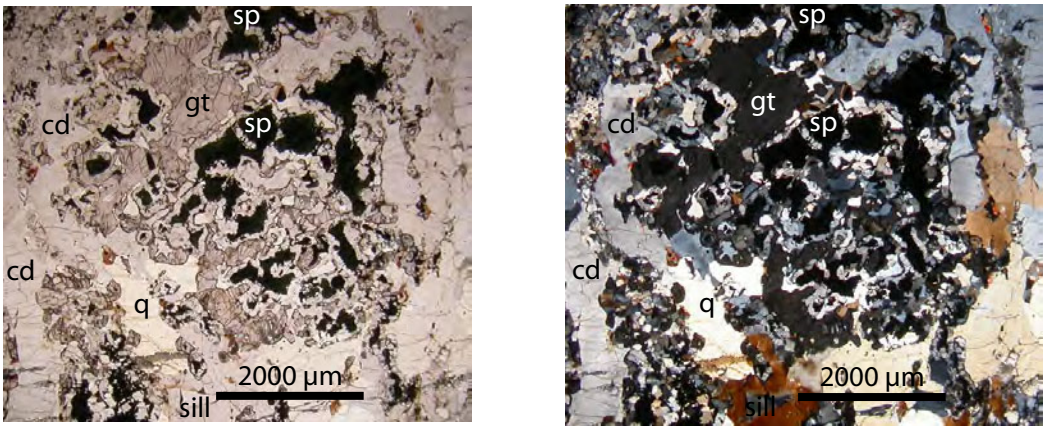

7b

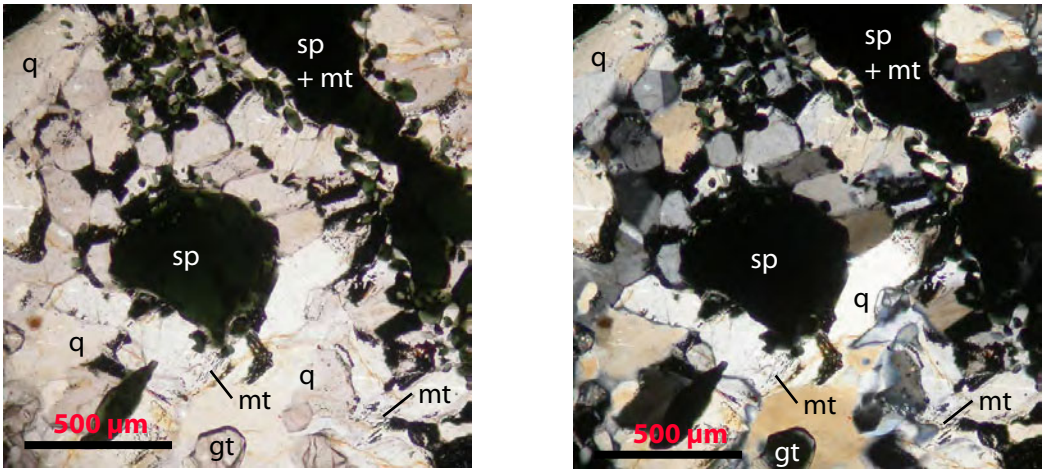

7c

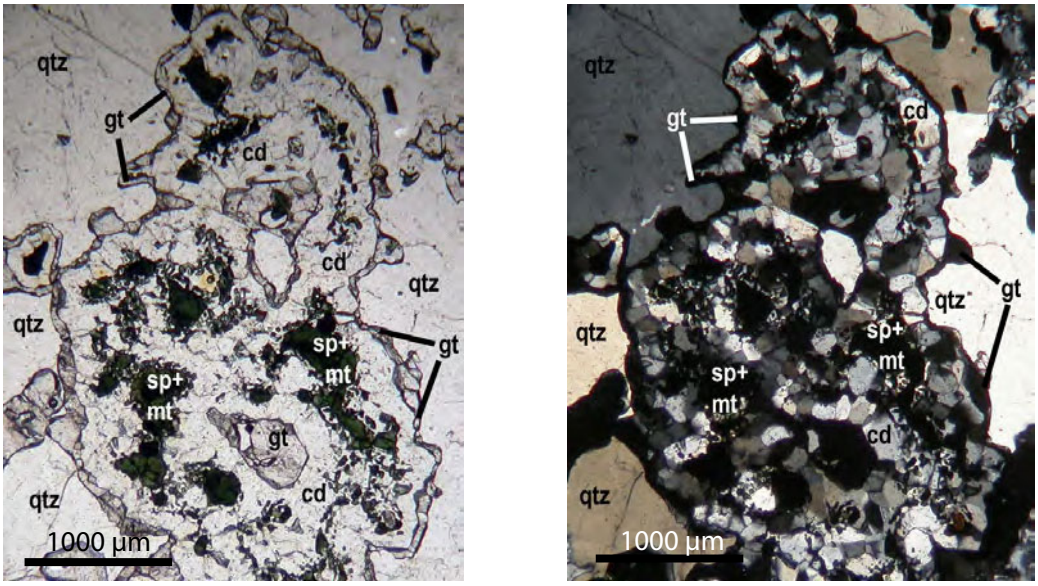

Figure 7 - MHLH-7 Petrography

7d

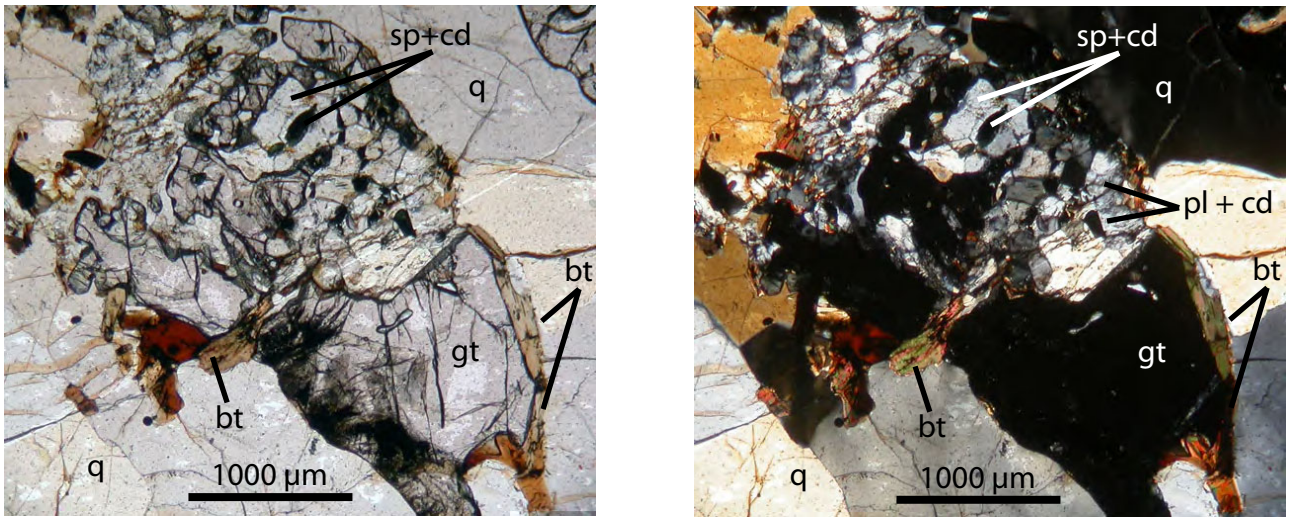

Figure 8 - MHLH-7 Petrography

8a

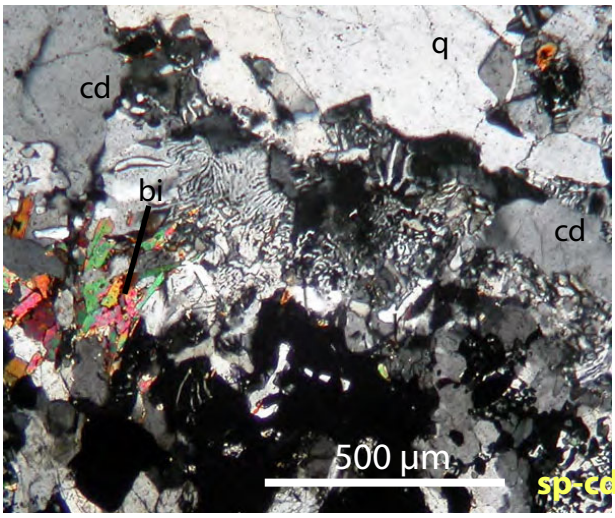

8b

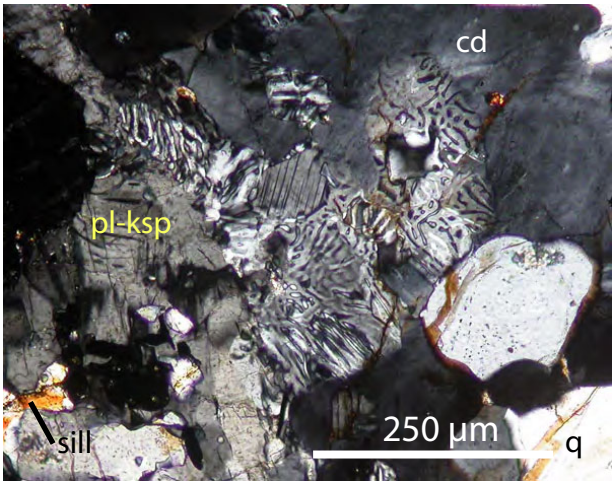

8c

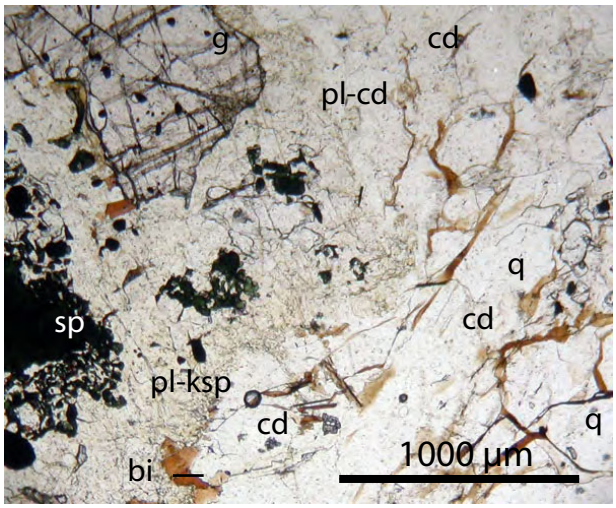

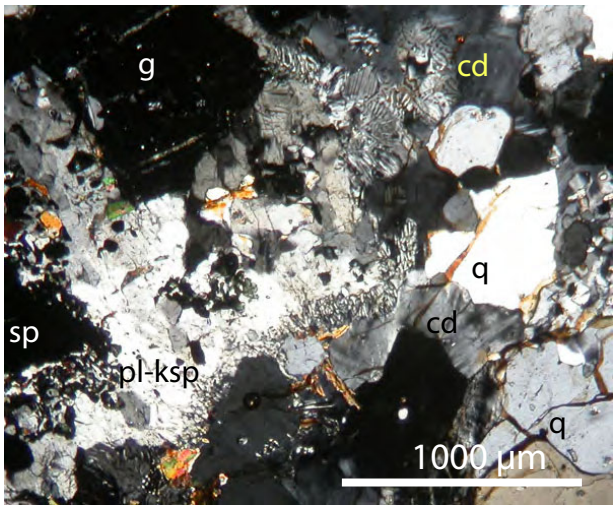

8d

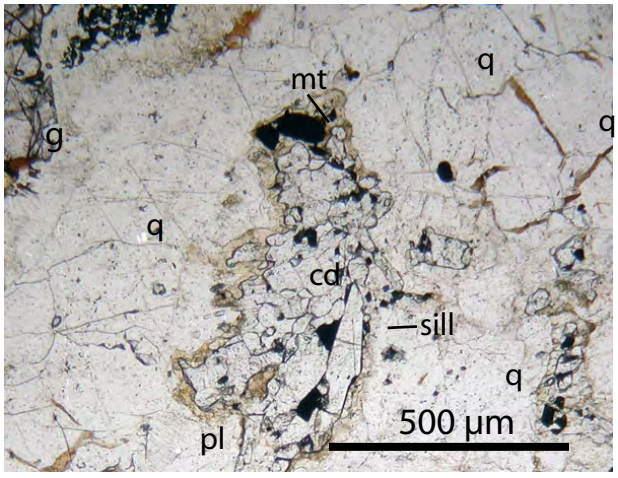

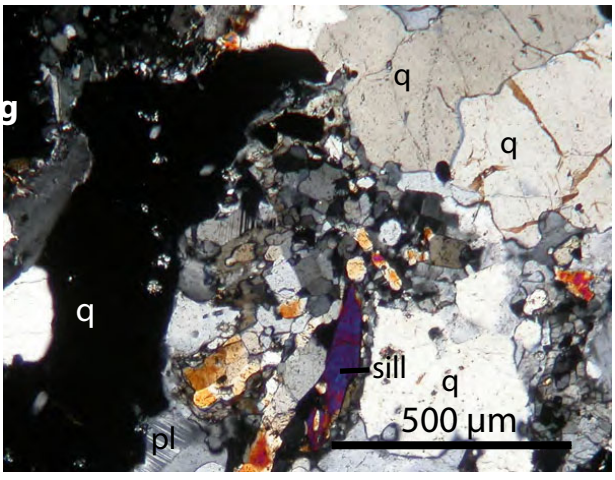

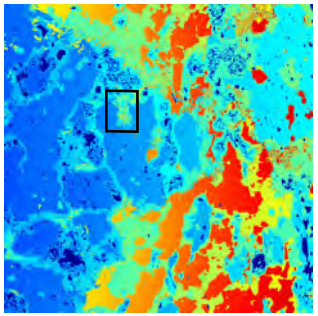

Figure 9

View of an embayment along the edge of a garnet crystal, with particular reference to the growth of cordierite (Mg high) and plagioclase (Ca high).

photomicrograph

Mg intensity map

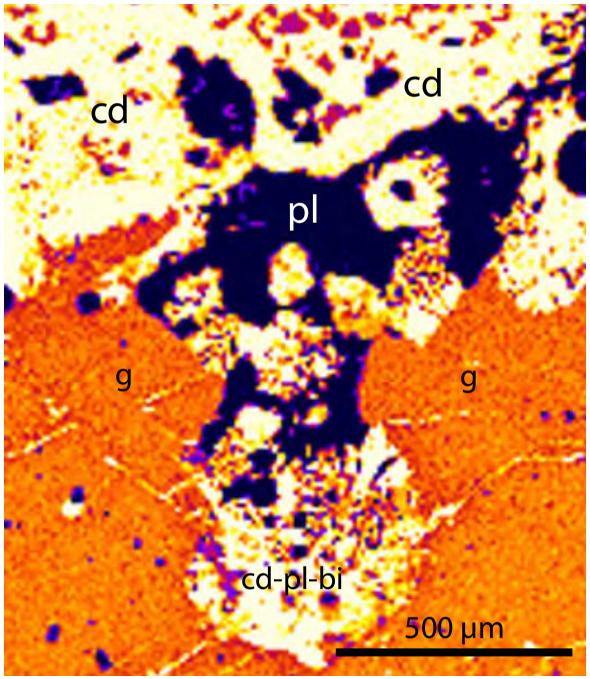

Ca intensity map

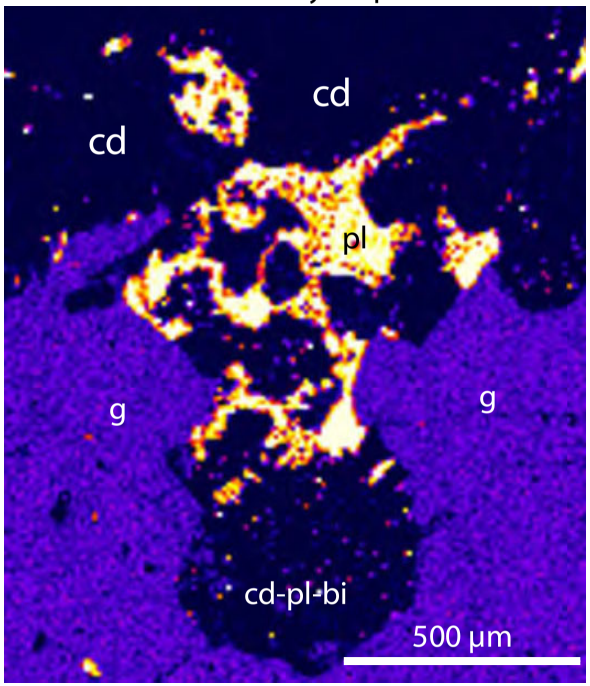

Left to right, photomicrograph viewed under cross polarized transmitted light, x-ray map of magnesium, x-ray map of calcium.

Myrmekitic intergrowth of plagiocalse, K-feldspar and cordierite occurs along the outer rim of garnet. There is also considerable growth of biotite in contact with garnet, deep, within the embayment and is effectively shielded from the matrix by the complex relationship between cordierite and plagioclase. Zoning of Mg is present in garnet, with Mg decreasing towards the crystal edge, particularly where garnet is in contact with cordierite.

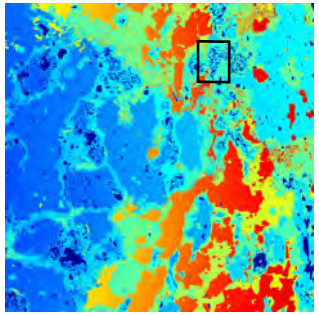

Figure 10

View of a globular spinel - cordierite symplectite.

photomicrograph

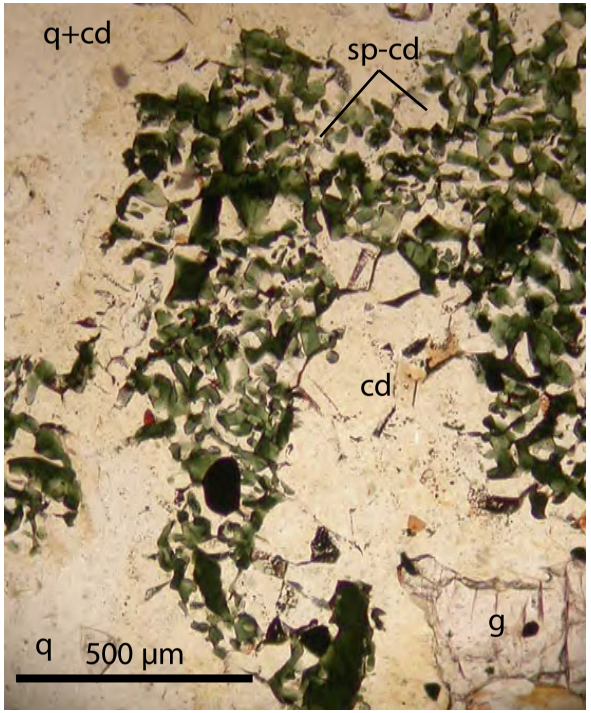

Fe intensity map

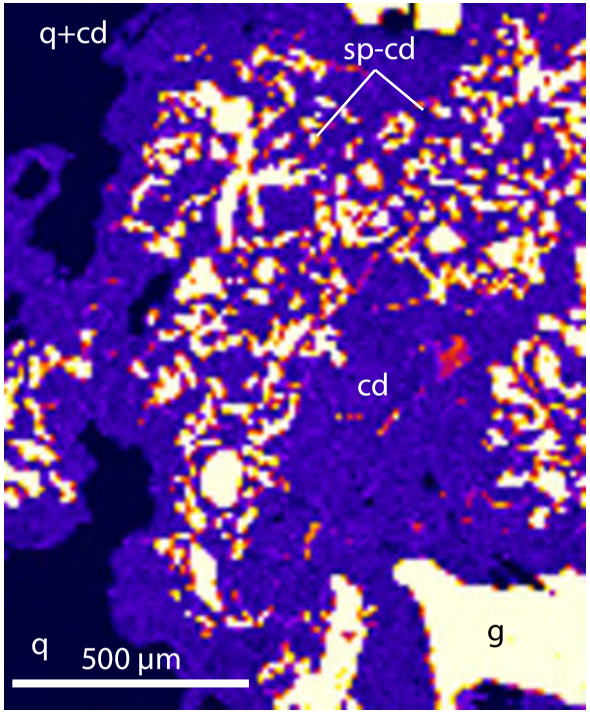

Si intensity map

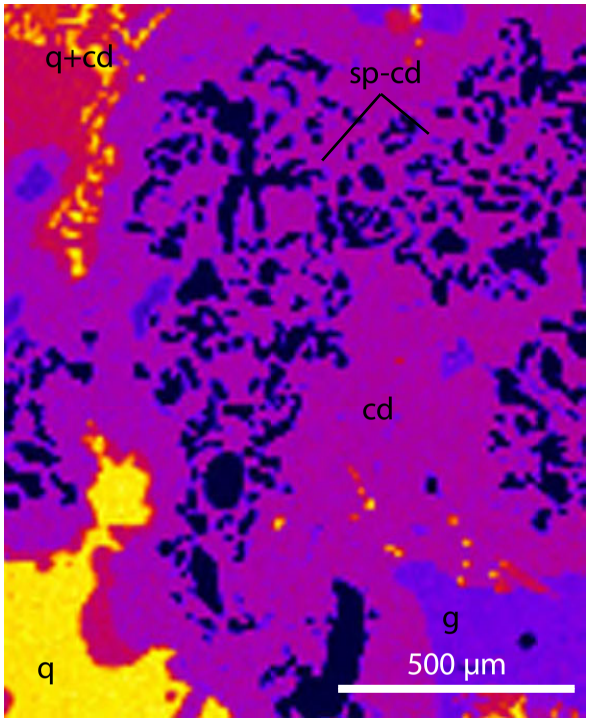

Left to right, photomicrograph viewed under cross polarized transmitted light, x-ray map of iron, x-ray map of silicon.

Figure 11

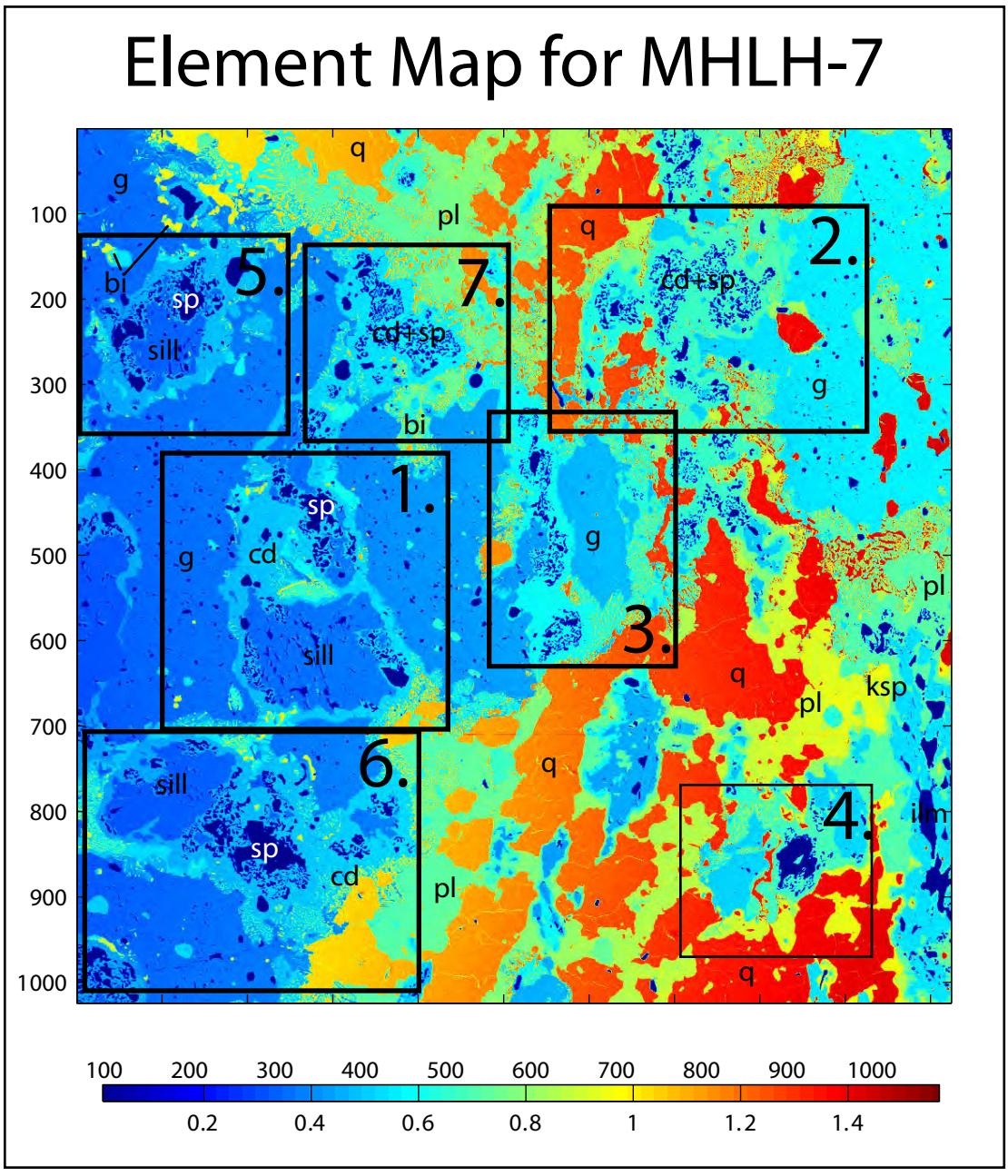
Element Map for MHLH-7
q
g
pl
q
2.
bi
sp
5.
7.
cd+sp
cd+sp
sill
g
bi
1.
sp
g
cd
g
3.
pl
sill
q
pl
ksp
6.
q
sill
4.
ilm
sp
cd
pl
q
100
200
300
400
500
600
700
800
900
1000
100 200 300 400 500 600 700 800 900 1000
0.2 0.4 0.6 0.8 1 1.2 1.4

Figure 12: Close-up of Square 5 sub-domain

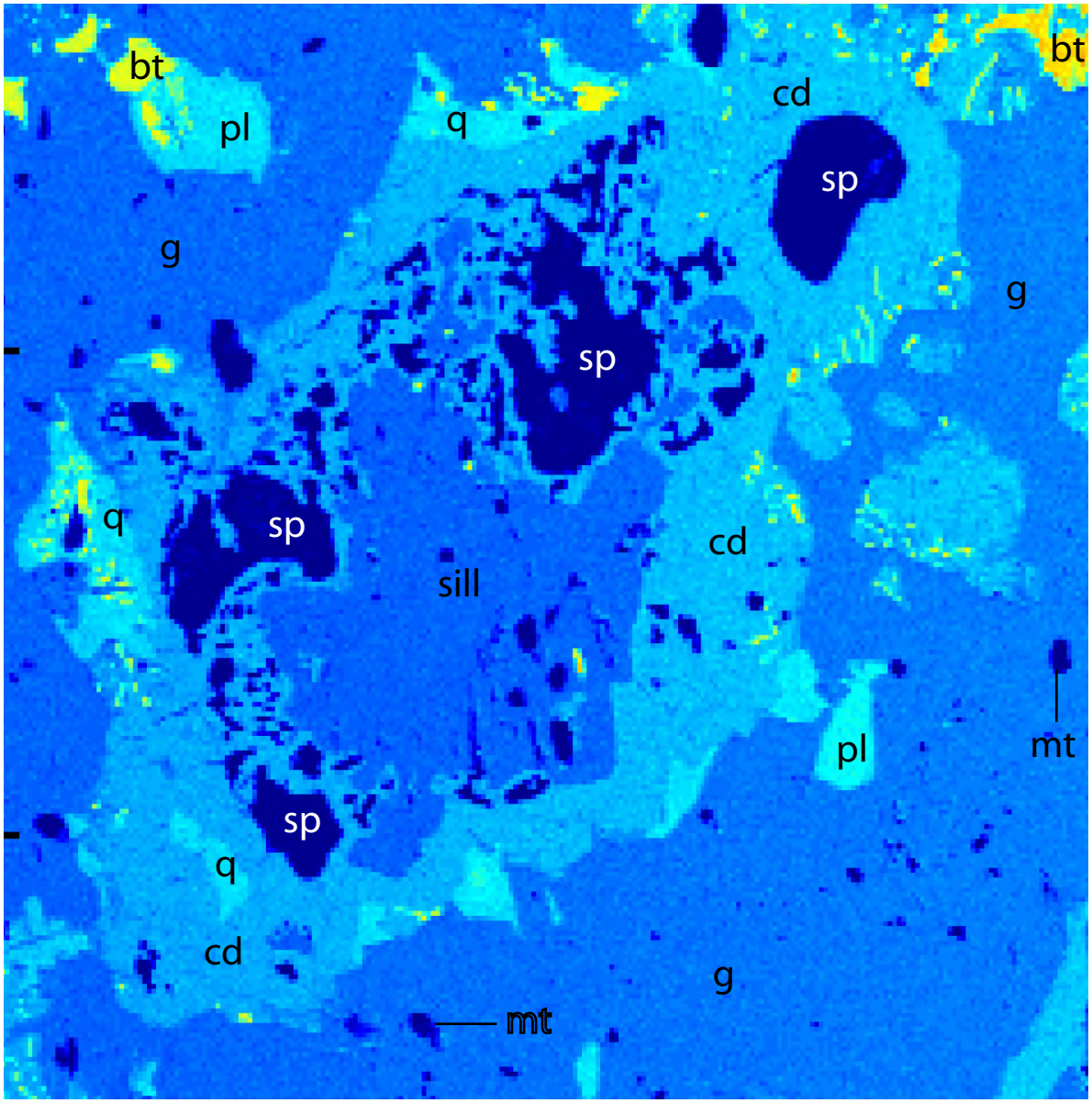

From MHLH-7, mineral composition and textures from the modelled Square 5, contained reaction texture.

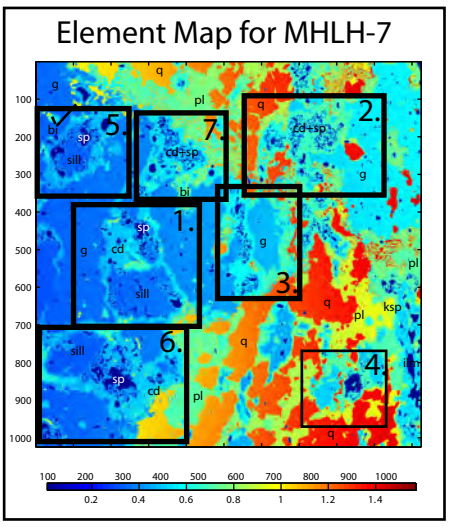

Figure 13

Temperature-Composition Diagram - Investigating the stability of sp-cd-sill-g assemblages with varying proportions of FeO-MgO at 4.4 kbar.

H2O	SiO2	Al2O3	CaO	MgO	FeO	K2O	Na2O	TiO2	O
5.14	60.11	16.48	0.41	12.18	1.06	2.55	0.84	0.70	0.53 (left)
5.14	60.11	16.48	0.41	0.00	13.24	2.55	0.84	0.70	0.53 (right)

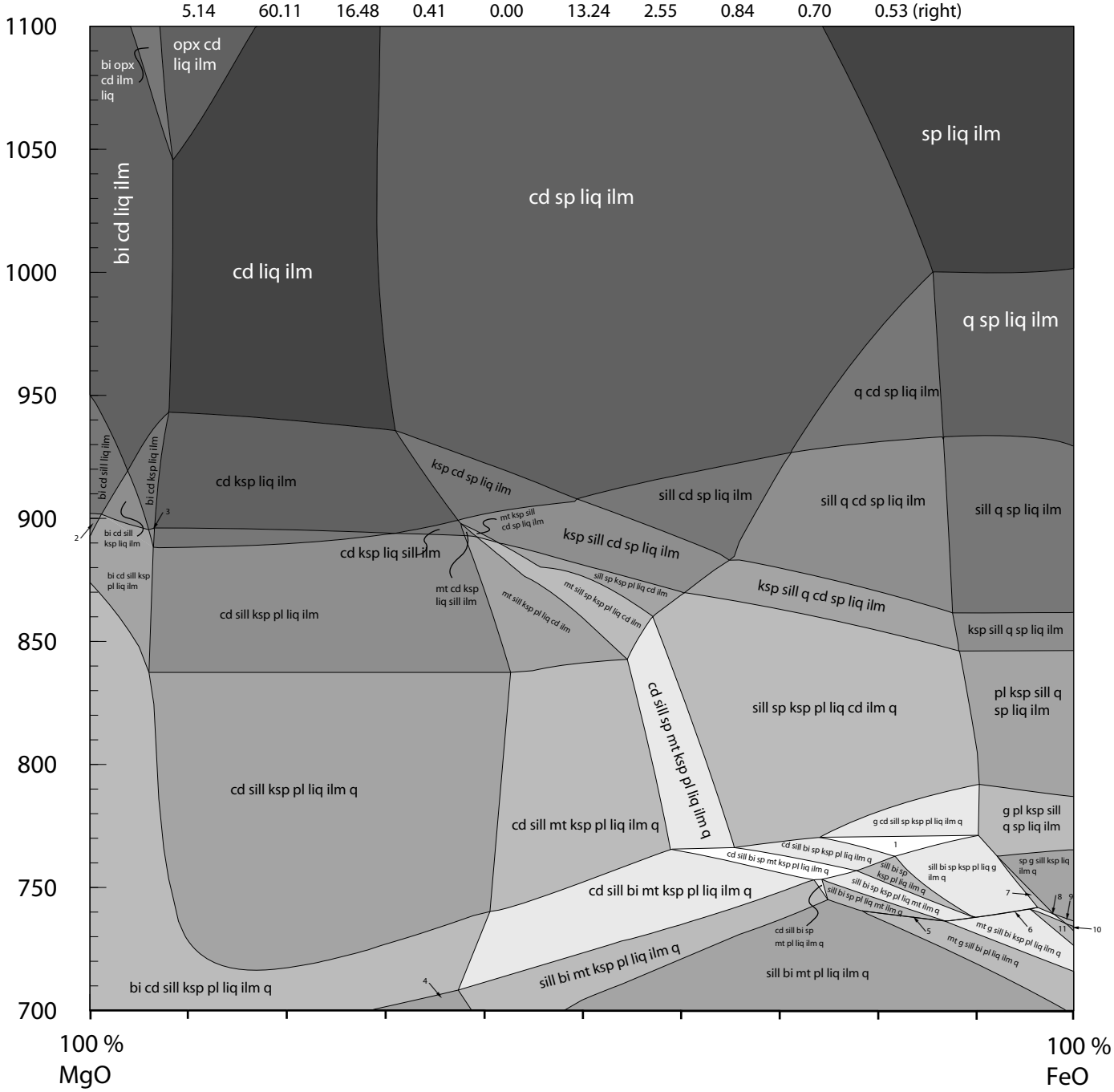

1. g cd sill bi sp ksp pl liq ilm q
2. ksp pl bi cd liq ilm
3. ksp pl bi cd liq ilm
4. sill bi ksp pl liq ilm q
5. mt g sill bi sp liq pl ilm q
6. ksp mt g sill bi sp liq pl ilm q
7. g sill bi sp ksp liq ilm q
8. g mt sp ksp bi sill liq ilm q
9. g mt sp ksp sill liq ilm q
10. g mt ksp sill liq ilm q
11. mt g sill bi ksp liq ilm q

Figure 14

Pressure-Temperature pseudosection for Fe-rich metapelites, in the system NCKFMASHTO (+q, +ilm).

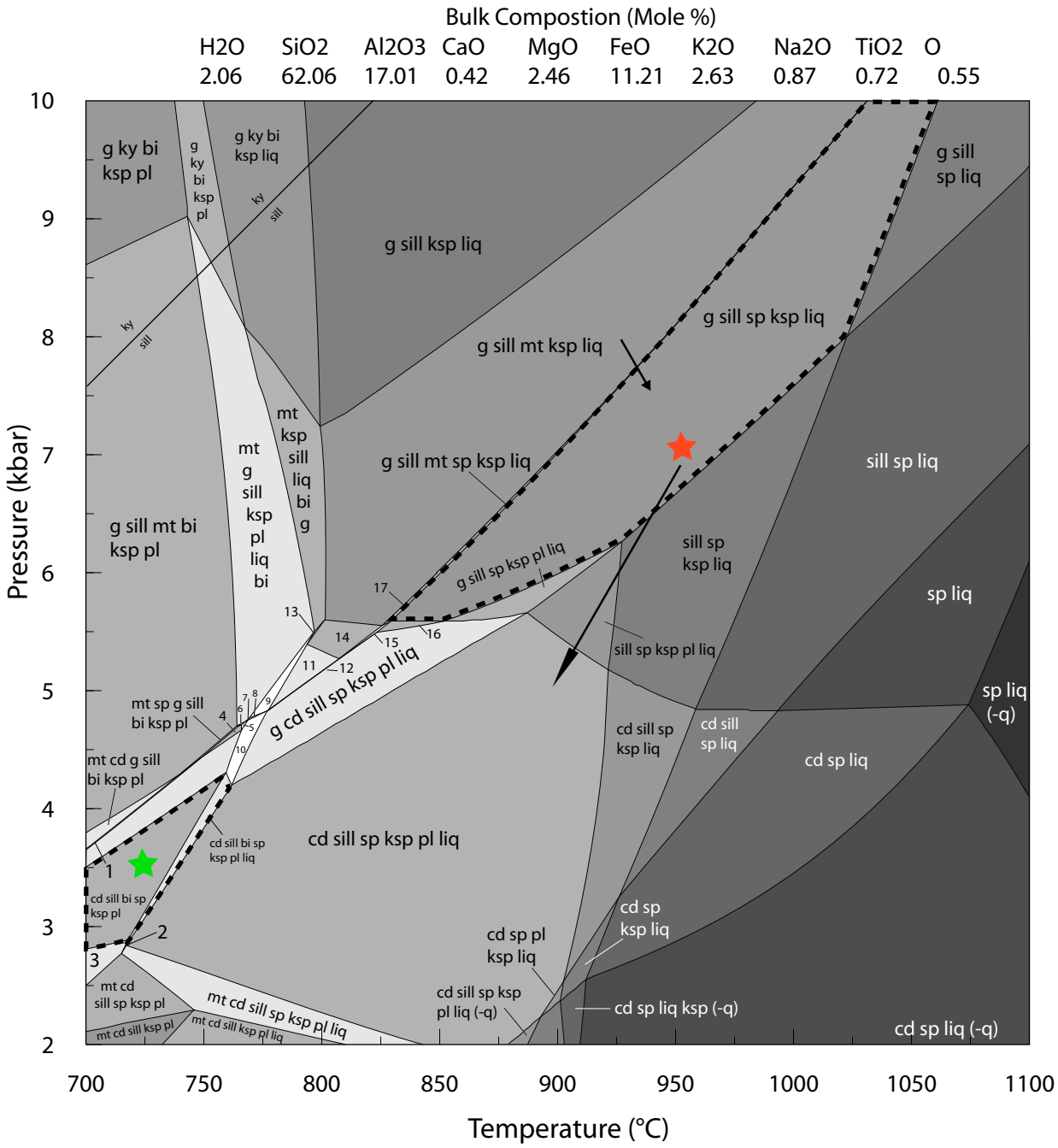

1. mt g cd sill bi sp ksp pl
2. mt cd sill bi sp ksp pl liq
3. mt cd sill bi sp ksp pl
4. g sill bi sp ksp pl
5. g sill bi sp ksp pl liq
6. mt g sill bi sp ksp pl liq
7. g sill bi ksp pl liq
8. g sill bi ksp pl liq cd
9. g cd sill bi mt ksp pl liq
10. g cd sill bi sp ksp pl liq
11. g cd sill sp ksp pl liq
12. g cd sill mt sp ksp pl liq
13. g cd sill mt bi ksp liq
14. g cd sill mt ksp liq
15. g cd sill mt sp ksp liq
16. g cd sill sp ksp liq
17. g sill mt sp ksp liq

Figure 15

Temperature - Composition phase diagram at 5 kbar in the system NCKFMASHTO.

Compositions (Mole %)

H2O	SiO2	Al2O3	CaO	MgO	FeO	K2O	Na2O	TiO2	O	
2.06	62.06	17.01	0.42	2.46	11.21	2.63	0.87	0.72	0.55	(Left-hand axis - fig. 14)
1.10	39.30	17.73	1.11	12.41	25.79	0.26	0.48	0.99	0.83	(right-hand axis - fig.16)

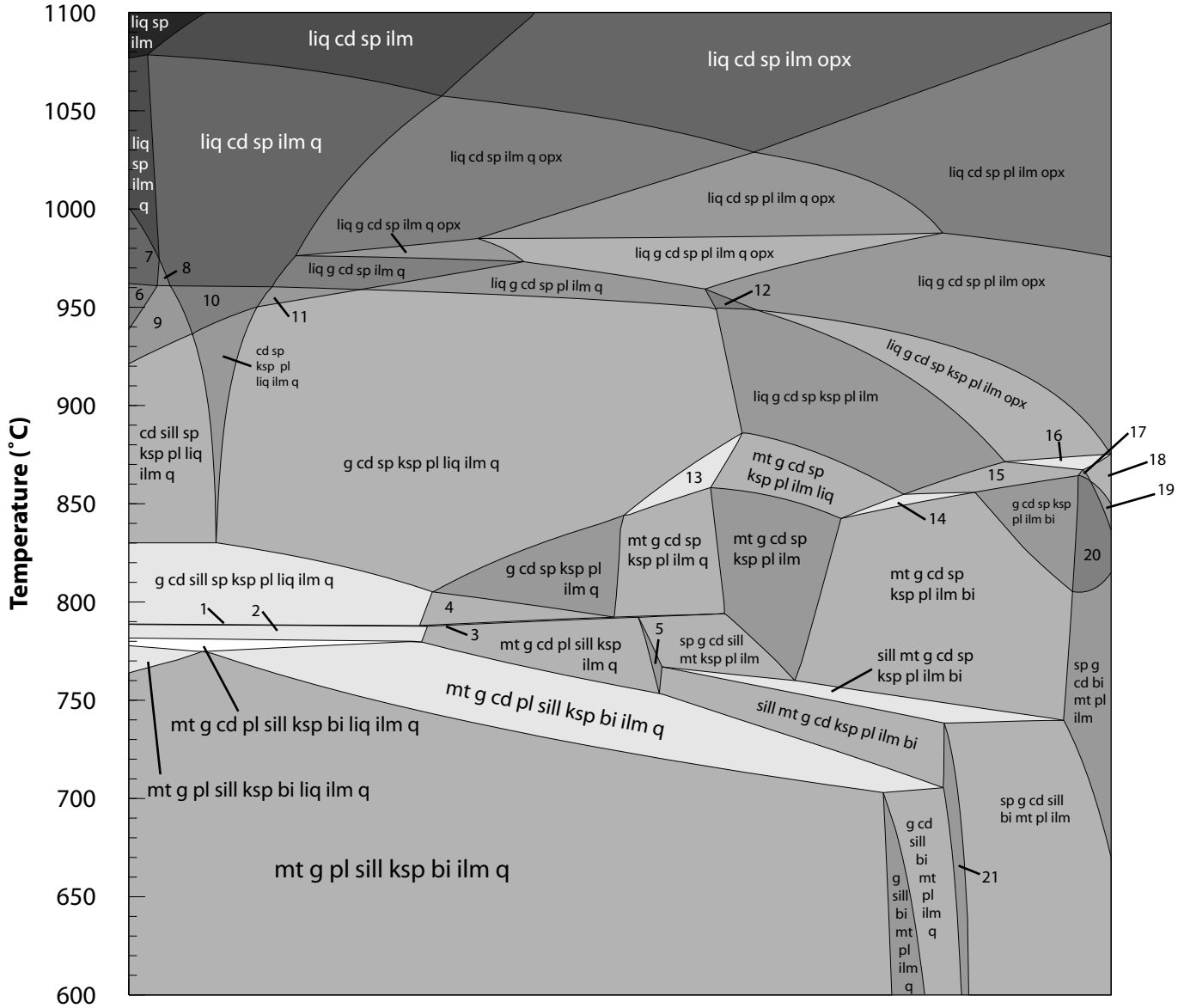

fig.14 fig.16

1. g cd sill sp mt ksp pl liq ilm q
2. g cd sill ksp pl liq mt ilm q
3. g cd sill mt ksp pl sp ilm q
4. g cd sill ksp pl sp ilm q
5. g cd sill mt ksp pl ilm
6. sill sp ksp liq ilm q
7. sill sp liq ilm q
8. cd sill sp liq ilm q
9. cd sill sp ksp liq ilm q
10. g cd sp ksp liq ilm q
11. cd sp ksp liq ilm q
12. liq g cd sp pl ilm
13. liq mt g cd sp ksp pl ilm q
14. liq bi mt g cd ksp pl ilm
15. g cd sp ksp pl bi ilm liq
16. g cd sp ksp pl bi ilm liq opx
17. g cd sp pl bi ilm liq
18. g cd sp pl bi ilm liq opx
19. g cd sp pl bi ilm opx
20. g cd sp pl bi ilm
21. g cd sill bi mt pl ilm

Figure 16

Pressure -Temperature phase diagram for a contained mineral reaction from MHLH-7 in the system NCKFMASHTO.

Composition (Mole %)

H2O	SiO2	Al2O3	CaO	MgO	FeO	K2O	Na2O	TiO2	O
1.10	39.30	17.73	1.11	12.41	25.79	0.26	0.48	0.99	0.83

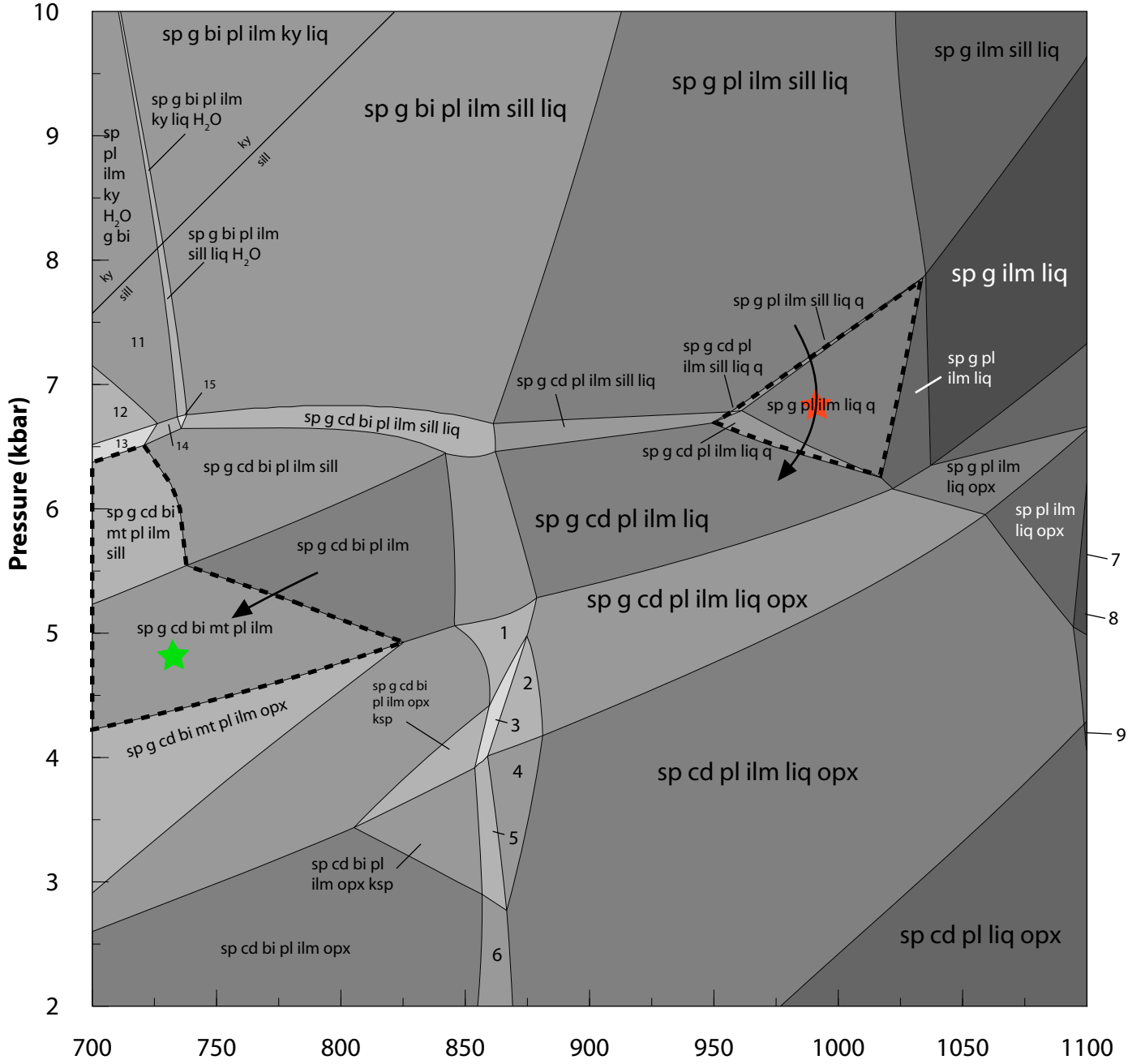

1. sp g cd bi pl ilm opx liq
2. sp g cd pl ilm opx ksp liq
3. sp g cd bi pl ilm opx ksp liq
4. sp cd pl ilm opx ksp liq
5. sp cd bi pl ilm opx ksp liq
6. sp cd bi pl ilm opx liq
7. sp ilm liq opx
8. sp ilm liq opx cd
9. sp liq opx cd
10. sp g ilm sill liq
11. sp H_2O g bi pl ilm sill
12. sp H_2O g bi pl ilm sill cd
13. mt sp H_2O g bi pl ilm sill cd
14. sp H_2O g bi pl ilm sill cd
15. sp H_2O liq g bi pl ilm sill cd

Figure 17

Geochronological Sample 187231: clinopyroxene-garnet-quartz-plagioclase-magentite bearing granulite.

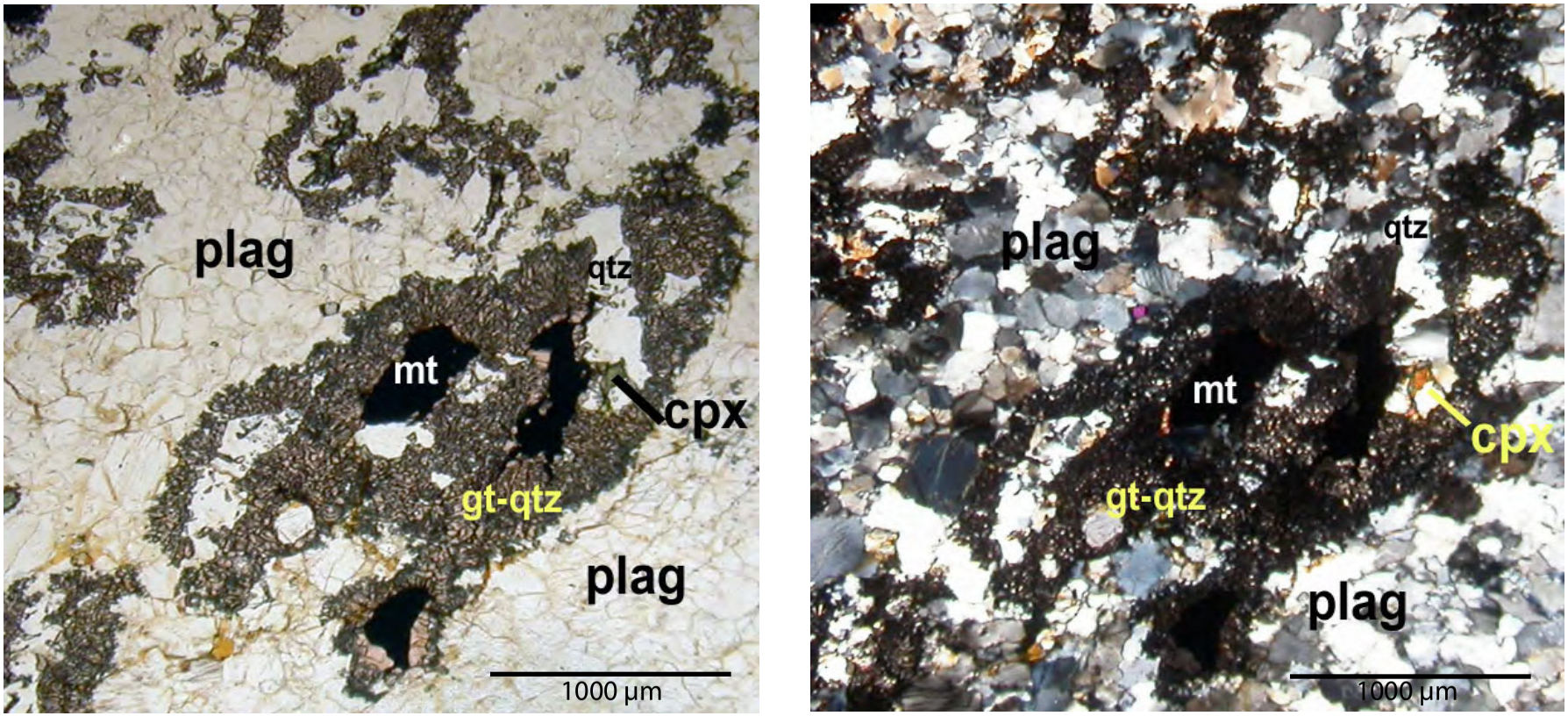

Figure 18

Zircon CL images: size, morphology and zonation.

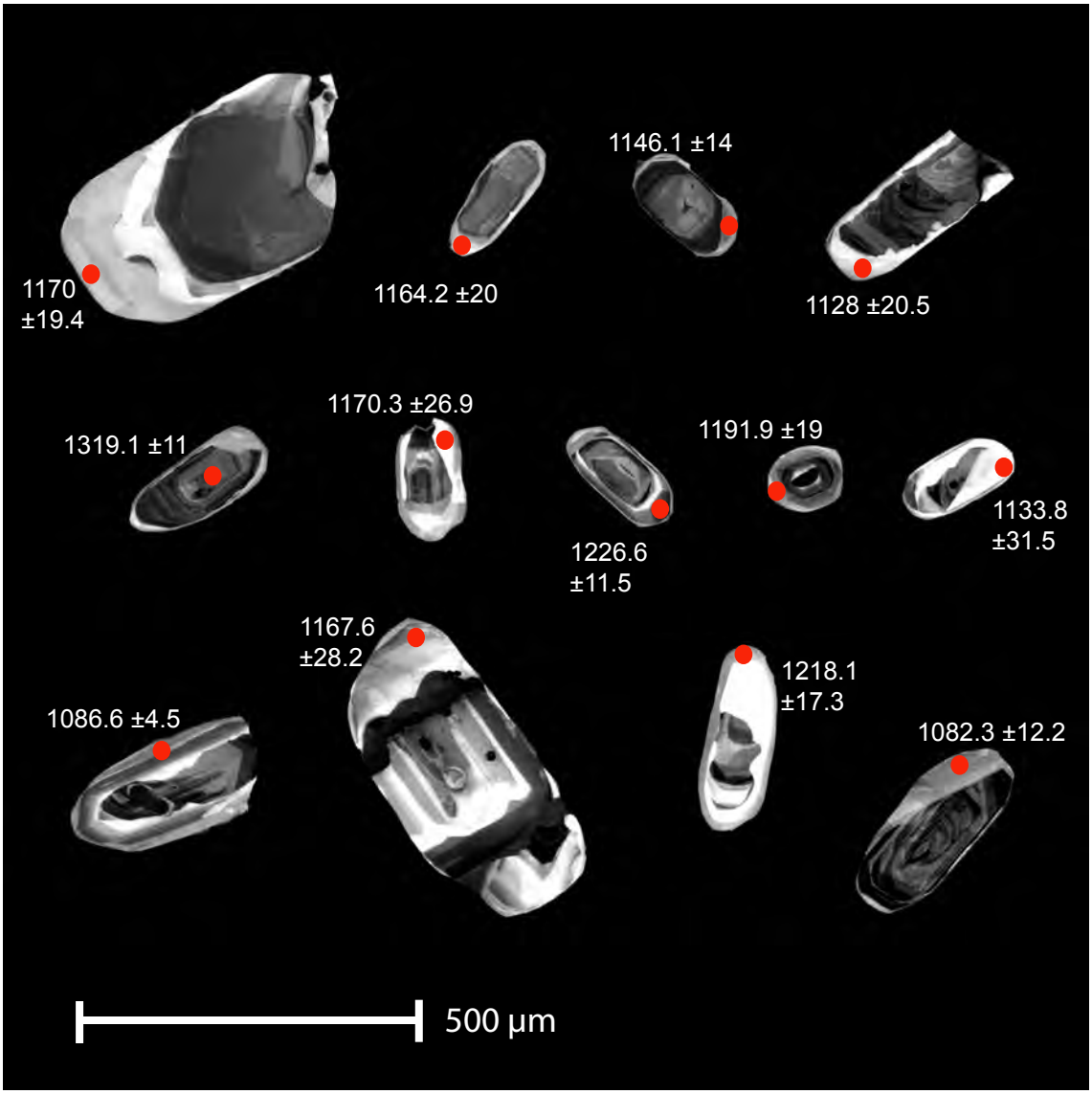

Figure 19

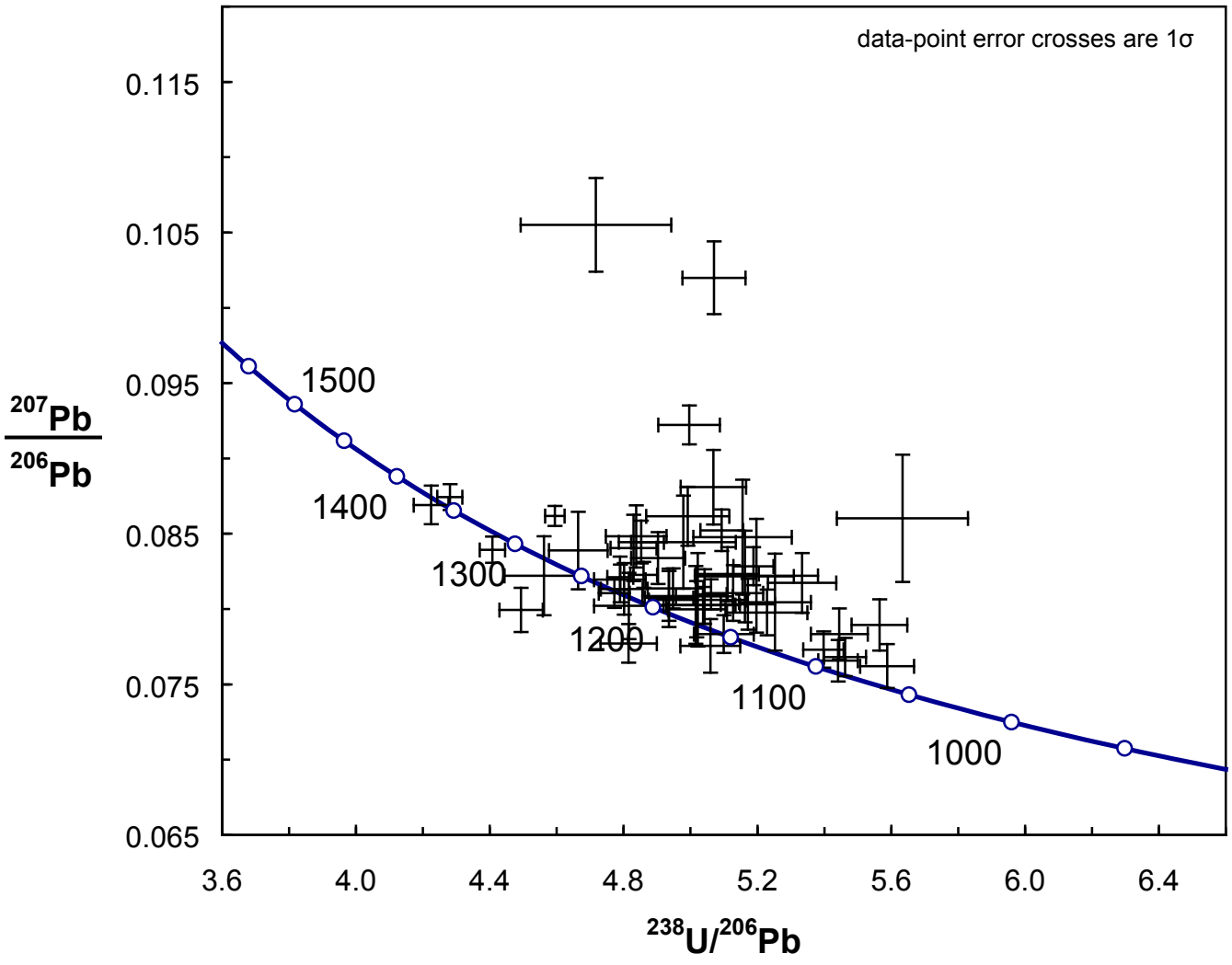

Figure 15: Terra-Wasserberg Plot of U-Pb data without 204 Pb correction for sample 187231.

Figure 20

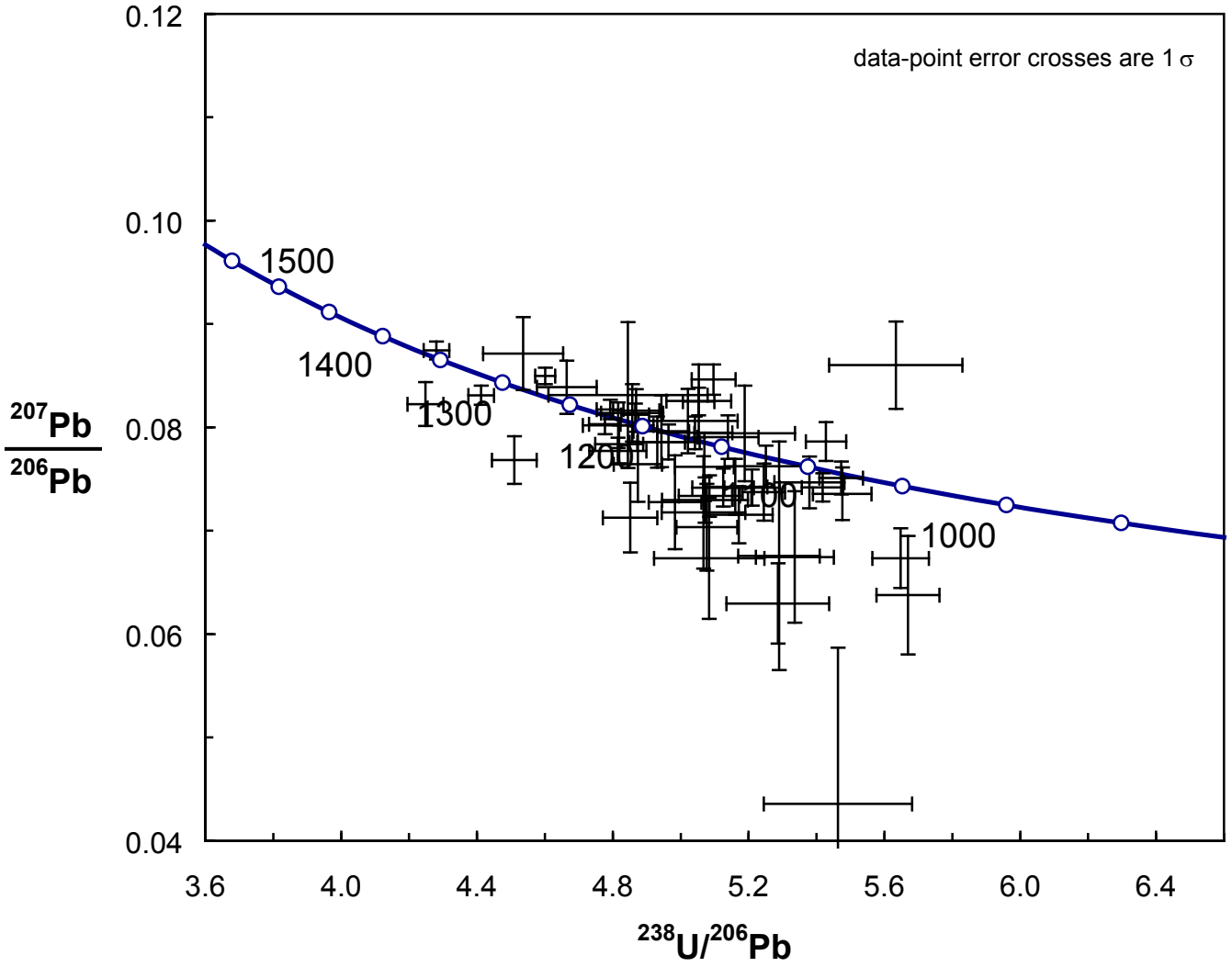

Figure 16: Terra-Wasserberg Plot of U-Pb data, with 204Pb correction, for sample 187231.

Figure 21

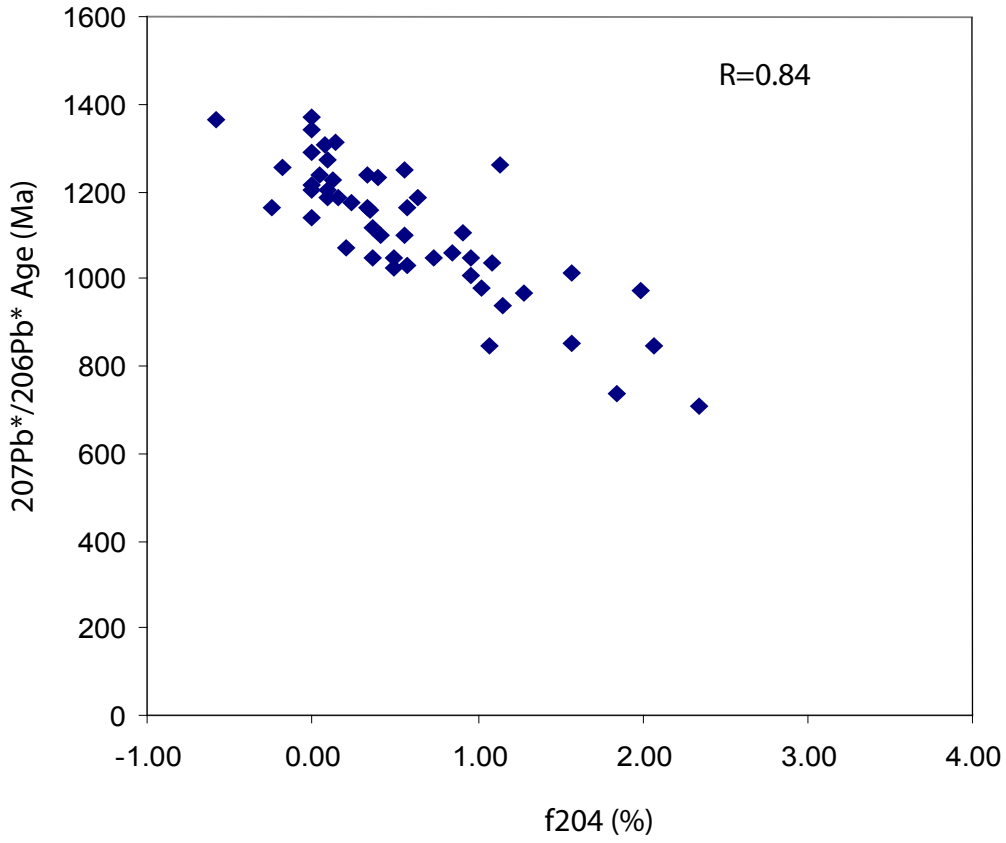
R=0.84
207Pb*/206Pb* Age (Ma)
1600
1400
1200
1000
800
600
400
200
0
-1.00
0.00
1.00
2.00
3.00
4.00
f204 (%)

Figure 22

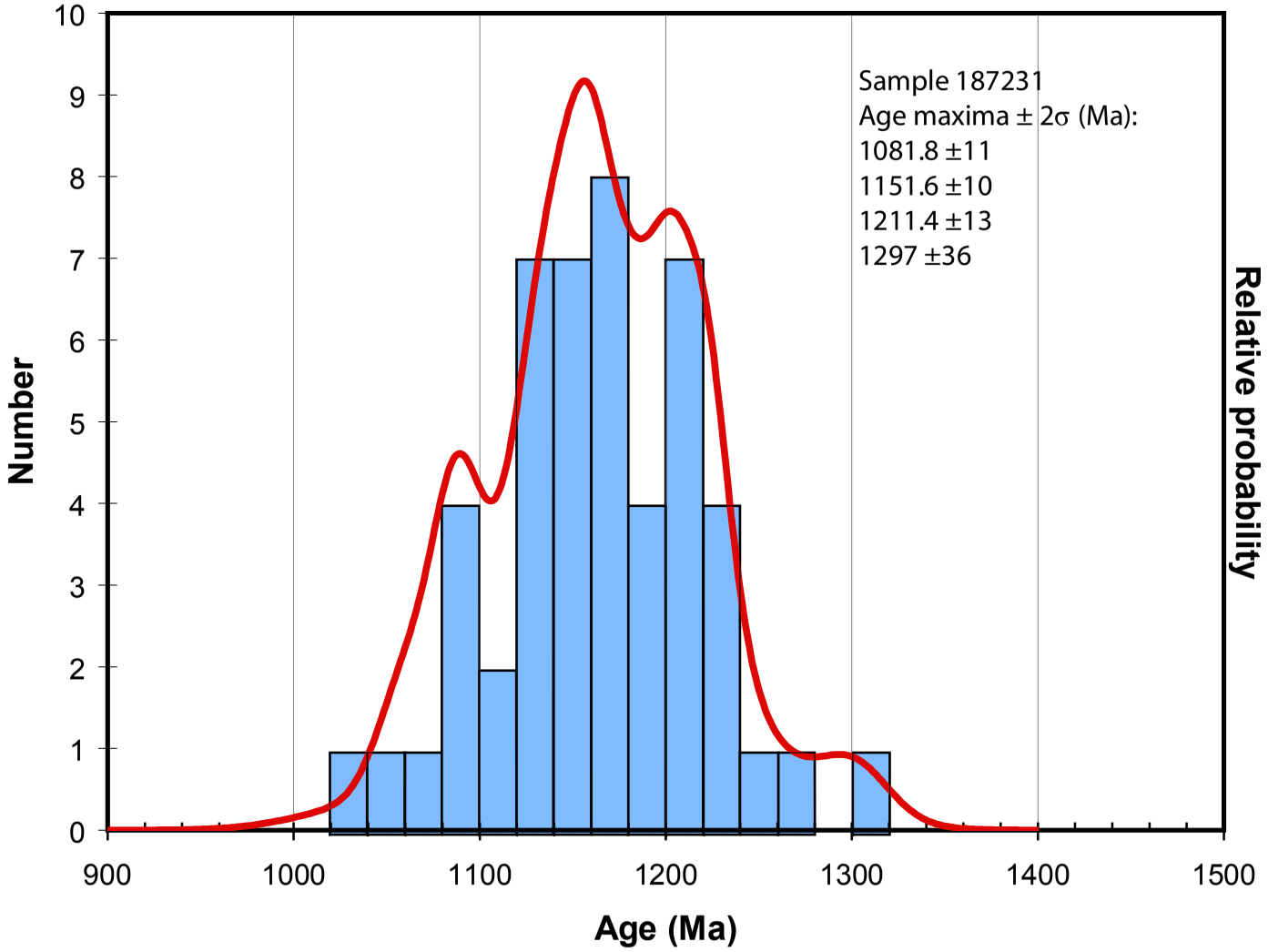
Sample 187231
Age maxima ± 2σ (Ma):
1081.8 ±11
1151.6 ±10
1211.4 ±13
1297 ±36
Number
Relative probability
Age (Ma)
0
1
2
3
4
5
6
7
8
9
10
900
1000
1100
1200
1300
1400
1500

Figure 23

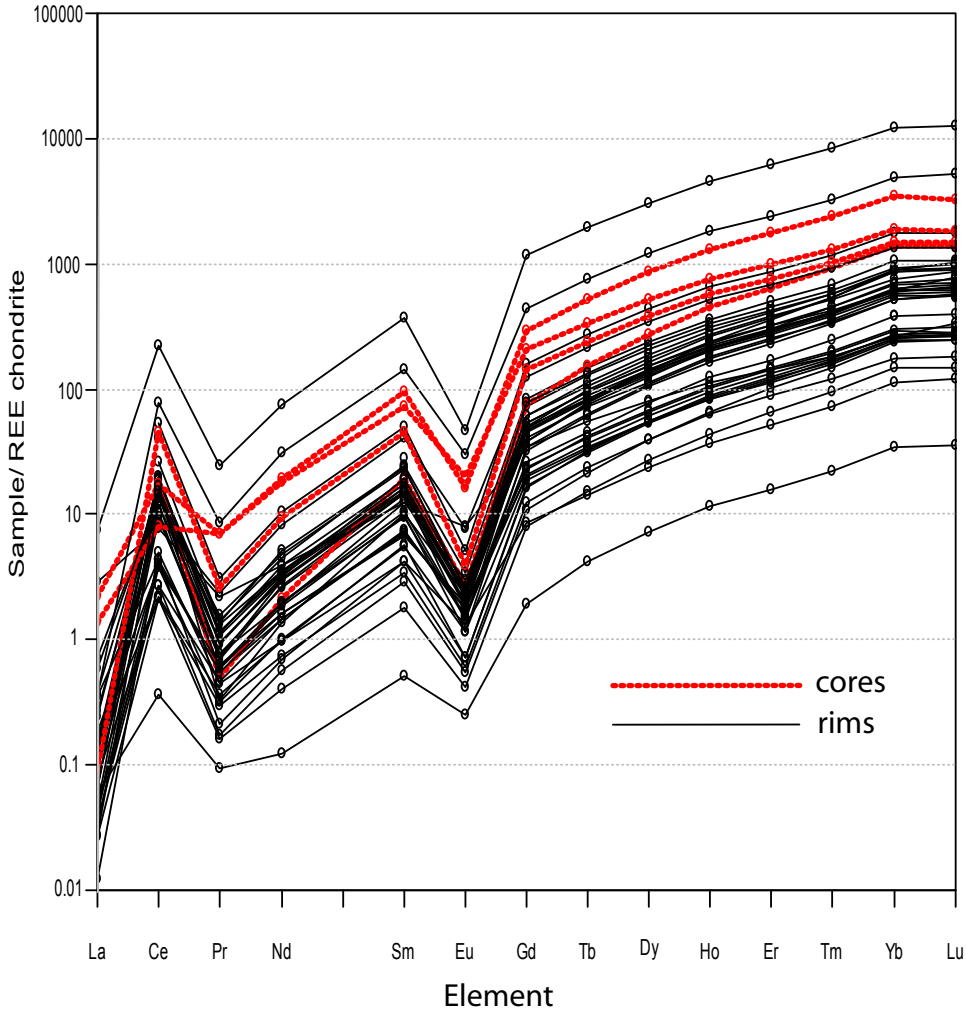

Chondrite normalised REE patterns of zircon cores and metamorphic overgrowths from clinopyroxene-quartz-garnet-plagioclase-bearing granulites from the Latitude Hills, W.A. Normalisation after Boynton (1984).

Figure 24

Titanium in zircon thermometry

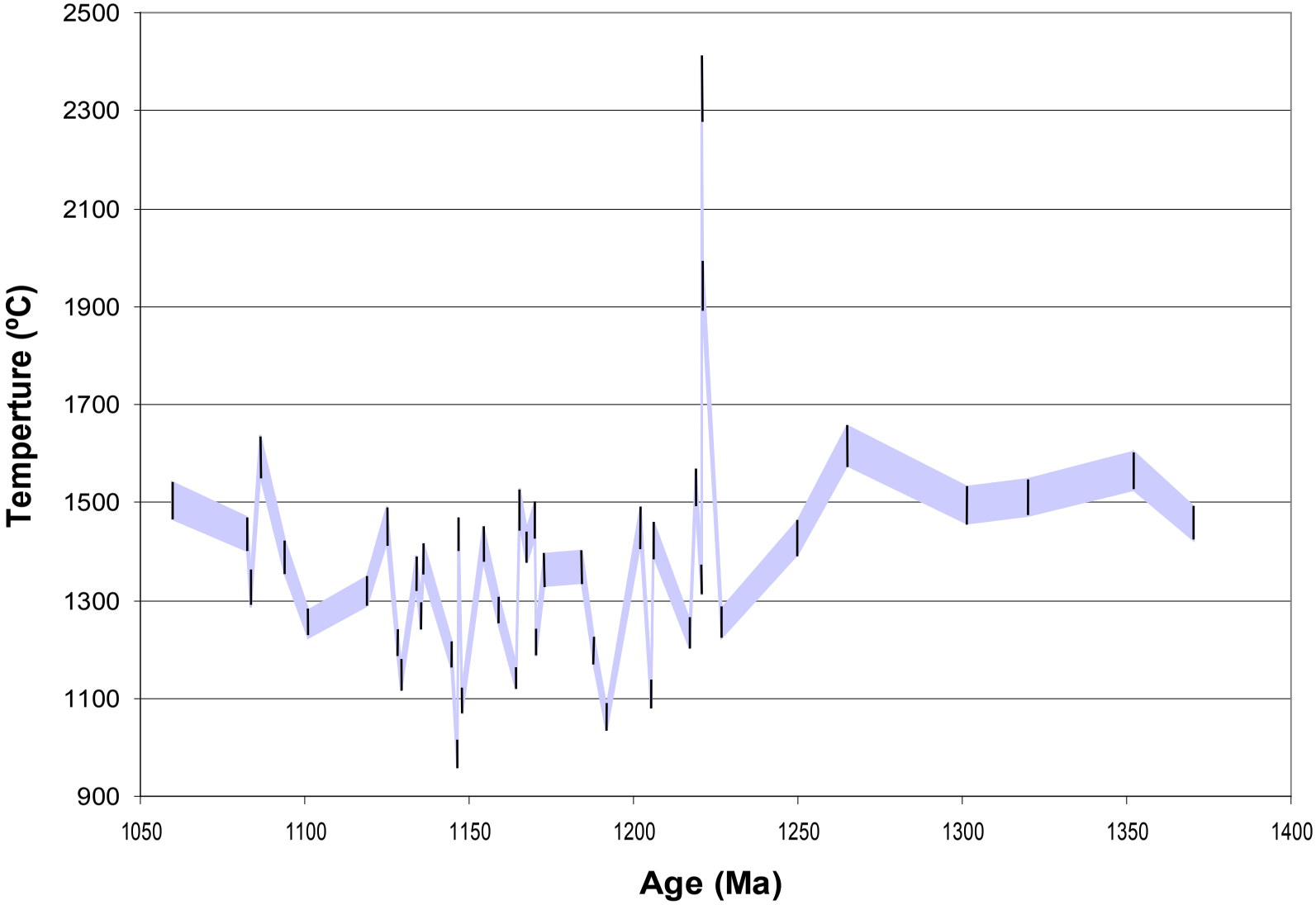

Table 1

Selected garnet and cordierite microprobe analyses.

	MHLH-6	MHLH-13	MHLH-16	MHLH-6	MHLH-13	MHLH-16
wt%	**gt**	**gt**	**gt**	**cd**	**cd**	**cd**
F	0.4217	0.3970	0.3175	0.1756	0.1632	0.1350
NaO	0.0114	0.0145	0.0084	0.0332	0.0262	0.0349
MgO	6.2406	6.8189	7.4051	8.6974	9.7696	10.6345
Al2O3	21.2647	21.5352	21.7114	32.7829	33.3827	33.3342
SiO2	37.9583	38.1375	38.0687	49.0723	48.9356	49.1567
Cl	0.0071	0.0097	0.0053	0.0133	0.0121	0.0109
K2O	0.0062	0.0114	0.0053	0.2632	0.0182	0.0366
CaO	0.8347	1.1790	0.9126	0.0268	0.0404	0.0544
TiO2	0.0214	0.0391	0.0328	0.0091	0.0189	0.0266
Cr2O3	0.0380	0.0561	0.0262	0.0137	0.0198	0.0111
MnO	0.5445	0.3649	0.5757	0.0343	0.0315	0.0370
FeO	32.9977	32.0958	31.4942	7.7312	6.4004	5.2299
ZnO	0.0659	0.0590	0.0519	0.0358	0.0562	0.0360
total	100.4121	100.7182	100.2977	98.8889	98.8747	98.7378
Recalculated cation data						
Si^{4+}	2.9949	2.9838	2.9683	5.0148	4.9654	4.9641
Ti^{4+}	0.0013	0.0023	0.0019	0.0007	0.0014	0.0020
Al^{3+}	1.9773	1.9856	1.9950	3.9482	3.9919	3.9671
Cr^{3+}	0.0024	0.0035	0.0016	0.0011	0.0016	0.0009
Fe^{3+}	0.0304	0.0421	0.0648	0.0606	0.0804	0.1114
Fe^{2+}	2.1466	2.0577	1.9886	0.6001	0.4626	0.3303
Mn^{2+}	0.0364	0.0242	0.0380	0.0030	0.0027	0.0032
Mg^{2+}	0.7340	0.7953	0.8608	1.3251	1.4778	1.6010
Zn^{2+}	0.0038	0.0034	0.0030	0.0027	0.0042	0.0027
Ca^{2+}	0.0706	0.0988	0.0762	0.0029	0.0044	0.0059
Na^{1+}	0.0017	0.0022	0.0013	0.0066	0.0052	0.0068
K^{1+}	0.0006	0.0011	0.0005	0.0343	0.0024	0.0047

Table 2

Selected plagioclase and K-feldspar microprobe analyses.

	MHLH-6	MHLH-13	MHLH-16	MHLH-6	MHLH-13	MHLH-16
wt%	**pl**	**pl**	**pl**	**ksp**	**ksp**	**ksp**
F	0.1239	0.0729	0.3514	0.1268	0.0659	0.1444
NaO	7.1462	6.0211	6.4554	1.3597	1.0264	1.8052
MgO	0.0037	0.0199	0.1330	0.0100	0.0149	0.0030
Al2O3	24.6990	27.6833	17.8900	18.8375	18.7287	18.6279
SiO2	60.1173	56.2330	61.4039	64.8181	64.2381	64.3450
Cl	0.0085	0.0045	0.0158	0.0082	0.0090	0.0030
K2O	0.1328	0.0855	5.9267	13.8192	14.7238	13.5773
CaO	6.3913	9.5648	2.9941	0.1685	0.0927	0.2921
TiO2	0.0285	0.0112	0.0766	0.0413	0.0360	0.0181
Cr2O3	0.0160	0.0148	0.0002	0.0103	0.0050	0.0002
MnO	0.0236	0.0102	0.0002	0.0153	0.0226	0.0013
FeO	0.2791	0.3644	5.8890	0.0786	0.1206	0.1492
ZnO	0.0638	0.0324	0.0002	0.0877	0.0316	0.0002
total	99.0336	100.1180	101.1365	99.3813	99.1152	98.8225
Recalculated cation data						
Si^{4+}	2.7218	2.5268	2.9824	3.0103	2.9912	2.9907
Ti^{4+}	0.0010	0.0004	0.0028	0.0014	0.0013	0.0006
Al^{3+}	1.3179	1.4660	1.0240	1.0310	1.0278	1.0204
Cr^{3+}	0.0006	0.0005	0.0000	0.0004	0.0002	0.0000
Fe^{3+}	-	0.0086	-	-	-	-
Fe^{2+}	0.0106	0.0051	0.2392	0.0031	0.0047	0.0058
Mn^{2+}	0.0009	0.0004	0.0000	0.0006	0.0009	0.0001
Mg^{2+}	0.0002	0.0013	0.0096	0.0007	0.0010	0.0002
Zn^{2+}	0.0021	0.0011	0.0000	0.0030	0.0011	0.0000
Ca^{2+}	0.3100	0.4604	0.1558	0.0084	0.0046	0.0145
Na^{1+}	0.6273	0.5245	0.2190	0.1224	0.0927	0.1627
K^{1+}	0.0077	0.0049	0.3672	0.8187	0.8746	0.8050

Table 3

Selected spinel and bi microprobe analyses.

	MHLH-6	MHLH-13	MHLH-16	MHLH-6	MHLH-13	MHLH-16
wt%	**sp**	**sp**	**sp**	**bi (absent)**	**bi**	**bi**
F	0.4214	0.3960	0.3579	-	2.1042	2.5626
NaO	0.0134	0.0166	0.0090	-	0.0557	0.0582
MgO	4.5582	5.7720	6.2670	-	16.9809	16.0846
Al2O3	56.7241	59.0787	58.2619	-	15.2837	16.7508
SiO2	0.0507	0.0949	0.1366	-	38.9365	37.4698
Cl	0.0043	0.0088	0.0107	-	0.1144	0.1563
K2O	0.0039	0.0046	0.0064	-	8.6713	8.8633
CaO	0.0104	0.0063	0.0045	-	0.0205	0.0303
TiO2	0.0362	0.0240	0.0205	-	3.8438	2.9947
Cr2O3	0.6294	0.3197	0.4785	-	0.2529	0.0603
MnO	0.0424	0.0492	0.0684	-	0.0224	0.0410
FeO	35.9892	33.4497	33.9364	-	11.9403	12.4076
ZnO	0.3485	0.4118	0.3885	-	0.4530	0.1483
total	98.8321	99.6323	99.5882	-	98.6795	95.0652
Recalculated cation data						
Si^{4+}	0.0015	0.0027	0.0038	-	2.5136	2.4516
Ti^{4+}	0.0008	0.0005	0.0004	-	0.1866	0.1474
Al^{3+}	1.9164	1.9529	1.9199	-	1.1628	1.2916
Cr^{3+}	0.0143	0.0071	0.0106	-	0.0129	0.0031
Fe^{3+}	0.0658	0.0348	0.0617	-	0.0513	-
Fe^{2+}	0.7969	0.7498	0.7318	-	0.5932	0.6788
Mn^{2+}	0.0010	0.0012	0.0016	-	0.0012	0.0023
Mg^{2+}	0.1948	0.2414	0.2612	-	1.6343	1.5689
Zn^{2+}	0.0074	0.0085	0.0080	-	0.0216	0.0072
Ca^{2+}	0.0003	0.0002	0.0001	-	0.0014	0.0021
Na^{1+}	0.0007	0.0009	0.0005	-	0.0070	0.0074
K^{1+}	0.0001	0.0002	0.0002	-	0.7141	0.7397

Table 4

Mineral Chemistry Summary			
Sample	**MHLH-06**	**MHLH-13**	**MHLH-16**
Description	Metapelite	Metapelite	Metapelite
Peak assemblage	sill-g-q-sp-mt-ksp	sill-q-sp-g-ilm	g-q-sp-ksp-pl-ilm
Post-peak assembla	cd-sp-sill-pl-ksp-mt	sp-cd-ksp-pl-bi	sp-cd-g-ksp-pl-mt-ilm-bt
XCa (cpx)	-	-	-
XFe (opx)	-	-	-
XFe (sp)	0.86-0.90	0.82-0.85	0.81-0.87
XFe (ilm)	0.479-0.481	0.468-0.470	0.472-0.473
XFe (cd)	0.47-0.48	0.39-0.41	0.33-0.40
TiO2 wt% (bi)	-	2.80-4.53	2.85-4.92
F ox% (bi)	-	1.69-2.46	1.73-3.87
Cl ox% (bi)	-	0.06-0.18	0.05-0.29
F ox% (g)	0.30-0.53	0.19-0.60	0.01-0.58
%Almandine (g)	78.13-85.17	77.12-83.31	81.88-76.14
%Pyrope (g)	11.64-18.30	14.16-18.66	14.80-19.93
%Grossular (g)	2.00-2.15	1.92-3.05	2.12-2.18
%Spessartine (g)	1.03-1.56	0.60-1.16	1.20-1.75
XCa (ksp)	0.001-0.02	0.0001-0.01	0.017-0.02
XNa (ksp)	0.06-0.10	0.5-0.1	0.07-0.21
XK (ksp)	0.87-0.94	0.89-0.95	0.76-0.90
XCa (pl)	0.45-0.46	0.60-0.62	0.26
XNa (pl)	0.52-0.54	0.37-0.39	0.21
XK (pl)	0.006-0.014	0.004-0.007	0.53
sill	Y	Y	Y
q	Y	Y	Y

Mineral chemistry summary of Latitude Hills metapelites. P.A. = peak assemblage, R.M.= retrograde mineral products, Y shows presence of mineral, (-) indicates absence.

Table 5: X-ray element map, bulk compositions for selected squares

Analysis No.	H_2O	SiO_2	Al_2O_3	CaO	MgO	FeO	K_2O	Na_2O	TiO_2	O
LH7-box1	1.86	42.07	19.75	1.03	10.75	22.86	0.23	0.44	0.58	0.42
LH7-box2	3.43	56.99	11.13	0.93	8.85	16.96	0.30	0.51	0.31	0.58
LH7-box3	3.44	53.31	13.48	0.57	10.91	16.73	0.37	0.23	0.17	0.78
LH7-box4	1.75	67.82	11.48	0.41	5.14	10.30	1.62	0.58	0.12	0.79
LH7-box5	1.10	39.30	17.73	1.11	12.41	25.79	0.26	0.48	0.99	0.83
LH7-box6	2.14	48.48	16.68	0.96	10.03	18.69	0.77	0.64	0.60	1.01
LH7-box7	3.81	50.96	14.70	1.63	10.09	15.49	0.53	1.26	0.75	0.78

Table 6: Bulk compositions for calculated T-X diagrams and pseudosections.

	H_2O	SiO_2	Al_2O_3	CaO	MgO	FeO	K_2O	NaO	TiO_2	O	
Figure 13	5.14 5.14	60.11 60.11	16.48 16.48	0.41 0.41	12.18 0.00	1.06 13.24	2.55 2.55	0.84 0.84	0.70 0.70	0.53 0.53	(LH axis) (RH axis)
Figure 14	2.06	62.06	17.01	0.42	2.46	11.21	2.63	0.87	0.72	0.55	
Figure 15	2.06 1.11	62.06 39.30	17.01 17.73	0.42 1.11	2.46 12.41	11.21 25.79	2.63 0.26	0.87 0.48	0.72 0.99	0.55 0.83	(LH axis) (RH axis)
Figure 16	1.11	39.30	17.73	1.11	12.41	25.79	0.26	0.48	0.99	0.83	

Table 7: Geochronology

Sample	U ppm	Th ppm	Th/U	% comm 206	% Concordant	204corr 206Pb/238U Age	±	204 corr 207Pb/206Pb Age	±	207corr 206Pb/238U Age	±	Total 238/206	% err	Total 207 /206	% err	238/ 206r	% err	207r /206r	% err
Metamorphic rim analyses																			
231-1.1	27.45	72.84	2.74	1.16	-19	1159	19	938	122	1170	19	5.02	1.7	.0800	2.3	5.08	1.8	.0703	6.0
231-2.1	22.84	85.82	3.88	4.15	-23	1116	23	856	340	1128	21	5.07	1.9	.1020	2.4	5.29	2.3	.0676	16.3
231-3.1	46.96	138.24	3.04	1.14	8	1164	20	1259	84	1159	21	5.00	1.8	.0922	1.4	5.05	1.9	.0826	4.3
231-4.1	99.27	505.44	5.26	0.09	-2	1227	12	1205	25	1228	13	4.77	1.0	.0810	1.2	4.78	1.0	.0803	1.2
231-5.1	36.15	73.81	2.11	0.73	-8	1136	18	1045	88	1141	19	5.17	1.6	.0803	2.1	5.21	1.6	.0742	2.4
231-6.1	12.80	50.83	4.10	2.64	5	1156	35	1272	196	1150	35	4.72	4.8	.1055	2.9	4.84	4.8	.0831	8.5
231-7.1	55.36	135.10	2.52	0.33	-2	1201	16	1161	43	1203	17	4.95	1.8	.0814	1.6	4.96	1.8	.0786	2.2
231-8.1	78.95	69.06	0.90	0.33	3	1236	16	1238	50	1236	17	4.85	1.4	.0844	1.7	4.87	1.4	.0816	2.5
231-9.1	61.05	141.37	2.39	0.07	13	1165	15	1308	33	1157	16	5.09	1.3	.0852	1.6	5.10	1.3	.0846	1.7
231-10.1	42.20	24.41	0.60	1.84	-30	1043	17	736	187	1056	17	5.56	1.5	.0789	2.2	5.67	1.6	.0638	9.0
231-11.1	39.82	118.46	3.07	1.28	-20	1262	19	964	95	1278	20	4.79	1.6	.0820	1.8	4.85	1.6	.0713	4.7
231-12.1	33.07	90.29	2.82	0.57	-2	1189	20	1161	66	1191	21	4.90	1.6	.0834	2.1	4.93	1.7	.0786	3.1
231-13.1	48.70	44.02	0.93	0.00	-6	1209	15	1140	33	1213	16	4.81	1.7	.0777	1.7	4.81	1.7	.0777	1.7
231-14.1	13.61	54.80	4.16	-0.58	6	1293	33	1365	78	1288	35	4.56	2.6	.0822	3.2	4.54	2.6	.0871	4.0
231-15.1	27.01	47.26	1.81	0.84	-4	1115	22	1060	101	1118	23	5.33	1.9	.0817	2.4	5.38	1.9	.0747	3.3
231-16.1	31.40	43.42	1.43	0.50	-12	1171	21	1024	72	1178	22	5.06	1.8	.0776	2.3	5.08	1.8	.0734	2.7
231-17.1	39.61	74.82	1.95	0.37	-13	1279	18	1118	60	1289	20	4.49	1.4	.0799	1.8	4.51	1.5	.0768	3.0
231-18.1	32.83	78.72	2.48	0.57	-5	1082	17	1030	75	1084	18	5.44	1.6	.0783	2.2	5.48	1.6	.0736	3.5
231-19.1	45.70	49.64	1.12	1.07	-19	1049	16	849	99	1057	16	5.59	1.4	.0762	1.9	5.65	1.5	.0674	4.3
231-20.1	62.43	50.06	0.83	0.09	2	1174	14	1174	40	1174	15	5.04	2.2	.0802	1.5	5.04	2.2	.0795	2.0
231-21.1	28.36	71.81	2.62	0.24	2	1160	20	1173	52	1159	22	5.13	1.7	.0811	2.3	5.14	1.7	.0791	2.7
231-22.1	10.83	52.12	4.97	0.63	4	1152	33	1183	115	1151	35	5.16	2.8	.0848	4.5	5.19	2.9	.0794	5.8
231-23.1	55.49	51.42	0.96	0.50	-9	1147	14	1046	55	1152	15	5.10	1.8	.0783	1.6	5.12	1.8	.0742	2.5
231-24.1	62.79	44.20	0.73	1.09	-8	1131	13	1034	74	1135	14	5.19	1.2	.0828	1.5	5.24	1.2	.0737	3.7
231-25.1	75.12	36.93	0.51	0.20	-1	1091	13	1072	42	1092	13	5.46	1.2	.0768	1.7	5.47	1.2	.0751	2.1
231-26.1	10.56	41.47	4.06	0.00	4	1178	34	1212	76	1176	36	5.02	2.9	.0806	3.9	5.02	2.9	.0806	3.9
231-27.1	28.51	119.88	4.34	0.00	3	1214	21	1291	59	1210	22	4.66	1.9	.0839	3.1	4.66	1.9	.0839	3.1
231-28.1	24.25	61.18	2.61	1.57	-23	1098	23	852	194	1109	24	5.25	2.0	.0805	4.0	5.34	2.2	.0675	9.4
231-29.1	73.68	100.47	1.41	0.37	-4	1096	12	1046	46	1098	13	5.40	1.1	.0773	1.6	5.42	1.1	.0742	1.9
231-30.1	24.86	26.96	1.12	1.98	-15	1140	23	974	176	1149	24	5.07	1.9	.0881	2.8	5.17	1.9	.0715	3.9
231-31.1	44.58	54.02	1.25	0.90	-8	1201	17	1107	94	1206	18	4.83	1.4	.0841	2.6	4.87	1.5	.0764	4.8
231-32.1	7.45	31.59	4.38	4.88	-112	1120	43	-128	838	1163	44	5.20	3.5	.0822	4.6	5.46	4.0	.0436	34.6
231-33.1	32.33	40.56	1.30	0.55	-5	1147	20	1099	87	1150	21	5.04	1.7	.0808	2.2	5.07	1.7	.0762	4.3
231-34.1	100.01	108.89	1.13	-0.18	8	1143	10	1258	32	1137	11	5.06	0.9	.0810	1.2	5.05	0.9	.0825	1.6
231-35.1	15.02	35.49	2.44	1.02	-16	1151	28	980	153	1159	29	5.02	2.4	.0803	3.2	5.07	2.4	.0718	7.6
231-36.1	43.67	112.61	2.66	0.42	-2	1149	17	1102	55	1151	18	5.23	2.3	.0798	1.9	5.25	2.3	.0763	2.6
231-37.1	38.76	130.32	3.47	0.95	-15	1183	18	1007	126	1192	19	4.94	1.5	.0807	2.4	4.98	1.6	.0728	6.2
231-38.1	31.42	85.23	2.80	0.96	-8	1116	19	1049	97	1119	20	5.11	1.8	.0823	2.2	5.16	1.8	.0743	3.7
231-39.1	10.37	49.91	4.98	2.06	-27	1109	33	849	241	1120	34	4.98	3.1	.0844	3.7	5.08	3.2	.0673	8.7
231-39.2	9.61	22.75	2.45	0.00	27	986	34	1339	95	971	36	5.63	3.5	.0860	4.9	5.63	3.5	.0860	4.9
231-40.1	26.32	107.65	4.23	1.58	-13	1151	21	1013	136	1157	22	4.99	2.5	.0862	2.3	5.07	2.5	.0730	3.0
231-41.1	26.27	54.76	2.15	0.40	2	1196	22	1230	67	1194	24	4.84	1.9	.0848	2.4	4.86	1.9	.0814	3.4
231-42.1	67.23	142.26	2.19	-0.24	7	1101	12	1163	47	1098	13	5.44	1.1	.0766	1.8	5.43	1.1	.0786	2.4
231-43.1	37.09	50.26	1.40	0.35	-5	1220	18	1156	55	1224	19	4.80	1.5	.0813	2.1	4.82	1.5	.0784	2.3
231-44.1	24.98	82.23	3.40	0.00	-1	1124	23	1202	54	1120	25	4.82	2.2	.0802	2.7	4.82	2.2	.0802	2.7
231-45.1	10.53	45.70	4.48	2.33	-37	1110	33	707	272	1127	34	5.16	2.8	.0822	3.7	5.29	2.9	.0630	6.2
231-46.1	36.82	61.48	1.73	0.15	0	1196	20	1188	86	1197	21	4.94	1.6	.0809	2.0	4.94	1.7	.0796	4.4
231-34.2	130.97	136.66	1.08	0.13	2	1204	10	1227	27	1202	10	4.86	0.8	.0823	1.0	4.87	0.8	.0812	1.4
Core analyses																			
231-47.1	120.01	131.98	1.14	0.10	-3	1320	11	1272	22	1323	12	4.41	0.9	.0839	1.0	4.41	0.9	.0831	1.1
231-29.2	133.17	127.99	0.99	0.00	1	1362	12	1371	19	1362	13	4.28	0.9	.0874	1.0	4.28	0.9	.0874	1.0
231-48.1	132.82	628.55	4.89	0.04	1	1216	10	1239	23	1214	10	4.79	0.8	.0821	1.0	4.79	0.8	.0817	1.2
231-49.1	215.28	153.90	0.74	0.14	4	1262	8	1315	18	1259	8	4.59	0.6	.0862	0.8	4.60	0.6	.0850	0.9
231-50.1	55.08	69.46	1.30	0.55	-8	1367	17	1251	50	1375	18	4.22	1.2	.0869	1.5	4.25	1.2	.0822	2.6

	Element												
	Ca	Sc	Ti	Ga	Y	Zr	Nb	Cs	Ba	La	Ce	Pr	Nd
Zircon rims													
231_1_1	<67.87	314.21	1417.94	0.032	698.31	416451.25	8.08	<0.0106	0.045	<0.040	21.52	0.174	2.7
231_2_1	<66.13	236.53	1089.4	0.044	594.58	321712.56	3.41	<0.0091	0.078	0.0837	10.92	0.191	2.86
231_3_1	<39.61	141.85	651.7	0.049	339.27	247059.23	4.98	<0.0074	0.104	0.0287	9.58	0.0722	1.123
231_4_1	<124.96	429.61	1962.29	0.059	1296.69	755720.88	14.95	<0.017	0.145	<0.015	42.7	0.372	6.34
231_5_1	<51.24	193.87	897.27	0.098	398.57	336390.25	5.12	<0.0069	0.542	0.22	11.23	0.161	2.15
231_6_1	<39.56	103.18	477.46	0.0587	185	150658.81	0.828	<0.0046	0.193	0.0293	3.31	0.0658	0.883
231_7_1	1403.79	122.7	657.62	0.851	369.87	187007.84	3.73	<0.0050	1.99	44.99	117.87	15.47	77.85
231_8_1	<64.75	244.81	1174.2	0.046	514.14	378651.16	5.51	<0.0077	0.148	0.042	12.09	0.084	1.62
231_9_1	<25.38	85.2	395.01	0.0632	249.5	118849.08	11.76	<0.0032	0.251	0.902	6.16	0.264	2.35
231_11_1	20.97	55.11	261.2	0.008	130.12	78270.13	1.157	0.0025	0.0215	0.0143	2.195	0.0208	0.34
231_12_1	<48.62	168.67	792.33	0.029	403.92	300071.34	5.03	<0.0072	0.12	0.117	13.19	0.141	2.08
231_131	28.44	113.61	521.96	0.0084	172.07	151056.5	1.701	<0.0038	<0.021	0.0128	3.5	0.0254	0.418
231_15_1	55.36	186.72	878.63	0.038	355.67	255337.86	3.78	<0.0071	0.108	0.0209	10.97	0.095	1.56
231_16_1	<20.84	73.54	343.96	0.0136	164.32	103282.39	1.629	<0.0029	<0.0124	0.0107	3.04	0.0386	0.603
231_17_1	<5.63	18.48	88.69	0.0045	22.96	26774.58	0.482	0.00062	0.0157	0.0178	0.297	0.01142	0.073
231_18_1	<65.07	231.12	1090.86	0.114	417.74	322185.22	6.28	<0.0074	0.304	0.0461	15.94	0.133	2.01
231_19_1	<10.98	41.55	195.35	0.0147	72.96	60823.88	3.82	<0.00140	0.0273	0.025	1.754	0.0445	0.579
231_20_1	<66.01	216.84	1009.86	0.024	932.74	384316.56	2.22	<0.0082	<0.049	0.031	7.62	0.289	4.91
231_21_1	<31.09	116.27	551.54	0.0211	237.09	206909.28	3.56	<0.0037	0.201	0.0295	7.54	0.0735	1.185
231_22_1	<14.69	57.22	265.65	<0.0042	191.02	100753.38	0.857	<0.0020	<0.0094	0.0109	2.18	0.0567	0.881
231_23_1	<82.97	298.36	1356.96	0.056	563.06	515234.09	5.66	<0.0105	0.532	0.0416	16.41	0.112	1.94
231_24_1	<51.01	213.74	979.56	0.068	400.08	341286.75	2.48	<0.0066	0.543	0.18	11.53	0.094	1.15
231_25_1	<78.63	268.2	1227.82	0.036	450.88	431519.19	2.44	<0.0135	<0.060	<0.0082	13.5	0.0406	0.807
231_27_1	<27.69	84.35	392.92	0.0108	158.32	134830.23	2.17	<0.0042	<0.025	0.0037	4.03	0.055	0.589
231_28_1	<60.55	177.98	801.51	0.035	425.21	267769.44	4.73	<0.0079	0.053	0.0146	12.48	0.114	1.77
231_29_1	<39.19	176.18	824.24	0.0155	313.51	296880.81	2.404	<0.0059	0.033	0.038	8.35	0.0651	1.201
231_30_1	<22.46	77.62	360.85	0.0197	206.1	135020.23	1.1	<0.0028	0.116	0.0564	3.04	0.0762	0.96
231_35_1	<8.59	32.31	154.95	0.0303	117.86	52217.44	0.822	<0.00106	0.08	0.0494	1.742	0.0359	0.443
231_36_1	<62.56	250.95	1177.63	0.041	515.87	397360.94	7.02	<0.0085	0.048	0.075	14.99	0.137	2.32
231_37_1	<13.05	46.34	211.54	0.0099	87.71	76898.56	5.34	<0.0018	0.0147	0.0082	1.693	0.0194	0.242
231_38_1	<62.73	228.23	1047.4	0.043	441.22	376435.09	6.11	<0.0089	0.069	0.0202	15.74	0.142	2.15
231_39_1	<26.59	92.13	426.33	0.062	166.27	148922.45	1.04	<0.0042	0.753	0.11	3.51	0.0665	0.982
231_40_1	<112.16	342.85	1571.39	0.039	645.8	584818.5	4.37	<0.0137	<0.085	0.028	15.32	0.169	3.1
231_41_1	<52.67	159.92	738.01	0.0184	432.71	246859.38	3.53	<0.0071	<0.046	0.0085	9.6	0.114	1.82
231_42_1	<823.44	2572.18	11709.05	0.92	8834.99	3921573.5	46.68	<0.110	1.21	2.29	178.34	2.98	45.58
231_43_1	<286.33	1172.13	5204.09	0.23	3347.09	1773769.88	15.19	<0.040	<0.16	0.111	63.34	1.05	18.84
231_44_1	361.99	102.49	479.59	0.156	263.49	144417.41	1.459	<0.0041	0.0224	14.3	32.9	4.15	20.09
231_45_1	<59.59	233.56	1064.95	0.028	452.65	364260.19	2.392	<0.0075	<0.038	0.0128	7.27	0.0874	1.79
Zircon cores													
231_29_2	<87.34	298.57	1365.53	0.034	843.42	505278.53	8.5	<0.0099	<0.060	<0.025	15.34	0.06	1.28
231_47_1	17685.63	437.11	2098.46	5.87	2252.01	739165.75	5.71	0.027	4.59	420.73	1210.92	163.43	803.5
231_48_1	<112.03	310.72	1448.66	<0.037	1116.64	522282.09	19.22	<0.0155	<0.076	0.0267	36.1	0.322	5.64
231_49_1	<102.87	368.94	1754.63	0.047	2427.22	624126.69	4.5	<0.0119	0.198	0.682	14.07	0.851	11.78
231_50_1	<67.61	253.3	1185.84	0.042	1346.24	416538.09	1.51	<0.0093	<0.044	0.418	6.5	0.845	10.8

	Element													
	Sm	Eu	Gd	Tb	Dy	Ho	Er	Tm	Yb	Lu	Hf	Ta	Th	U
Zircon rims														
231_1_1	4.84	0.249	21.58	7.01	77.28	25.95	104.76	22.3	219.74	34.73	8129.2	3.19	63.54	25.03
231_2_1	4.47	0.199	18.8	6.08	67.14	22.58	89.55	18.92	180.62	29.84	6684.4	1.546	61.67	20.84
231_3_1	1.94	0.086	9.01	3.02	35.28	12.58	52.53	11.72	117.28	17.88	4234.64	1.7	64.53	42.75
231_4_1	9.92	0.383	41.82	13.14	142.04	48.12	183.68	38.69	373.95	56.24	12837.27	5.34	411.07	83.03
231_5_1	3	0.174	11.96	3.94	42.94	14.8	59.36	12.97	129.39	20.28	5739.73	2.02	66.75	30.24
231_6_1	1.464	0.115	5.39	1.73	19.62	6.74	28.45	5.81	55.99	10.85	3121.18	0.301	15.26	10.79
231_7_1	16.43	0.484	19.22	4.32	42.58	13.78	55.65	11.84	115.48	17.48	3690	1.041	45.57	46.27
231_8_1	2.87	0.147	12.9	4.64	53.29	19.02	79.3	17.68	180.68	28.48	7485.8	1.796	58.38	66.1
231_9_1	2.46	0.592	8.8	2.61	26	8.15	30.22	5.93	55.3	8.87	2519.17	1.115	29.31	50.99
231_11_1	0.555	0.0396	2.78	1.019	12.65	4.71	21.12	4.76	49.62	7.96	1802.89	0.495	17.34	33.21
231_12_1	3.2	0.181	13.05	3.94	45.3	14.9	61.61	13.19	130.31	19.96	5037.14	1.95	67.82	27.67
231_131	0.822	0.0525	4.19	1.514	17.94	6.35	26.33	5.73	56.89	9.02	3042.35	0.707	17.69	40.65
231_15_1	2.6	0.136	10.62	3.39	36.85	13.05	53.71	11.3	110.54	18.75	5349.95	1.426	41.21	22.63
231_16_1	1.054	0.0833	4.88	1.598	17.55	6.21	25.63	5.41	53.11	8.43	2102.11	0.628	18.14	26.27
231_17_1	0.0983	0.0184	0.504	0.198	2.36	0.822	3.34	0.712	7.16	1.153	604.85	0.318	2.171	33.06
231_18_1	2.94	0.164	12.3	3.97	45.97	15.49	62.14	13.55	133.57	21.7	6494.5	2.78	75	27.47
231_19_1	0.813	0.0964	2.198	0.68	7.52	2.63	10.87	2.39	24	3.96	1219.98	0.326	8.92	38.14
231_20_1	7.95	0.575	32.93	10.16	110.1	37.11	143.32	30.21	280.65	43.64	6154.58	0.891	61.15	52.12
231_21_1	1.83	0.107	6.87	2.17	25.05	8.85	36.26	7.98	79.08	12.7	3592.31	1.49	36.15	23.72
231_22_1	1.41	0.128	6.13	1.95	21.21	7.34	29.86	6.36	60.26	9.25	1614.92	0.285	15.93	9.11
231_23_1	3.79	0.193	16.12	5.34	61.01	20.91	86.13	18.74	188.15	29.47	9218.09	2.32	92.6	52.43
231_24_1	2.41	0.222	9.75	3.57	40.83	15	64.5	14.68	147.86	24.45	6934.13	1.214	35.25	52.43
231_25_1	1.99	0.165	9.93	3.7	44.77	17.21	75.7	17.55	188.41	33.15	9211.6	1.237	32.77	62.74
231_27_1	1.11	0.0518	4.4	1.475	17.02	5.96	24.81	5.54	53.39	8.82	2746.64	0.869	25.2	23.83
231_28_1	2.9	0.138	11.82	3.8	42.07	14.24	57.99	12.3	119.12	19.44	5419.82	1.91	66.32	20.59
231_29_1	2.04	0.11	8.31	2.94	33.95	11.94	49.02	10.74	108.38	17.97	5571.7	1.175	46.06	61.43
231_30_1	1.35	0.1327	6.03	1.97	22.12	7.59	31.13	6.58	64.16	10.11	2275.93	0.41	15.16	20.81
231_35_1	0.674	0.0446	3.23	1.105	12.69	4.62	18.84	3.9	37.35	5.86	1011.91	0.265	14.65	12.61
231_36_1	3.63	0.163	15.75	5.08	56.43	19.56	79.81	16.83	157.11	27.85	7708.11	2.8	84.75	36.4
231_37_1	0.354	0.0302	2.054	0.726	8.66	3.18	13.7	3.09	30.92	4.84	1421.42	0.465	13.71	32.31
231_38_1	3.45	0.174	13.81	4.51	48.99	16.8	67.55	14.73	143.78	23	6718.94	2.36	69.08	26.21
231_39_1	1.31	0.14	5.22	1.61	17.65	6.06	23.44	5.1	50.96	7.99	2918.84	0.441	15.95	8.08
231_40_1	4.6	0.184	20.18	6.44	72.42	24.17	95.63	20.21	197.34	32.08	10188.02	1.8	83.44	22
231_41_1	2.86	0.104	12.65	4.27	45.73	15.89	64.39	13.29	126.99	20.98	5027.43	1.487	62.13	21.95
231_42_1	73.1	3.47	306.18	92.82	980.08	333.42	1313.53	270.95	2584.39	408.73	83158.48	16.79	1556.42	457.1
231_43_1	27.7	2.2	115.8	36.46	386.57	133.19	509.24	107.57	1035.54	171.92	34996.16	5.85	82.1	30.97
231_44_1	5.56	0.337	11.05	2.98	30.73	10.29	41.21	8.49	81.58	13.3	2889.16	0.481	24.68	20.9
231_45_1	3.13	0.177	13.8	4.52	49.18	16.89	68.54	13.79	129.81	25.32	7199.2	0.913	42.97	8.86
Zircon cores														
231_29_2	3.78	0.201	19.57	7.28	87.82	32.65	135.55	30.03	294.2	44.58	8800.61	2.48	106.84	111.05
231_47_1	188.8	7.61	225.69	39.01	314.77	90.26	326.6	62.24	565.7	90.89	12113.3	2.17	118.75	100.09
231_48_1	8.76	0.291	37.22	11.35	123.17	41.38	161.1	32.87	308.3	48.12	9026.2	6.54	394.33	116.56
231_49_1	18.68	1.186	75.9	25.01	275.31	93.84	375.34	78.12	728.3	105.67	10427.09	1.72	177.33	179.37
231_50_1	13.94	1.486	53.78	15.7	167	54.31	208.82	42.04	392.44	59.83	6347.39	0.575	57.99	45.99

Table 9

	Element															
Sample ID	**La**	**Ce**	**Pr**	**Nd**	**Sm**	**Eu**	**Gd**	**Tb**	**Dy**	**Ho**	**Er**	**Tm**	**Yb**	**Lu**	**Ce/Ce***	**Eu/Eu***
Zircon rims																
231_1_1	-	22.49	1.27	3.79	20.95	2.86	70.52	120.93	202.83	304.94	420.72	626.45	886.03	911.62	-	0.23
231_2_1	0.228	11.41	1.391	4.02	19.33	2.29	61.43	104.8	176.22	265.29	359.62	531.37	728.3	783.16	4.88	0.20
231_3_1	0.078	10.01	0.527	1.58	8.41	0.99	29.46	52.04	92.61	147.8	210.98	329.11	472.89	469.42	11.88	0.19
231_4_1	-	44.62	2.72	8.92	42.96	4.4	136.67	226.57	372.82	565.51	737.66	1086.81	1507.86	1476.01	-	0.18
231_5_1	0.6	11.74	1.173	3.02	12.97	2	39.08	67.88	112.7	173.86	238.37	364.36	521.73	532.41	3.37	0.27
231_6_1	0.08	3.46	0.48	1.242	6.34	1.32	17.61	29.82	51.51	79.18	114.26	163.07	225.77	284.68	4.25	0.38
231_7_1	122.59	123.17	112.88	109.49	71.11	5.57	62.81	74.52	111.77	161.95	223.49	332.66	465.64	458.69	-	0.25
231_8_1	0.115	12.63	0.611	2.28	12.4	1.69	42.15	80.05	139.88	223.52	318.49	496.55	728.55	747.42	11.47	0.23
231_9_1	2.46	6.43	1.927	3.3	10.67	6.8	28.76	45.03	68.23	95.75	121.35	166.58	223	232.85	-	1.19
231_11_1	0.039	2.294	0.152	0.478	2.4	0.455	9.09	17.56	33.19	55.4	84.83	133.61	200.1	208.82	7.17	0.30
231_12_1	0.319	13.78	1.03	2.93	13.84	2.08	42.65	67.91	118.91	175.13	247.42	370.56	525.45	523.96	5.79	0.26
231_131	0.0348	3.65	0.186	0.588	3.56	0.603	13.69	26.11	47.08	74.66	105.76	160.98	229.38	236.83	10.92	0.26
231_15_1	0.057	11.46	0.694	2.19	11.25	1.57	34.69	58.53	96.71	153.31	215.7	317.5	445.72	492.17	13.87	0.24
231_16_1	0.0292	3.17	0.282	0.848	4.56	0.957	15.94	27.56	46.06	72.97	102.95	151.83	214.16	221.22	8.41	0.34
231_17_1	0.0486	0.31	0.0834	0.1026	0.426	0.212	1.647	3.41	6.19	9.65	13.42	20	28.88	30.27	1.17	0.77
231_18_1	0.126	16.66	0.97	2.83	12.72	1.89	40.19	68.51	120.67	182.07	249.55	380.6	538.6	569.61	11.47	0.26
231_19_1	0.068	1.832	0.325	0.814	3.52	1.108	7.18	11.72	19.73	30.86	43.67	67.25	96.78	104	2.97	0.67
231_20_1	0.085	7.96	2.11	6.9	34.43	6.61	107.6	175.24	288.98	436.13	575.58	848.53	1131.67	1145.29	4.52	0.33
231_21_1	0.08	7.88	0.537	1.67	7.92	1.23	22.46	37.47	65.74	103.95	145.62	224.29	318.89	333.27	9.15	0.28
231_22_1	0.0298	2.28	0.414	1.239	6.11	1.47	20.04	33.59	55.67	86.25	119.91	178.57	242.98	242.75	4.94	0.41
231_23_1	0.113	17.14	0.818	2.73	16.39	2.22	52.69	92.14	160.13	245.68	345.92	526.33	758.66	773.61	13.57	0.23
231_24_1	0.491	12.05	0.689	1.62	10.44	2.56	31.87	61.57	107.16	176.27	259.05	412.26	596.2	641.64	4.99	0.43
231_25_1	-	14.11	0.296	1.135	8.61	1.9	32.46	63.72	117.5	202.21	304.03	492.96	759.71	870.08	-	0.35
231_27_1	0.01	4.21	0.402	0.828	4.83	0.595	14.38	25.43	44.66	70.01	99.63	155.68	215.3	231.38	15.98	0.22
231_28_1	0.04	13.04	0.83	2.49	12.57	1.58	38.61	65.46	110.41	167.28	232.9	345.44	480.32	510.23	17.22	0.22
231_29_1	0.103	8.72	0.475	1.69	8.84	1.26	27.15	50.63	89.1	140.3	196.88	301.61	437.03	471.74	9.49	0.25
231_30_1	0.154	3.18	0.556	1.35	5.85	1.526	19.69	34.05	58.07	89.23	125	184.82	258.7	265.39	2.62	0.43
231_35_1	0.135	1.821	0.262	0.623	2.92	0.513	10.56	19.04	33.3	54.29	75.68	109.5	150.62	153.86	2.33	0.28
231_36_1	0.205	15.66	1	3.26	15.72	1.87	51.46	87.51	148.12	229.9	320.53	472.72	633.51	730.84	8.32	0.20
231_37_1	0.0223	1.769	0.141	0.34	1.53	0.347	6.71	12.51	22.74	37.35	55.02	86.66	124.66	126.93	7.59	0.33
231_38_1	0.055	16.45	1.04	3.03	14.92	2	45.12	77.7	128.57	197.44	271.28	413.64	579.78	603.63	16.55	0.24
231_39_1	0.299	3.67	0.485	1.38	5.66	1.61	17.05	27.76	46.33	71.25	94.12	143.35	205.48	209.69	2.32	0.50
231_40_1	0.077	16.01	1.23	4.36	19.91	2.11	65.94	111.01	190.08	284.06	384.07	567.64	795.74	842	12.52	0.18
231_41_1	0.023	10.03	0.829	2.57	12.37	1.19	41.35	73.61	120.03	186.66	258.59	373.23	512.07	550.74	17.48	0.16
231_42_1	6.25	186.35	21.76	64.1	316.45	39.94	1000.6	1600.32	2572.39	3918	5275.21	7610.83	10420.93	10727.83	3.85	0.22
231_43_1	0.301	66.18	7.66	26.5	119.93	25.25	378.44	628.69	1014.63	1565.09	2045.14	3021.53	4175.58	4512.41	10.49	0.36
231_44_1	38.98	34.38	30.32	28.26	24.06	3.88	36.1	51.3	80.66	120.9	165.52	238.54	328.94	348.98	-	0.40
231_45_1	0.035	7.6	0.638	2.51	13.54	2.04	45.09	78.01	129.09	198.48	275.26	387.23	523.42	664.46	12.24	0.25
Zircon cores																
231_29_2	-	16.03	0.438	1.8	16.36	2.31	63.96	125.51	230.51	383.69	544.36	843.42	1186.3	1169.95	-	0.22
231_47_1	1146.39	1265.33	1192.9	1130.1	817.34	87.43	737.54	672.62	826.16	1060.66	1311.66	1748.42	2281.04	2385.53	0.26	0.34
231_48_1	0.073	37.72	2.35	7.93	37.93	3.35	121.65	195.61	323.27	486.27	646.97	923.4	1243.15	1262.87	21.92	0.15
231_49_1	1.86	14.71	6.21	16.57	80.88	13.63	248.04	431.24	722.59	1102.67	1507.39	2194.35	2936.71	2773.36	1.04	0.29
231_50_1	1.138	6.79	6.17	15.19	60.36	17.08	175.74	270.7	438.32	638.18	838.64	1181.02	1582.44	1570.3	0.62	0.51

Table 10

Sample	Age (Ma)	error (1σ)	Ti (ppm)	±Ti	Temperature (°C)	±
Zircon rims						
231-1.1	1170.0	19.4	1227.82	107	1466.21	36
231-2.1	1128.4	20.5	395.01	20	1215.26	28
231-3.1	1158.8	20.6	551.54	46	1281.27	30
231-4.1	1226.6	11.5	479.59	25	1252.92	29
231-5.1	1136.2	17.3	878.63	41	1383.78	33
231-6.1	1206.1	55.6	1047.4	87	1426.06	34
231-7.1	1184.3	21.0	824.24	31	1368.92	32
231-8.1	1202.3	16.2	1177.63	44	1455.48	35
231-9.1	1146.7	14.0	1090.86	48	1436.15	35
231-11.1	1221.2	19.1	5204.09	475	1941.81	53
231-12.1	1191.9	19.0	154.95	6	1056.91	23
231-13.1	1220.8	20.6	738.01	68	1343.84	32
231-15.1	1101.1	20.4	477.46	18	1252.04	29
231-16.1	1164.2	20.0	265.65	22	1143.74	25
231-17.1	1301.6	18.2	1365.53	51	1494.14	37
231-18.1	1083.6	16.4	651.7	50	1316.51	31
231-19.1	1059.5	14.8	1417.94	61	1504.25	37
231-20.1	1165.5	24.6	1356.96	109	1492.46	37
231-21.1	1144.7	19.4	343.96	16	1189.51	27
231-22.1	1133.8	31.5	792.33	65	1359.87	32
231-23.1	1154.3	19.7	1009.86	82	1417.10	34
231-24.1	1129.4	12.7	261.2	12	1140.85	25
231-25.1	1082.3	12.2	1089.4	52	1435.82	35
231-27.1	1249.9	23.0	1064.95	41	1430.17	34
231-28.1	1119.1	22.5	657.62	23	1318.47	31
231-29.1	1094.1	11.9	897.27	76	1388.72	33
231-30.1	1147.9	21.5	195.35	7	1092.89	24
231-35.1	1170.3	26.9	392.92	35	1214.25	28
231-36.1	1124.9	25.0	1174.2	42	1454.74	35
231-37.1	1187.8	17.1	360.85	31	1198.32	27
231-38.1	1146.5	20.2	88.69	4	977.58	21
231-39.1	1172.7	35.8	801.51	73	1362.50	32
231-40.1	1167.6	28.2	979.56	86	1409.69	34
231-41.1	1205.5	22.0	211.54	17	1105.71	24
231-42.1	1086.6	11.5	1962.29	154	1596.55	40
231-43.1	1218.9	17.3	1571.39	125	1532.44	38
231-44.1	1217.2	25.5	426.33	37	1229.85	28
231-45.1	1135.4	31.4	521.96	22	1269.96	29
Zircon cores						
231-29.2	1352.3	11.6	1754.63	148	1563.71	39
231-47.1	1319.9	11.0	1448.66	118	1510.06	37
231-48.1	1220.8	9.7	11709.05	1086	2343.56	70
231-49.1	1264.9	7.8	2098.46	78	1616.81	41
231-50.1	1370.3	16.4	1185.84	101	1457.26	35

Appendix 1

Geological Map of the Latitude Hills

Appendix 2

Photomicrographs and Element Maps for MHLH-7

Photomicrograph under transmitted, plane-light and X-ray element of Silicon for sample MHLH-7.

2000 µm

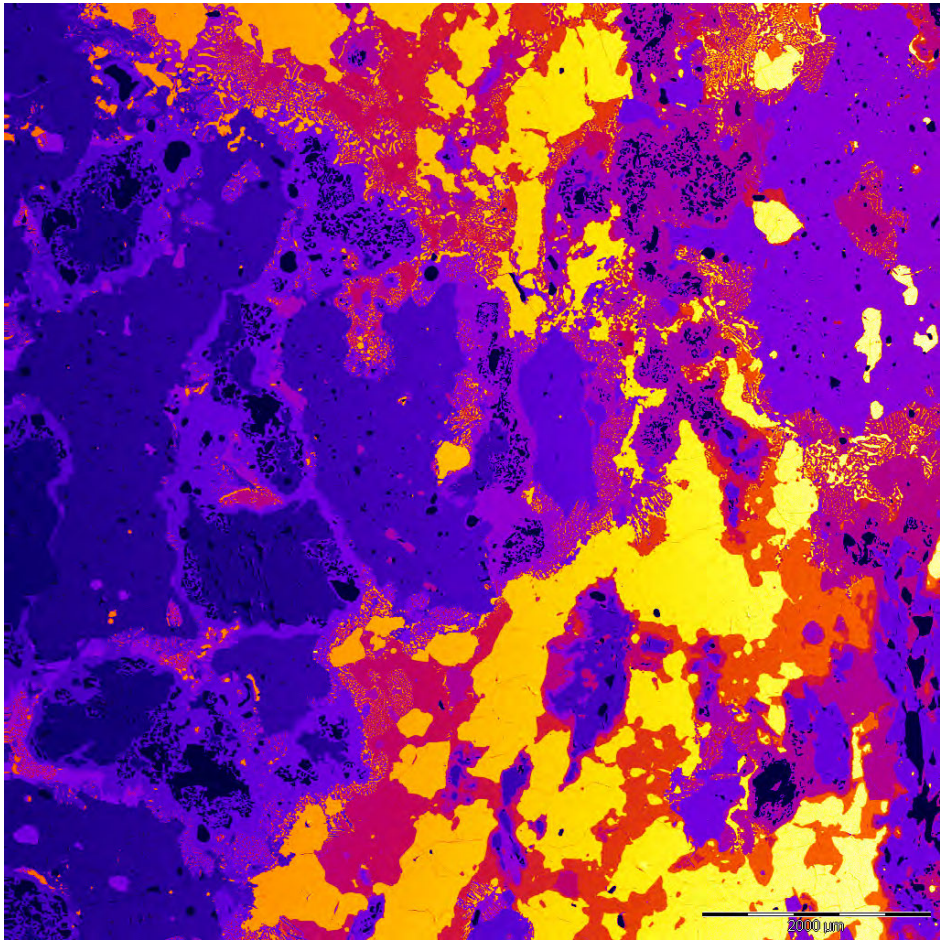

2000 µm

Left: Photomicrograph of MHLH-7, viewed through plane, transmitted light.
Right: X-ray element map of Silicon from MHLH-7, produced on the Cameca SX51 electron microprobe, Adelaide Microscopy.

Photomicrograph under transmitted plane-light and X-ray element of Magnesium for sample MHLH-7.

2000 µm

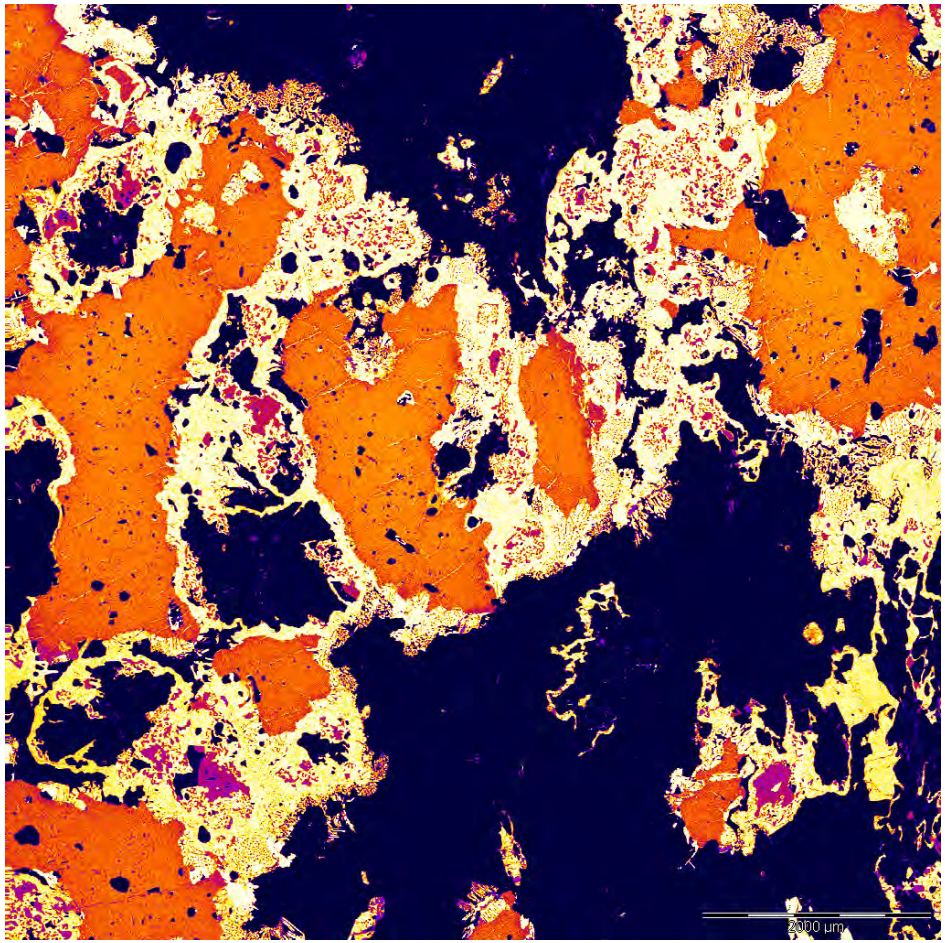

2000 µm

Left: Photomicrograph of MHLH-7, viewed through plane, transmitted light.
Right: X-ray element map of Magnesium from MHLH-7, produced on the Cameca SX51 electron microprobe, Adelaide Microscopy.

Photomicrograph under plane-light transmitted light and X-ray element of Calcium for sample MHLH-7.

2000 µm

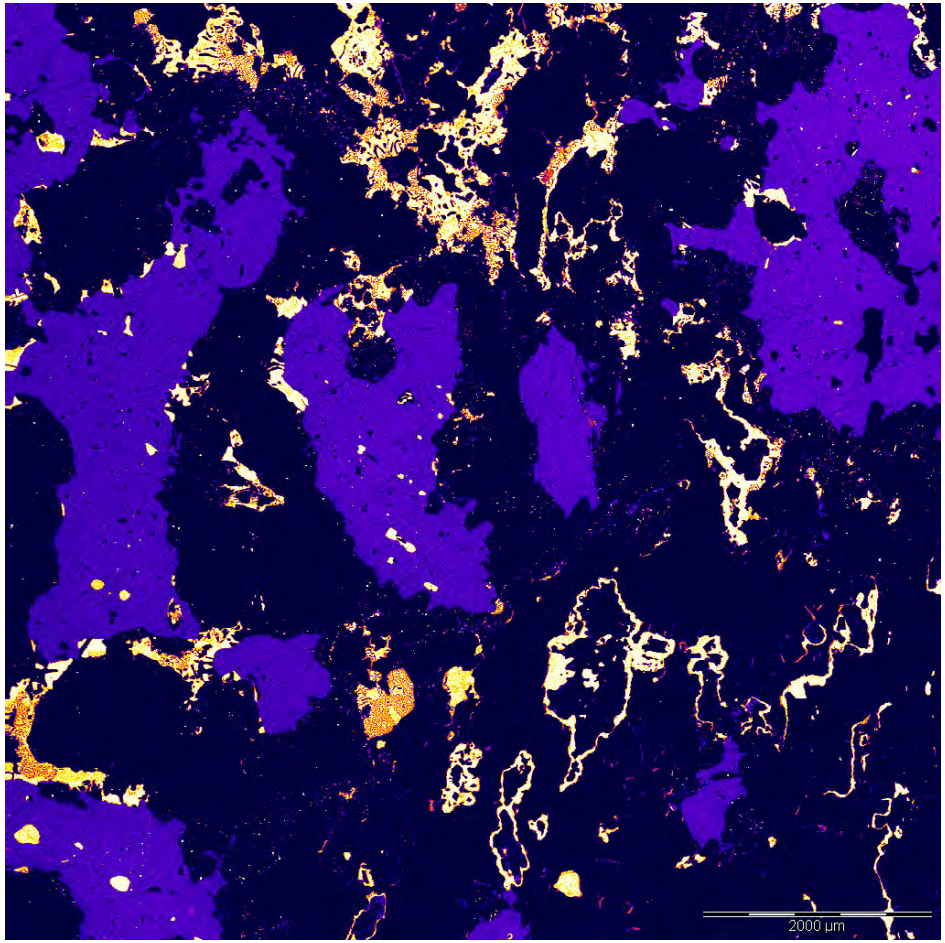

2000 µm

Left: Photomicrograph of MHLH-7, viewed through plane, transmitted light.
Right: X-ray element map of Clacium from MHLH-7, produced on the Cameca SX51 electron microprobe, Adelaide Microscopy.

Photomicrograph under transmitted plane-light and X-ray element of Sodium for sample MHLH-7.

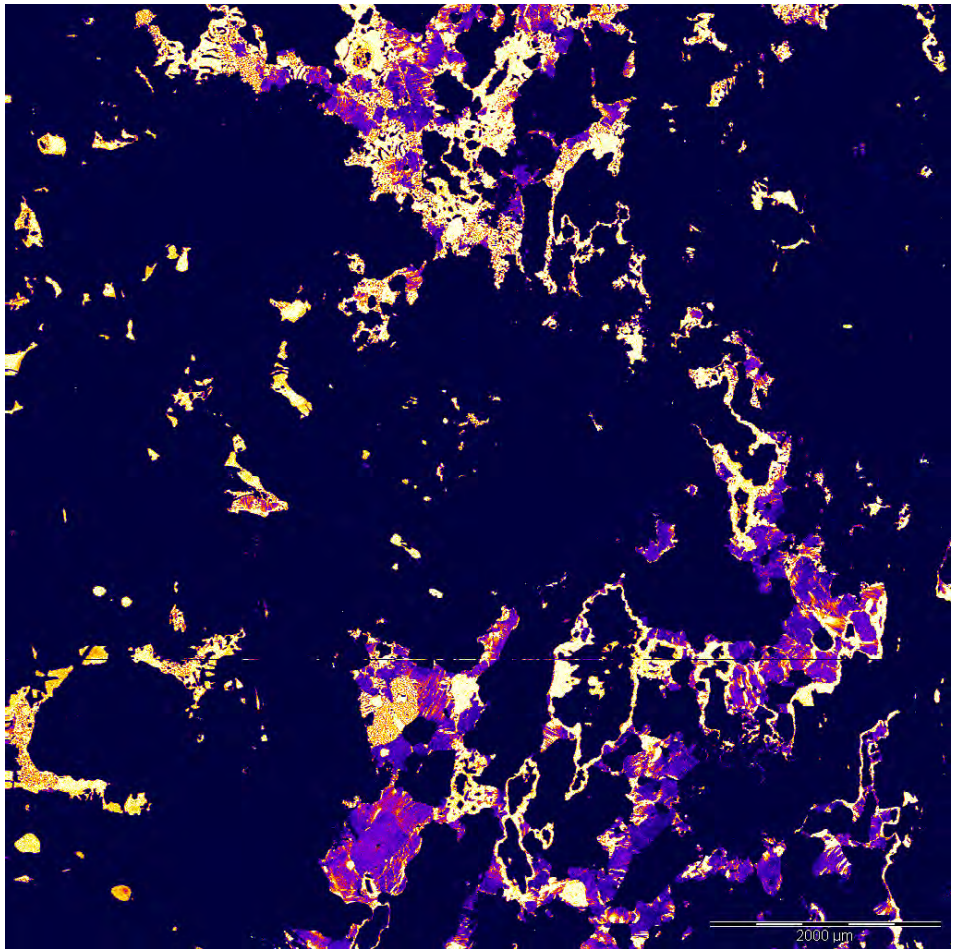

Na

2000 µm

Left: Photomicrograph of MHLH-7, viewed through plane, transmitted light.
Right: X-ray element map of Sodium from MHLH-7, produced on the Cameca SX51 electron microprobe, Adelaide Microscopy.

Photomicrograph under transmitted plane-light and X-ray element of Potassium for sample MHLH-7.

2000 µm

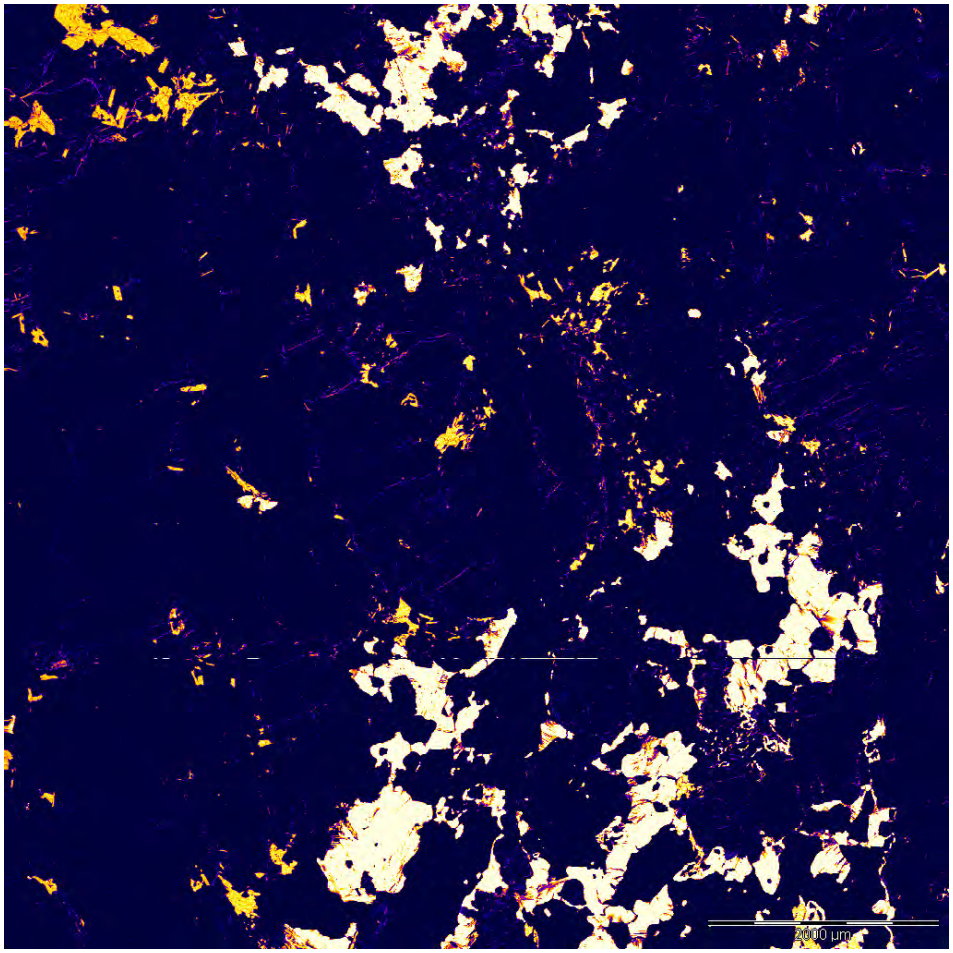

2000 µm

Left: Photomicrograph of MHLH-7, viewed through plane, transmitted light.
Right: X-ray element map of Potassium from MHLH-7, produced on the Cameca SX51 electron microprobe, Adelaide Microscopy.

Photomicrograph under transmitted plane-light and X-ray element of Iron for sample MHLH-7.

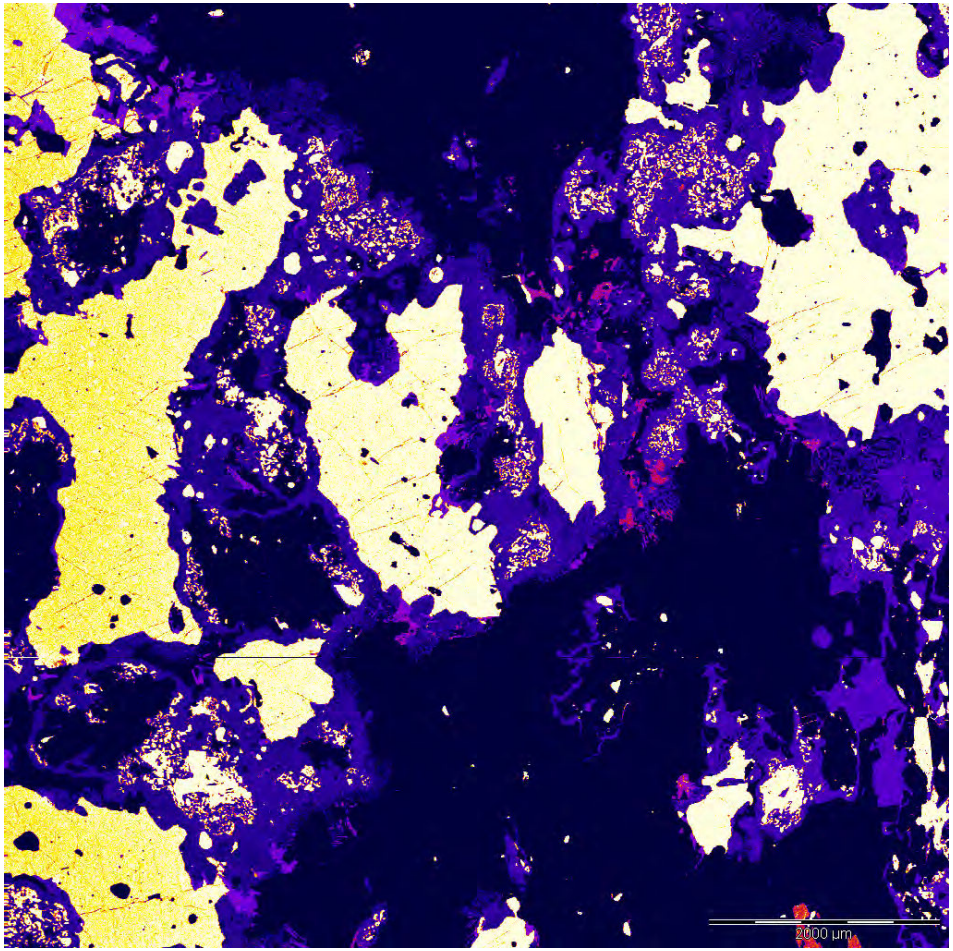

Left: Photomicrograph of MHLH-7, viewed through plane, transmitted light.
Right: X-ray element map of Iron from MHLH-7, produced on the Cameca SX51 electron microprobe, Adelaide Microscopy.

Photomicrograph under transmitted plane-light and X-ray element of Aluminium for sample MHLH-7.

2000 µm

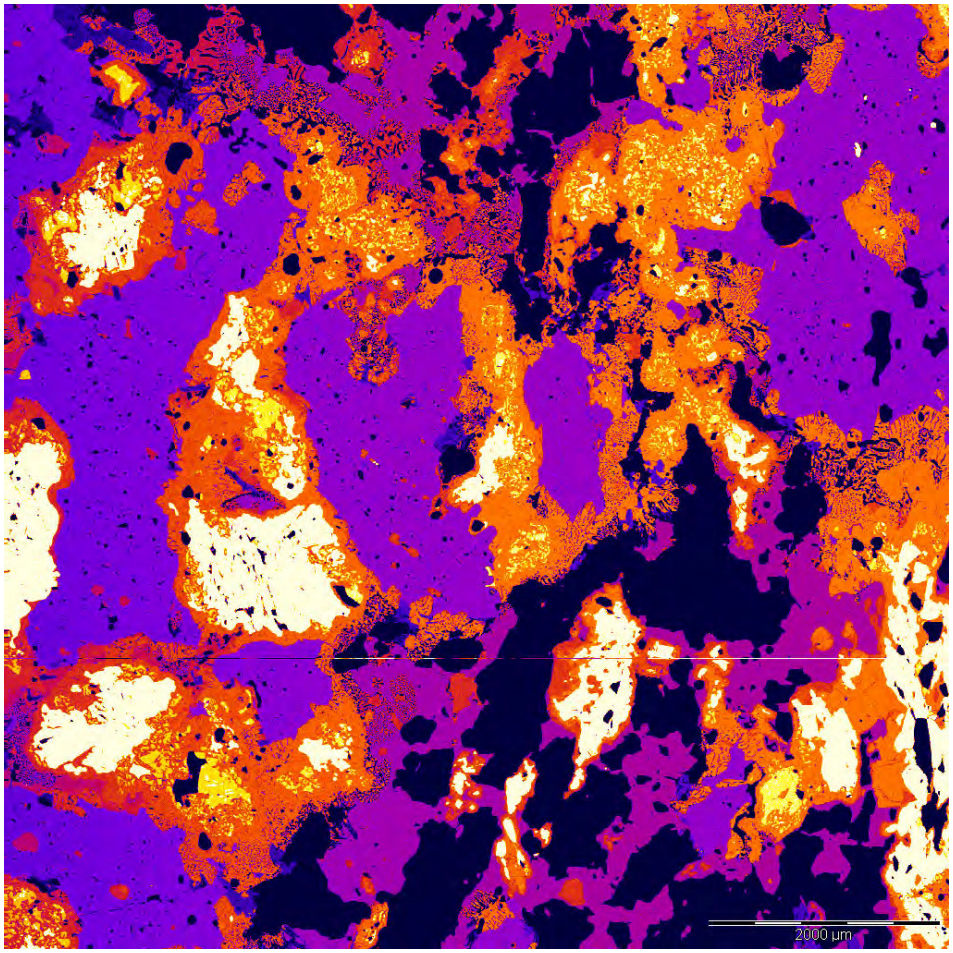

2000 µm

Left: Photomicrograph of MHLH-7, viewed through plane, transmitted light.
Right: X-ray element map of Aluminium from MHLH-7, produced on the Cameca SX51 electron microprobe, Adelaide Microscopy.

Photomicrograph under transmitted, plane-light and X-ray element of Titanium for sample MHLH-7.

2000 µm

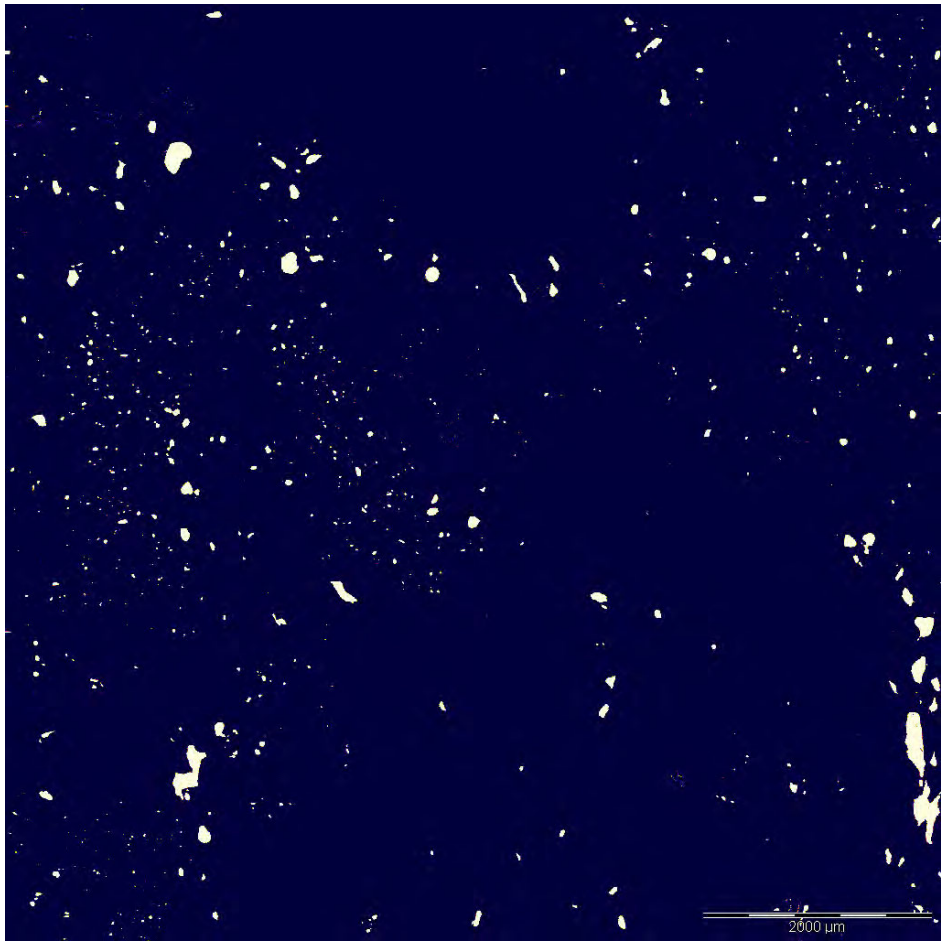

2000 µm

Left: Photomicrograph of MHLH-7, viewed through plane, transmitted light.
Right: X-ray element map of Titanium from MHLH-7, produced on the Cameca SX51 electron microprobe, Adelaide Microscopy.

RECORD 2009/15

USING CALCULATED PSEUDOSECTIONS IN THE SYSTEM NCKFMASHTO AND SHRIMP U-PB ZIRCON DATING TO CONSTRAIN THE METAMORPHIC EVOLUTION OF PARAGNEISSES IN THE LATITUDE HILLS WEST MUSGRAVE PROVINCE, WESTERN AUSTRALIA

KING

This Record is published in digital format (PDF) and is available online at: www.dmp.wa.gov.au/GSWApublications.
Laser-printed copies can be ordered from the Information Centre for the cost of printing and binding.

Further details of geological publications and maps produced by the Geological Survey of Western Australia can be obtained by contacting:

Information Centre
Department of Mines and Petroleum
100 Plain Street
EAST PERTH, WESTERN AUSTRALIA 6004
Phone: (08) 9222 3459 Fax: (08) 9222 3444
www.dmp.wa.gov.au/GSWApublications